Titre: Title:	Cu on Co Improves C5+ Selectivity in the Fischer-Tropsch Synthesis
Auteur: Author:	Charles-David Guérette
Date:	2023
Type:	Mémoire ou thèse / Dissertation or Thesis
Référence: Citation:	Guérette, C.-D. (2023). Cu on Co Improves C5+ Selectivity in the Fischer-Tropsch Synthesis [Mémoire de maîtrise, Polytechnique Montréal]. PolyPublie. https://publications.polymtl.ca/53462/

POLYTECHNIQUE MONTRÉAL
affiliée à l'Université de Montréal

Cu on Co improves C_{5+} selectivity in the Fischer-Tropsch synthesis

CHARLES-DAVID GUÉRETTE
Département de génie chimique

Mémoire présenté en vue de l'obtention du diplôme de *Maîtrise ès sciences appliquées*
Génie chimique

Mai 2023

POLYTECHNIQUE MONTRÉAL
affiliée à l'Université de Montréal

Ce mémoire intitulé :

Cu on Co improves C_{5+} selectivity in the Fischer-Tropsch synthesis

présenté par **Charles-David GUÉRETTE**
en vue de l'obtention du diplôme de *Maîtrise ès sciences appliquées*
a été dûment accepté par le jury d'examen constitué de :

Olivier HENRY, président
Daria Camilla BOFFITO, membre et directrice de recherche
Gregory PATIENCE, membre et codirecteur de recherche
Jan KOPYSCINSKI, membre externe

DEDICATION

To my spouse, my parents and my loved ones
who have supported and encouraged me
throughout my journey

ACKNOWLEDGEMENTS

First, I would like to thank my supervisor, Prof. Daria Camilla Boffito. Thank you for your support and wise advice throughout this journey. Your feedback and critical thinking helped me to excel in scientific research and as a person. You have encouraged me to discover a new area of engineering that had never crossed my mind and made me want to learn more about how it works and its applications. Thank you for opportunities such as AQPER and CCEC that allowed me to show the world how far my team and I have come over the past two years and for your trust in me throughout the master's program. I leave the university with the knowledge that I look forward to sharing.

Thank you to my co-supervisor, Prof. Gregory S. Patience, for his feedback and support throughout the writing of my paper and thesis. Writing a scientific text seemed complex and challenging initially, but your excellent guidance and experience showed me that writing is enjoyable and rewarding.

I want to thank my colleague Dr. Christopher Panaritis. When I started my master's degree, I was a little confused by all the novelty, and he took his time to introduce me to the team and explain the project in detail. From the beginning, he trusted me and encouraged me to share my opinion and ideas, making me feel I was essential to the development of this research project. Thank you for accompanying me in writing and editing the article and this thesis. Scientific writing was not something I was exceptionally comfortable with. Still, he showed me that it was not complicated by helping me with the writing and editing by giving me constructive criticism and sound advice. I will remember our long coffee breaks where we discussed ambitious ideas and future plans. I end this stage of my life hoping we will stay in touch and our paths will cross again.

I want to thank my colleague Prof. Ergys Pahija. At the beginning of my master's degree, when the Fischer-Tropsch reactor was not operational, he gave me some coding tasks that quickly turned into a project. He helped me get back into coding and introduced me to modelling complex systems. Thanks to him, I enjoyed writing Python code, which no one else had done during my undergraduate studies. When I had questions, he was always available and answered them with exceptional pedagogy. He gave me confidence when I felt like I had too much on my hands by giving me excellent advice and a huge helping hand. I remember our early morning lunches in the cafeteria, where we discussed innovative and challenging topics. I hope we will stay in touch and cross paths again.

Thank you to my colleague Brian Rutheford who helped me by explaining how the GC works and being my eyes when there was a problem with the reactor and I couldn't make it to the lab. Your advice helped me in completing my master's degree, especially from someone who has met the same path. I will remember the AQPER and CCEC conferences we did together and our outings. I wish you much success in your future projects and hope to see you soon.

RÉSUMÉ

La croissance de la population mondiale et des activités humaines contribue à l'augmentation globale de la consommation d'énergie telle que les combustibles fossiles, ce qui libère davantage de CO_2 dans l'atmosphère. Ce défi pousse la communauté scientifique à développer des technologies et des méthodes pour convertir et stocker le CO_2. La conversion du CO_2 en hydrocarbures est une méthode qui permettrait de produire des carburants à faible empreinte carbone. La synthèse de carburant d'avion permettrait à elle seule de réduire de 2% les émissions mondiales de CO_2. Le processus consiste à convertir le CO_2 atmosphérique en CO par la Réaction du Gaz à l'Eau Inverse, puis à convertir le CO en carburant d'avion via la Synthèse Fischer-Tropsch, le tout en étant alimenté par l'électricité renouvelable du Québec.

Les 4 objectifs du projet permettent de démontrer que le Cu peut remplacer les métaux nobles comme promoteurs pour augmenter la performance du catalyseur. Le **premier objectif** était de synthétiser des catalyseurs avec des Nanoparticules (NPs) de Co dopées de NPs de Cu afin d'évaluer l'effet du Cu sur la conversion du gaz de synthèse (H_2 et CO) en carburant d'avion. Le **deuxième objectif** était d'identifier le % massique optimal de Cu dopé sur le catalyseur pour maximiser la conversion du CO et la production de paraffine C_{5+} tout en minimisant la formation de CH_4. Le **troisième objectif** était d'établir une relation entre les propriétés physicochimiques des catalyseurs et leur conversion. Le **quatrième objectif** était de concevoir, à partir des résultats obtenus, un modèle informatique permettant d'identifier le % massique optimal de Cu à imprégner afin de maximiser la production de paraffine C_{5+}.

Sept catalyseurs, dont le % massique des NPs de Co et de Cu imprégnés variait entre 0 et 0,15 g g^{-1}, ont été synthétisés en utilisant la méthode d'imprégnation par ultrasons. La sélectivité de chaque catalyseur à produire des paraffines C_{5+} a été testée dans un réacteur Fischer-Tropsch à une température de 230°C et à une pression de 20 bar pendant 90 h. La Microscopie Électronique en Transmission (TEM), la Microscopie Électronique en Transmission à Balayage (STEM), la Diffractométrie de Rayons X (XRD) et la Réduction en Température Programmée (TPR) ont été utilisées pour caractériser les catalyseurs. Co15-Cu0.15 est le catalyseur le plus performant avec une conversion du CO de 66%, une sélectivité pour la paraffine C_{5+} de 29% et une sélectivité de 16% pour le CH_4. Les images TEM, avant la réaction, montre une dispersion uniforme des NPs de CoCu sur le support Al_2O_3.

ABSTRACT

The increase in global energy consumption, including the burning of fossil fuels, which increases the amount of CO_2 in the atmosphere, results from the development of the world's population and human activity. This challenge drives the scientific community to develop technologies and methods to convert and store CO_2. Converting CO_2 into hydrocarbons is a method that would allow the production of low-carbon footprint fuels. Jet fuel synthesis alone would reduce global CO_2 emissions by 2%. It is a solution that uses renewable electricity generated in Quebec to transform atmospheric CO_2 into CO using the Reverse Water-Gas Shift reaction and then turns the CO into jet fuel via the Fischer-Tropsch Synthesis.

The 4 objectives of the project allow to demonstrate that Cu can replace noble metals as promoters to increase the performance of the catalyst. The **first objective** was to synthesize catalysts with Co Nanoparticles (NPs) doped with Cu NPs to evaluate the effect of Cu on the conversion of syngas (H_2 and CO) into jet fuel. The **second objective** was identifying the optimal wt % of Cu doped on the catalyst to maximize CO conversion and C_{5+} paraffin production while minimizing CH_4 formation. The **third objective** was to establish a relationship between the physicochemical properties of the catalysts and their conversion. The **fourth objective** was to model, using the obtained results, a computer model allowing to identify the optimal wt % of Cu to impregnate to maximize the production of C_{5+} paraffin.

Seven catalysts, whose wt % of Co and Cu NPs impregnated could vary between 0 and 0.15 g g^{-1}, were synthesized using the ultrasonic impregnation method. Co15-Cu0.15 is the best-performing catalyst with a CO conversion of 66% and selectivity for C_{5+} paraffin of 29% while having the lowest selectivity for CH_4 at 16%. Transmission Electron Microscopy (TEM) images showed uniform CoCu NPs dispersion on the Al_2O_3 support before the reaction. Scanning Transmission Electron Microscopy (STEM), X-Ray Diffraction (XRD), and Temperature Programmed Reduction (TPR) were also used to characterize the catalysts. The selectivity of each catalyst to produce C_{5+} hydrocarbons was tested in a Fischer-Tropsch reactor at a temperature of 230°C and a pressure of 20 bar for 90 h.

TABLE OF CONTENTS

LIST OF TABLES

LIST OF FIGURES

LIST OF SYMBOLS AND ACRONYMS

ASF	Anderson-Schulz-Flory
EDX	Energy Dispersive X-ray
EELS	Electron Energy-Loss Spectrometer
FID	Flame Ionization Detector
FT	Fischer-Tropsch
FTS	Fischer-Tropsch Synthesis
GC	Gas Chromatograph
GHG	Greenhouse Gases
HSPE	Hydrogen Spillover Effect
HTFT	High Temperature Fischer-Tropsch
LTFT	Low Temperature Fischer-Tropsch
MFC	Mass Flow Controller
MSI	Metal-Support Interactions
MWD	Molecular Weight Distribution
NP	Nanoparticle
PCM	Particle Migration and Coalescence
RWGS	Reverse Water-Gas Shift
STEM	Scanning Transmission Electron Microscopy
TCD	Thermal Conductivity Detector
TEM	Transmission Electron Microscopy
TOF	Tunrover Frequency
TPR	Temperature Programmed Reduction
VdW	Van der Waals
WGS	Water-Gas Shift
XRD	X-Ray Diffraction

LIST OF APPENDICES

CHAPTER 1 INTRODUCTION

1.1 The Problem

The fight against climate change is one of the most significant challenges of the 21st century. The growth of the world's population and human activities contributes to the overall increase in energy consumption, such as fossil fuels (oil, coal and gas), which account for about 82% of global energy consumption [1]. The methane (CH_4), carbon dioxide (CO_2) and nitrous oxide (NO_x) that they generate during their combustion are pollutants and Greenhouse Gases (GHG) [2]. In 2020, 63% of the energy consumed in Canada came from fossil fuels [1]. Of this energy consumed, 27% (179 MT of CO_2 eq.) was used to fuel the oil and gas sector and 24% (159 MT of CO_2 eq.) was used for transportation [3]. Hydroelectricity, wind and solar power are renewable and sustainable energies. Still, their production is not always stable, as geography and weather limit the production to meet the population's demand, so it is necessary to store energy. One of the alternatives is to store renewable electricity in the form of electrofuel. This method consists of storing renewable electricity in the chemical bonds of liquid or gaseous fuels through the reduction of captured carbon [4]. Electrofuels would allow the storage and production of carbon-neutral fuels, thereby reducing GHG emissions from the oil and gas, and transportation sectors [4].

Since CO_2 is chemically stable due to the covalent double bonds between the carbon and oxygen atoms, it is a high-energy process for the carbon to reach an oxidation state of +2 or lower to form hydrocarbons. Various methods such as electrochemical, metal-based and catalytic CO_2 conversion have been developed to perform this synthesis [5,6]. The challenges surrounding the use of catalysts is to ensure that they can function at the operating conditions of the Fischer-Tropsch (FT) reactor, i.e. at temperatures that can vary from 180 to 350°C and at a pressure that can reach 30 bar without deactivation while having a high selectivity towards C_{5+} paraffin [7]. Furthermore, the price of the raw materials used in synthesizing the catalysts must also be considered, as they will have a significant economic impact when the time comes to scale up the reactor, and the quantity of catalyst inside [7].

The Reverse Water-Gas Shift (RWGS) reaction uses CO_2 to produce higher value chemicals such as CH_4 and CO [8]. One of the new approaches is to produce syngas using the newly formed CO to convert it into hydrocarbons via the FT reaction. The operating conditions of the RWGS are 300 to 750°C at ambient pressure [9]. Since methanation is an exothermic reaction, it is thermodynamically favoured over the endothermic RWGS reaction at low temperatures [10]. A high-temperature favours synthesizing CO through the RWGS reaction.

The FT reaction synthesizes hydrocarbons (paraffin and olefins) as well as alcohols via polymerization reactions on the surface of the catalyst by the combination of H_2 and CO (syngas) [11, 12]. By-products such as CH_4 (methanation), CO_2 (Water-Gas Shift (WGS)) and graphite (Boudouard reaction) can also be synthesized during the polymerization [12, 13]. Cobalt (Co) and Iron (Fe) are used as active metals for the design of catalysts. These transition metals influence the selectivity of the products and the operating temperature of the FT reactor. Fe-based catalysts are activated at temperatures ranging from 290 to 360°C, referred to as High Temperature Fischer-Tropsch (HTFT) reaction [14]. They have a high activity for the WGS reaction and a high selectivity towards olefins. For Co-based catalysts, they are activated at temperatures ranging from 180 to 260°C, referred to as Low Temperature Fischer-Tropsch (LTFT) reaction [14]. They have a high activity for forming long paraffin chains (C_{5+}) used in jet fuel. For this reason, a Co-based catalyst is favourable to an Fe-based catalyst despite its higher price (0.0490 USD g^{-1} for Co, 0.000123 USD g^{-1} for Fe) [15]. The selectivity of the catalyst can be modified by adding a promoter. The promoters currently used for Co-based catalysts are noble metals such as Ruthenium (Ru), Platinum (Pt) and Rhenium (Re). The prices of these noble metals are expensive, causing high expenses for the scale up of the FT reactor (21.870 USD g^{-1} for Ru, 35.790 USD g^{-1} for Pt, 2.844 USD g^{-1} for Re) [15, 16]. Substituting these noble metals with a metal having a similar activity and being more economical to produce low-cost jet fuel from syngas is an interesting challenge that this research project will address.

1.2 CO_2 to Jet fuel

Converting atmospheric CO_2 into jet fuel (Figure 1.1) would reduce the carbon footprint of the air transport sector. Considering that it represents 2% of the world's GHG emissions, this would be equivalent to converting 720 MT of waste CO_2 into a usable product [17].

Atmospheric CO_2 produced by the plants combined with green H_2, produced by Quebec hydroelectricity, is used as feedstock to power the RWGS reactor [18]. The formed CO combined with green H_2 feeds the FT reactor to form jet fuel. Due to the advancement of CO_2 capture technologies [19], the emissions produced by airplanes could be captured to feed the RWGS-FT process again, significantly reducing the carbon footprint of airlines.

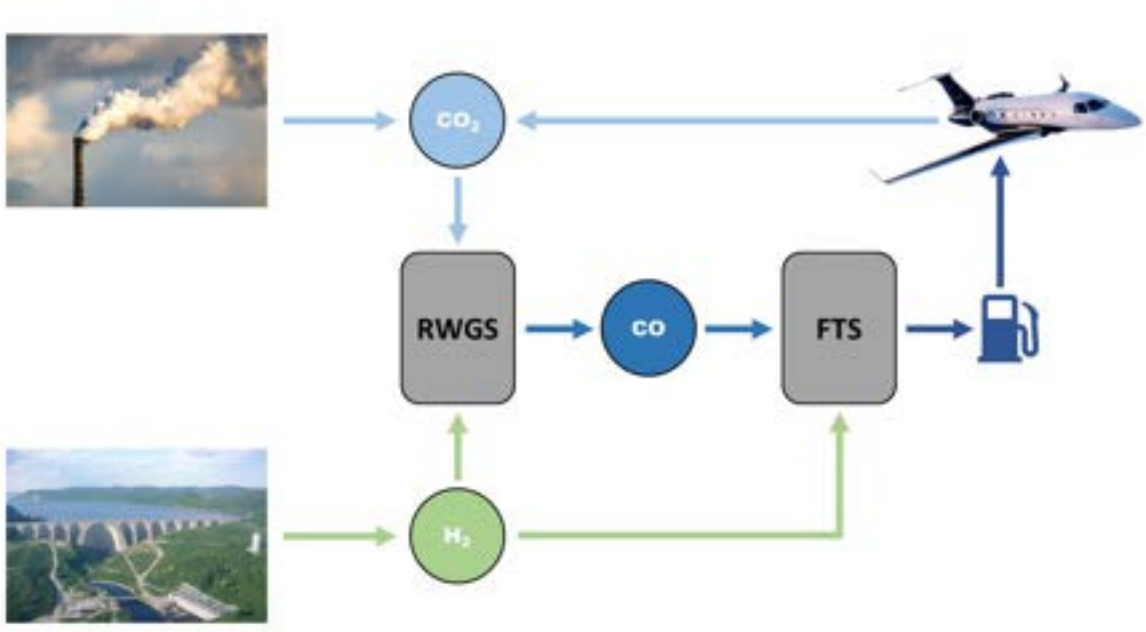

Figure 1.1 Conversion of CO_2 to jet fuel using Reverse Water-Gas Shift reaction and Fischer-Tropsch synthesis

1.3 Research Hypothesis

This research hypothesizes that the use of Copper (Cu) as a promoter would be an economical alternative to Ru and other noble metals, as it would keep Co, supported on Al_2O_3, active by keeping it reduced to preserve its metallic active phase during Fischer-Tropsch synthesis (FTS).

1.4 Objectives

This research project focuses on the effects of Cu as a promoter of paraffin synthesis from syngas (H_2 and CO) in FTS. The established objectives will confirm or disprove the hypothesis of this research:

1. Synthesize a series of catalysts impregnated with Co NPs doped with Cu NPs in order to evaluate the performance of Co, to keep it metallic in its active phase by Cu, in converting syngas (H_2 and CO) into jet fuel during FTS.

2. Optimize the wt % of Cu to be doped on the catalyst to maximize CO conversion and

its selectivity for C_{5+} paraffin during FTS while minimizing CH_4 formation.

3. Establish a relationship between the physicochemical properties of the catalysts and their performance based on the results obtained in objective 2 for the FTS.

4. Design a computer model with the results obtained in objective 2 on Python to identify the optimal wt % of impregnated Cu to maximize the selectivity of C_{5+} paraffin.

1.5 Thesis Outline

- Chapter 2 is a literature review of the notions raised in the article presented in Chapter 4. Effects of metals and supports during FTS, activation and deactivation of the catalyst, and Metal-Support Interactions (MSI) are some of the notions that will be discussed.

- Chapter 3 explains the methods taken in this research project to ensure that the objectives presented in Chapter 1 are met.

- Chapter 4 presents the results on the Cu effect promoted on a Co-Al_2O_3 catalyst.

- Chapter 5 offers the conclusions of this research project, as well as the limitations and future works

CHAPTER 2 LITERATURE REVIEW

2.1 History of Fischer-Trsopch Synthesis

In 1926, German scientists Franz Fischer and Hans Tropsch invented a process to convert coal into synthetic liquid hydrocarbons. Fischer and Tropsch's process involved hydrocracking coal by reacting it with steam to produce syngas (a mixture of H_2 and CO). At a pressure ranging from 1 to 10 atm and a temperature ranging from 453 to 473 K, this syngas produced liquid hydrocarbons when interacting with a Co catalyst, produced by Fischer and Tropsch [12]. Through the diversity of its feedstock, this process can convert coal to liquid, gas to liquid, biomass to liquid, and energy to liquid to produce a range of products such as gasoline, diesel, and jet fuel [20, 21]. The interest in the Fischer-Tropsch (FT) process has increased during the last years since it allows to answer the energy demand with the potential of it being carbon neutral when paired with renewable electricity, making it an attractive solution for Canada as well as for the 120 countries that have the objective to reach carbon neutrality by 2050 [22, 23].

2.2 The Fischer-Tropsch Synthesis mechanisms

The Fischer-Tropsch Synthesis (FTS) is a complex reaction implying surface polymerization reactions that occur when the syngas comes into contact with the catalyst *in situ* to produce saturated and unsaturated hydrocarbons and alcohols :

$$(2n+1)H_2 + nCO \rightarrow C_nH_{2n+2} + nH_2O \text{ (synthesis of paraffin)} \tag{2.1}$$

$$2nH_2 + nCO \rightarrow C_nH_{2n} + nH_2O \text{ (synthesis of olefin)} \tag{2.2}$$

$$2nH_2 + nCO \rightarrow C_nH_{2n+2}OH + (n-1)H_2O \text{ (synthesis of alcohol)} \tag{2.3}$$

Polymerization reactions adhere to the following steps: 1) reaction initiation, 2) chain growth, and 3) chain termination. Two polymerization mechanisms are suggested for these reaction steps: CO insertion chain growth and carbide. In the CO insertion chain growth mechanisms (Figure 2.1), a CO molecule is adsorbed on the catalyst's surface. The CO molecule's dissociation and hydrogenation initiate the chain growth, forming either CH_4 or a CH_x molecule.

The chain propagation continues by the association of a CO molecule to the CH_x molecule. The C-O covalent bond is broken by a dehydration reaction to form an initial molecule of C_2H_y, and the chain growth stage continues. When chain termination occurs, a molecule of paraffin, α-olefin, or alcohols can be formed once the molecule is desorbed from the catalyst surface [24].

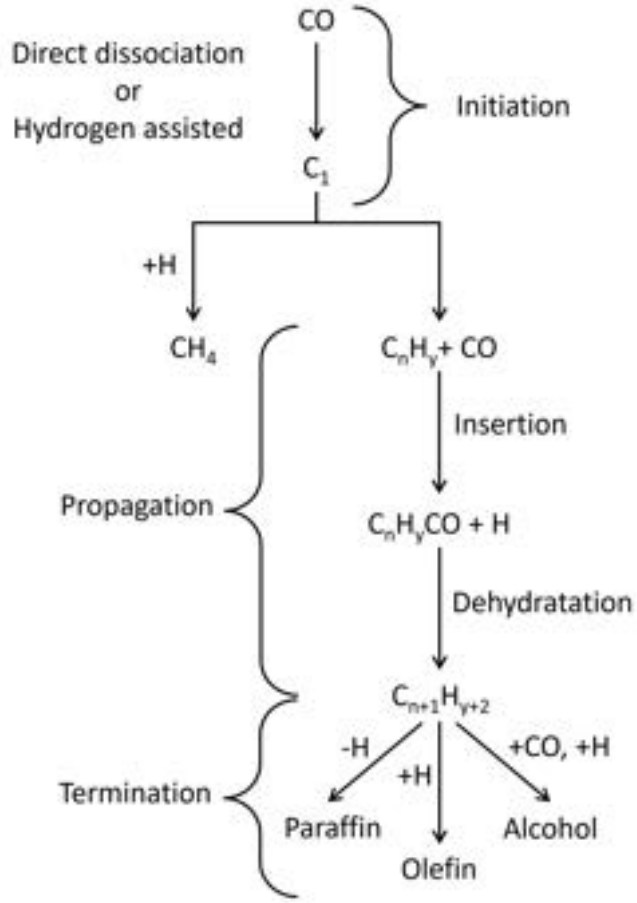

Figure 2.1 Schematic of the Fischer-Tropsch reaction according to the CO insertion chain growth mechanism. Adapted from [25]

In the carbide mechanism (Figure 2.2), chain extension begins with the formation of a methylene monomer (-CH_2-). H_2 and CO are absorbed and dissociated at the catalyst surface to allow the formation of CH_x species such as -CH_2- and -CH_3. CH_4 can be formed if the rate of transformation of CO to CH_x is not fast enough compared to the rate of formation of CH_4 from CH_x [25]. Chain growth occurs by adding these monomers, allowing the polymerization of long-chain hydrocarbons. Chain termination occurs when a -CH_3 or H species is added to form a paraffin molecule or when an H atom is removed from the chain to form an olefin molecule [26].

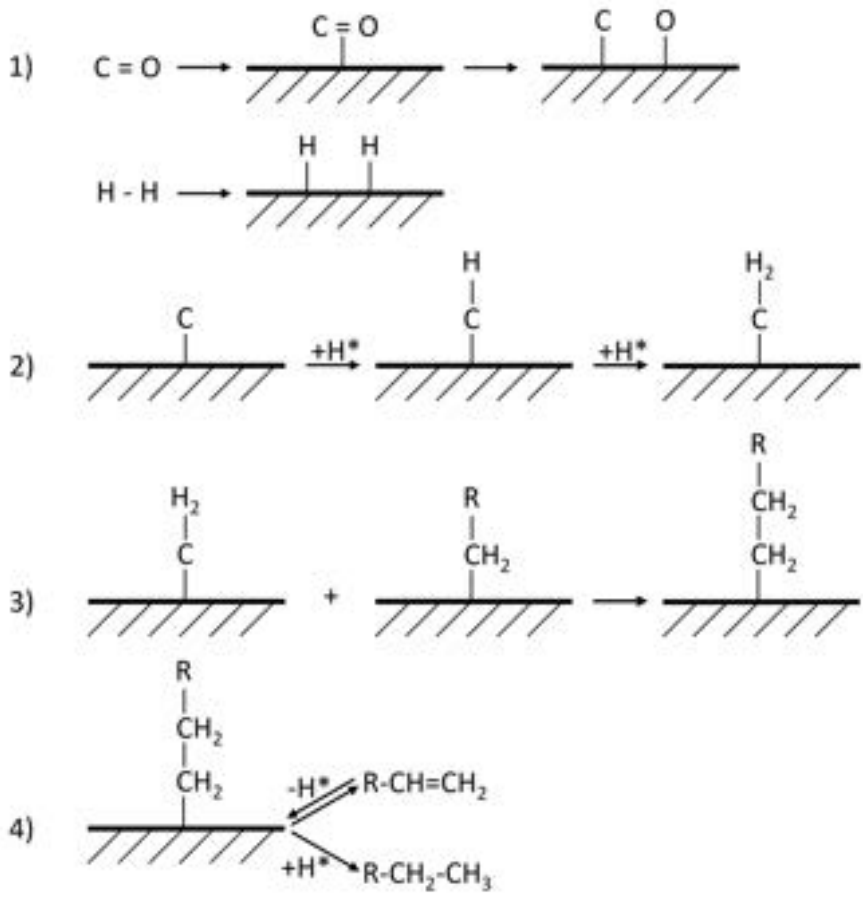

Figure 2.2 Schematic of the Fischer-Tropsch reaction according to the carbide mechanism. Adapted from [26]

2.3 Side Reactions

2.3.1 Methanation

During the FT reaction, the formation of CH_4 can occur. CH_4 is an undesirable product that can be formed during the insertion of CO insertion chain growth mechanism and carbide mechanism (Section 2.2) but also via a separate and irreversible reaction :

$$CO + 3H_2 \rightarrow CH_4 + H_2O \text{ (synthesis of methane)} \tag{2.4}$$

The combined effect of temperature, metal particle size, and the internal partial pressure of H_2 and CO fed to the reactor can influence methane selectivity [12, 13, 27].

Increasing the temperature promotes selectivity for CH_4 and decreases chain growth selectivity. The final step to form CH_4 is the hydrogenation of a metal surface -CH_3 species. Increasing the temperature will increase the rate coefficient of the hydrogenation reaction of -CH_3 and therefore decrease the surface residence time of CH_4 [28]. Since this is an exothermic reaction, controlling the reactor temperature and removing heat is essential to reduce the CH_4 selectivity [12].

As the metal particle size decreases, the number of metal particles exposed to the surface increases (increasing the surface-to-volume ratio). These metal particles on the surface readily react with H_2O to oxidize the catalyst rendering the catalyst inactive for FTS, increasing the selectivity for CH_4 [27, 29].

The formation of CH_4 is also related to the availability of H_2 on the surface [30]. Changing the internal partial pressure of H_2 and CO changes the selectivity for CH_4. For low to moderate conversion, the catalyst surface is covered with CO. When the conversion is high, the concentration of CO on the surface decreases, and this vacant surface becomes available for H_2, increasing its concentration. The increase of the H_2 concentration favours the desorption leading to the rise of the CH_4 formed [29].

2.3.2 Water-Gas Shift

The Water-Gas Shift (WGS) is an undesired reaction that can occur during the FTS process resulting in the production of unwanted products such as CO_2 :

$$CO + H_2O \leftrightarrow CO_2 + H_2 \tag{2.5}$$

This reversible reaction is influenced by the H_2:CO ratio feeding the FT reactor [12]. A high H_2:CO ratio (>1) would favour the reaction towards the left, i.e., the formation of H_2O, while a low H_2:CO ratio (0.5 - 1.4) would favour the reaction towards the right, i.e., the formation of CO_2 [31]. Fe-based catalysts are inexpensive and readily available but are active at low H_2:CO ratio, so they tend to form CO_2 in the WGS reaction [24]. Co-based catalysts have an optimal activity when the H_2:CO ratio is high, around 1.8 - 2.1, thus limiting CO_2 formation [32].

2.3.3 Boudouard reaction

The Boudouard reaction is a disproportionate reaction where CO is converted to CO_2 and a carbon element:

$$2CO \rightarrow C + CO_2 \tag{2.6}$$

The operating temperature of the FT reactor is a crucial element to the deposition of carbonaceous elements on the active phase of the catalyst since at reaction temperatures of $\geq$300°C the Boudouard reaction becomes active [33]. At this temperature, it competes directly with the FTS for CO utilization. Carbon deposition in the Boudouard reaction is low or absent in the FTS using Co-based catalysts since the operating temperature is optimal at 180 to 260°C [34]. The FTS using Fe-based catalysts operates at high temperatures (290 to 360°C) and is therefore conducive to forming carbon elements [34].

2.4 Modeling

2.4.1 Simulation

The development of scientific computer simulations allows the prediction of physical behaviours that can occur in a system using mathematical models. Computer simulations are beneficial since they can facilitate a decision-making process or provide additional knowledge about the behaviours of the physical universe [35]. Since computer simulations are created based on mathematical models, they can be applied to as many physical systems as there are mathematical models to describe them.

Advances in simulations using equilibrium equations of matter, energy, and momentum have allowed scientists to assess the impact of the type of reactor on the FTS, to represent the fluid dynamics that occur inside the FT reactor and the kinetic reactions that appear on the surface of the catalysts [36–38].

Computer simulations allow us to predict different physical behaviours before they occur, saving time, energy and money.

2.4.2 Anderson-Schulz-Flory distribution

The spectrum of hydrocarbons produced by the catalysts is broad. Among all the FT products, only the saturated hydrocarbons between C_9-C_{16} can be used to produce jet fuel [39]. Henrici-Olive and Olive applied for the first time the Schulz and Flory equations to the description of the Molecular Weight Distribution (MWD) of hydrocarbons in FTS products (n-alkanes, alkenes, etc.) [40]. Schulz's formula describes the MWD of polymers obtained by free radical polymerization, and Flory's formula describes the MWD of polymers obtained by the linear polycondensation method. The results obtained showed that the MWD of the individual monocomponent of the FTS calculated by the two formulas, as well as the formula of Anderson (1984), are identical [40]. The classical Anderson-Schulz-Flory (ASF) model can be represented by Figure 2.3 derived from the Equation 2.7.

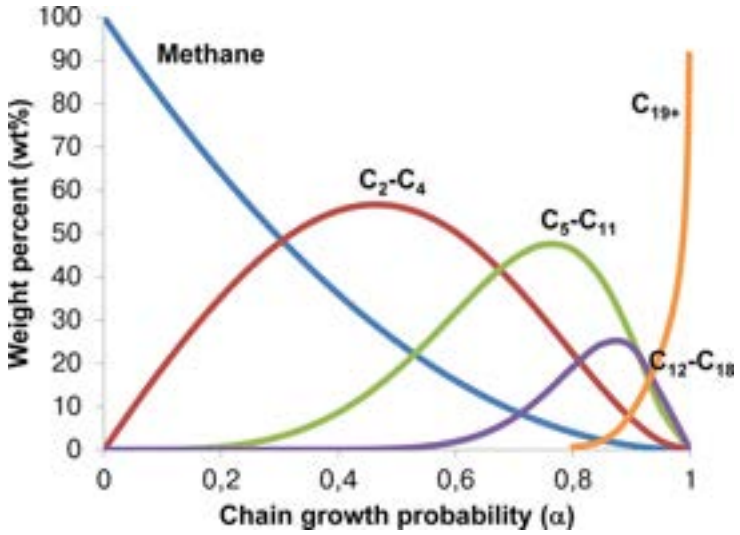

Figure 2.3 Anderson-Schulz-Flory model for the prediction of Fischer-Trsopch product distribution as a function of parameter α. Reprinted with permission from [41].

$$lg(g_n/n) = nlga + lg(ln^2\alpha) \tag{2.7}$$

where g_n is the mass fraction of hydrocarbons with the number n of atoms in the molecule and α is the hydrocarbons distribution parameter varying between 0 and 1. Because the products are formed via step-wise chain growth reactions, the product yield decreases exponentially with the chain length. ASF model estimates the relative proportions of these products with a constant chain growth probability (α) to determine the product distribution [42]. The α parameter can be influenced by: temperature, pressure, H_2:CO ratio, H_2 partial pressure, CO partial pressure and type of catalyst [40, 42].

Equation 2.8 determines the FT α where the propagation (r_p) and termination (r_t) rates are independent of chain length [40, 43].

$$\alpha = \frac{r_p}{r_p + r_t} \tag{2.8}$$

The product distribution is represented by the logarithmic mole fraction versus carbon number, which is a straight line [40, 44]. Equation 2.9 is an ideal ASF distribution who can be written as:

$$M_n = (1 - \alpha)\alpha^{n-1} \tag{2.9}$$

where the chain growth probability (α) identifies the molar fraction (Mn) of the product as a function of carbon atoms (n) [43]. The ideal ASF distribution can be modelled to predict the selectivity of a catalyst by iterating α for each hydrocarbon.

2.5 Operation Conditions

The FT technology is divided into two operating conditions: (i) Low-Temperature Fischer-Tropsch (LTFT) and (ii) High-Temperature Fischer-Tropsch (HTFT) process [45]. LTFT technology was initially used in a fixed-bed tubular reactor (Figure 2.4a) at 200 - 230°C [45, 46]. Despite operating at low temperatures, this reactor has a higher selectivity for saturated hydrocarbons and waxes than HTFT technologies while being easy to use and scale up [45, 47]. Unlike fluidized-bed reactors, fixed-bed reactors do not offer the phase mixing necessary for adequate heat control [45]. The heat exchange problem of LTFT technology can be minimized by using narrow tubes, fast syngas flow, and large catalyst particles, ensuring rapid heat exchange and minimizing exothermic temperature rise [47].

HTFT technology uses FT fluidized-bed reactors (Figure 2.4b and Figure 2.4c) for temperatures ranging from 300 to 330°C [45, 46]. This class of reactors, operating at elevated pressures and temperatures, is preferred because of its high heat exchange efficiency and ability to control the temperature of highly exothermic FT reactions through rapid, turbulent gas flow, thus ensuring superior heat transfer [47]. The fluidized-bed reactor is only suitable for the HTFT method because it operates only with solid and gas phases. At low temperatures, heavy components and liquids accumulate on the catalyst, resulting in agglomeration of the solids and loss of the fluid phase [47]. Moreover, it is difficult with this reactor to maximize the synthesis of products heavier than gasoline and naphtha since its selectivity for hydrocarbons $<C_{10}$ is about 80% [21].

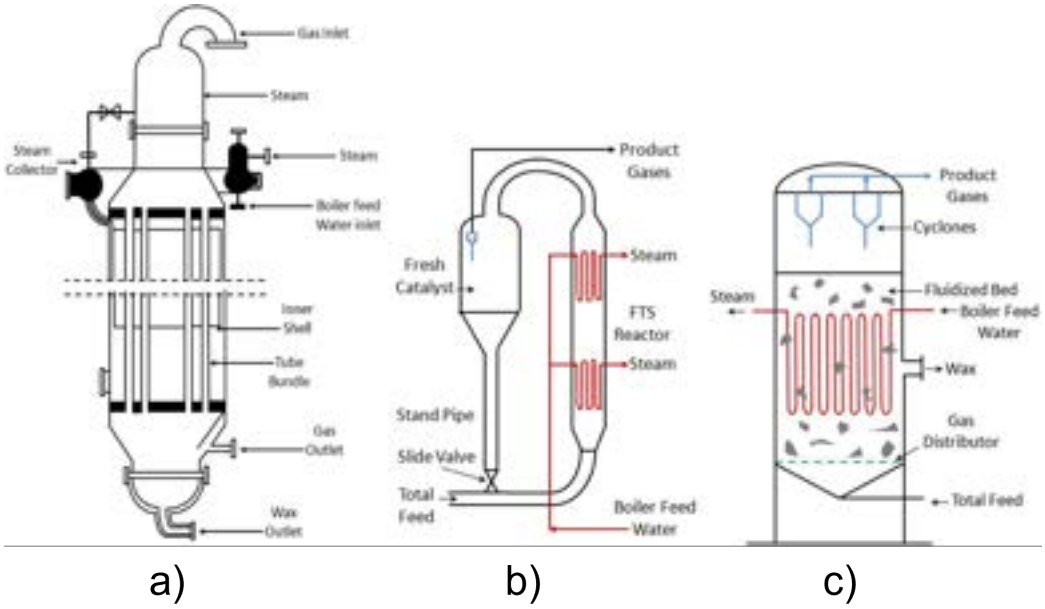

Figure 2.4 Fischer-Tropsch reactors. (a) multitubular trickle bed reactor, (b) circulating fluidized-bed reactor, and (c) fixed fluidized-bed reactor. Adapted from [46]

For both technologies, efficient heat exchange is essential to dissipate the heat generated by the multiple endothermic reactions during FTS. Too high temperature inside the reactor would increase selectivity for CH_4, carbon deposition and catalyst deactivation [46].

2.6 Catalyst Deactivation

2.6.1 Poisoning

Poisoning of a catalyst occurs when there is strong chemisorption of reactants, products or impurities on the catalyst, thereby blocking its active sites normally available for catalytic reactions and modifying the electronic and geometric structure of its surface [48]. To determine if a species acts as a poison, it is necessary to evaluate the strength of its absorption compared to the absorption of other species on the active sites [48]. The two most commonly used active metals for FTS are Co and Fe. Co-based catalysts can be poisoned by alkali metals (Li, Na, K, etc.) and sulphur (S^{2-}) [21]. Although alkali metals increase the elongation probability of hydrocarbon chains, the catalytic activity is consequently reduced [21]. It is, therefore, essential to identify the optimal concentration to optimize chain elongation and minimize deactivation by poisoning. Fe-based catalysts also undergo deactivation due to alkali metal and sulphide poisoning. However, the leading cause of deactivation of this catalyst remains the oxidation of the Fe active phase by H_2O, and CO_2 [21]. Pendyala et

al. also identified that Cu acted as a poison by obstructing the catalyst's active sites. An increase in Cu promoter resulted in a shift in average pore size to higher values, suggesting that the excess Cu had blocked smaller pore sizes [49].

2.6.2 Sintering

The sintering process is a physical and/or thermal phenomenon that causes the growth of crystals at the expense of smaller crystals due to differences in surface energy, resulting in deactivation due to the decrease in the surface area of the catalyst and the change in the surface structure [50]. Temperature, metal and support type, and the reaction environment all impact the sintering rate; water, in particular, is known to cause or speed up sintering [50]. Particle Migration and Coalescence (PCM) and atomic migration, also known as Ostwald ripening, are the two main mechanisms of sintering on supported catalysts [51]. PCM is the random movement of particles on the surface of the support. When they collide with other mobile or immobile particles, they merge to form a larger particle. Particle migration, which is strongly dependent on particle size, governs the rate of this mechanism. [51]. During the Ostwald ripening process, atomic species are released from stationary Nanoparticles (NPs). Smaller particles emit more atoms than larger ones due to the relatively higher chemical potential of their atoms, causing a net flux of atoms from smaller to larger particles [51]. This flux or transfer of atoms may occur through the vapour phase or diffusion over the support surface [51].

2.6.3 Fouling

Fouling is a type of catalyst deactivation that occurs when solid deposits from the fluid phase form on the catalyst's surface and reduce its activity due to the obstruction of the active sites and the pores [48]. One common cause of fouling is coke formation, which happens when hydrocarbons decompose on metal catalysts [48]. Coke formation can affect the activity and selectivity of Co catalysts by covering the active sites and reducing their availability for reaction, blocking the pores and preventing the reactants from reaching the active sites and altering the Metal-Support Interactions (MSI), and changing the electronic properties of Co [52, 53]. Different types of coke may have different effects depending on the catalyst and reaction conditions [52, 54]. However, the deactivation of the catalyst due to carbon deposition is reversible by an oxidation process (O_2, O_3, oxynitride), gasification (CO_2 and water steam), hydrogenation (H_2) and solvent extraction method [52].

2.7 H_2 Spillover

The Hydrogen Spillover Effect (HSPE) has been widely discussed in the literature for oxidized supported catalysts or carbon-based materials [55]. It consists of the movement of activated H species that have been adsorbed or produced on one surface to another surface that does not work under similar circumstances [11].

Nabaho et al. eagle-eyed mentioned HSPE to explain the reducing effect of Pt as a promoter on the Co-based FT catalyst. They point out that the maintenance of the reduced state of Co is due mainly to the overflow of H from Pt because the effect is more direct than the dissociation of H_2 occurring on Co. It is also pointed out that HSPE increases CH_4 selectivity and Tunrover Frequency (TOF) because Pt creates an H-rich environment [56].

The term HSPE has also been used in FTS to explain the function of noble metals (Pt, Ru, and Au) as promoters promoting Co reduction in Co/Al_2O_3 or Co/C catalysts. The atomic HSPE during FTS on Co/Al_2O_3 catalysts can result in higher CH_4 and rate of TOF [55]. H_2 spillover can occur via one of two mechanisms: (i) primary (Figure 2.5a) or (ii) secondary (Figure 2.5b). It was noted that primary H_2 spillover enhanced cobalt oxide (Co_3O_4/CoO) reducibility in contrast to secondary H_2 spillover because of the close contact between Ru and Co particles, which encourages the quick migration of H species from Ru particles to Co_3O_4/CoO particles [11].

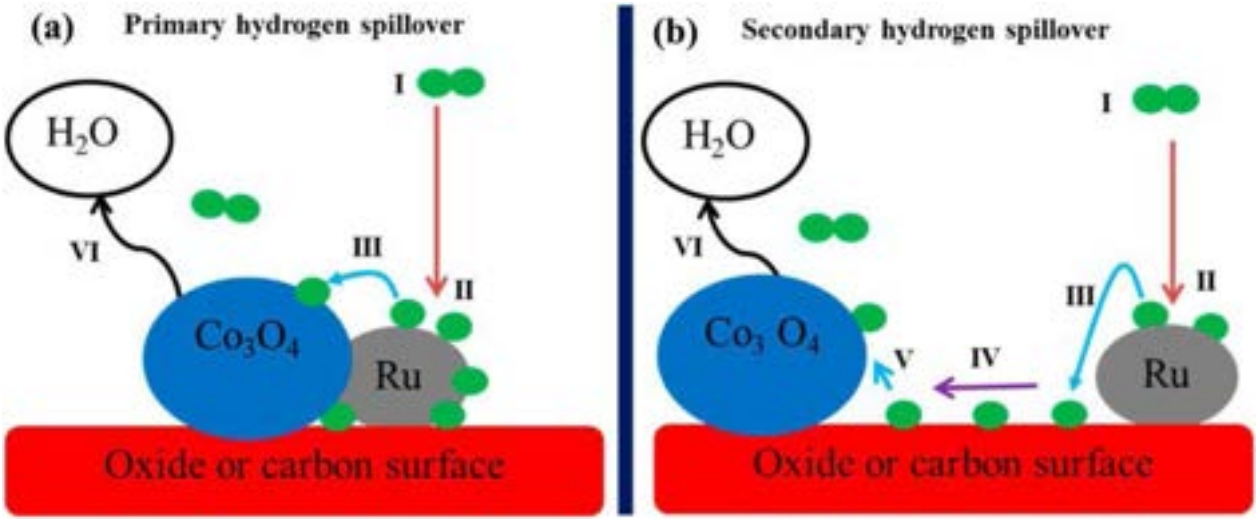

Figure 2.5 Pathways for spillover-assisted Co reduction on Ru-Co/C catalyst: a) primary; and b) secondary hydrogen spillover. (I) molecular hydrogen; (II) dissociative chemisorption; (III) spillover; (IV) hydrogen atom surface migration; (V) spillover; and (VI) reduction and water removal. Reprinted with permission from Ref. [11]

Due to the enrichment of the H environment by HSPE, the promoters seem to affect the active metals by maintaining their active form by keeping them reduced, in addition to impacting the selectivity of the molecules produced during FTS.

2.8 Catalyst

2.8.1 Active metals

The four main metals considered catalytically active in the FTS reaction are Fe, Co, Ruthenium (Ru) and Nickel (Ni) [46, 57]. Ru, despite its high catalytic activity, is inapplicable in reality because of its high price (21.870 USD g^{-1}) and low abundance (0.001 ppm in earth crust) [15,46,58]. Ni, despite its low price (0.022 USD g^{-1}), undergoes coking and is generally considered a catalyst for methanation [15, 46]. Co and Fe are therefore the most common active metals for FTS. The catalytic activity of Co is optimal at a temperature of 180 to 260°C considering that the metallic phase of Co (Co^0) is known to be the active phase for the hydrogenation of CO into hydrocarbon [14, 34]. As for Fe, its catalytic activity is maximal at a temperature of 290 to 360°C for Fe carbides recognized to be the active phase allowing the hydrogenation of CO [14, 34]. Co is a metal with a low WGS activity making it more suitable for feedstocks with a H_2:CO ≈ 2, such as natural gas [57]. In the case of Fe, it has a high WGS activity making it more suitable for use with feedstocks with a H_2:CO ≈ 1 ratio, such as coal and biomass [57].

2.8.2 Supports

The active metal and promoter are deposited on the surface of an inactive substance during the production of a supported catalyst. The support allows the regulation of the structural characteristics of the active metal by dispersing and stabilizing the size of its crystallites while strengthening its resistance to thermal attrition. [59, 60]. Different categories of supports are used in catalyst design, including oxide supports (Al_2O_3, SiO_2, TiO_2, etc.) and carbon supports [43]. Metal NPs for FTS are typically supported on inert oxide supports. MSI of moderate strength are frequently preferred; otherwise, the reduction of the metal precursor would be hampered by a strong interaction. On the other hand, catalyst aggregation and deactivation will result if this contact is too weak [43]. Carbon-based materials have excellent electrical and thermal conductivity, scalable physicochemical properties, diverse structures, mechanical strength, and lightness [43].

2.8.3 Promoters

Promoters are elements that modify the properties of the active metals and, consequently, the properties of the catalyst. It changes the structure, the texture, and the electronic interactions, stabilizes and prevents the poisoning of the catalyst, which can have the effect of lowering the reduction (activation) temperature, modifying the FTS selectivity, increasing the catalytic activity and the stability of the catalyst [24, 61]. Structural promoters, such as Al_2O_3, SiO_2, ZrO_2 and TiO_2, affect the MSI by improving the dispersion and the number of active metal [24, 62, 63]. Electron promoters change the electron density at the catalyst's surface by adding or removing electron density near the Fermi level in the valence band of the metal [64]. The 2 groups of active metals generally used are Fe and Co, and the choice of the promoter depends on this group [61]. Frequently used promoters for Co-based catalysts are noble metals such as Ruthenium (Ru), Platinum (Pt), Rhenium (Re) and Iridium (Ir) [24]. Adding these noble metals as promoters increases the number of active sites. It improves the reduction of Co_3O_4/CoO species by altering the Co-support interaction by shifting the reduction of CoO to Co^0 at a lower temperature while increasing the CO conversion and selectivity for C_{5+} [24]. By doping Ru and Re, the selectivity reached 84.2% and 83.1%, respectively, for the heavy hydrocarbons C_{5+} compared to 81.7% for unprompted Co/Al_2O_3 [65]. However, accounting for their high cost, the use of noble metals as promoters should be reconsidered. It would therefore be essential to identify a promoter that would increase activity with low capital investment. Cu is a promoter typically paired with Fe-based catalysts, as it improves the reduction of Fe, increases the CO conversion and the yield of C_{5+} while being inexpensive compared to other promoters (0.008952 USD g^{-1}) [15, 66–68]. Compared to noble metals, Cu is more economical (>300% cheaper) to produce low-cost paraffin from syngas.

2.9 Synthesis Method

2.9.1 Ultrasound impregnation method

A chemical reaction occurs when reactants are subjected to an energy source (heat, light, radiation, electrical potential, etc.), allowing them to interact. The result of the reaction is intrinsically dependent on the pressure, the amount of energy supplied, and the time, which vary according to the source of energy used (Figure 2.6) [69]. Compared to other energy sources, ultrasonication generates such high pressures (500 atm) and temperatures (5 200 ± 650 K) in a short period that cannot be achieved by other methods [70].

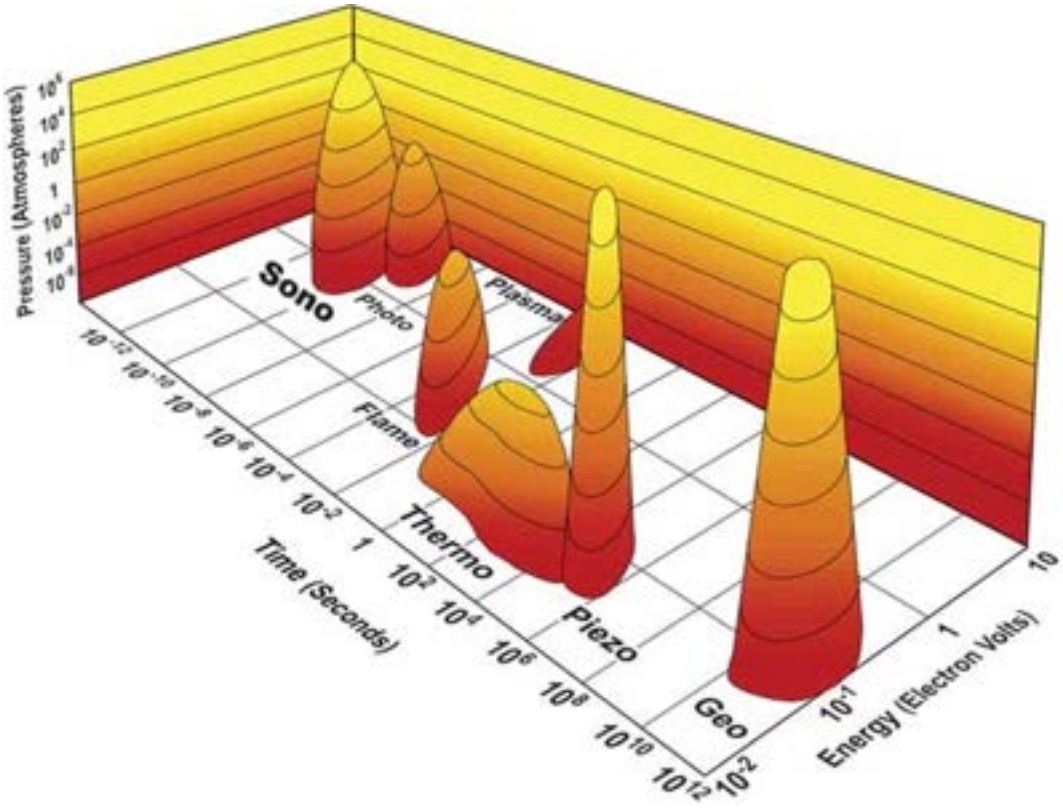

Figure 2.6 Islands of chemistry as a function of time, pressure, and energy. Reprinted with permission from Ref. [69]

2.9.2 Acoustic cavitation

Acoustic cavitation is a phenomenon that occurs when ultrasound, which is inaudible sound with a pressure oscillation frequency greater than 20 kHz, is coupled to a liquid, gas or solid medium [71]. Applying ultrasound in such media causes extreme conditions when the bubbles collapse [70]. When a liquid, for example, water, is subjected to ultrasonic waves, several microbubbles are generated due to the alternation of low-pressure (rarefaction) and high-pressure (compression) cycles, represented by Figure 2.7 [71,72]. During the rarefaction ultrasonic wave phase, many small bubbles expand because the pressure exerted on the bubble walls is greater than the pressure of the liquid [71]. During the compression phase, the pressure exerted by the liquid becomes greater than the pressure exerted on the bubble walls, causing them to collapse [71]. The energy released by the collapse of the bubbles is of such a magnitude that it can break the chemical bonds of solids, forming NPs that can be deposited on supports.

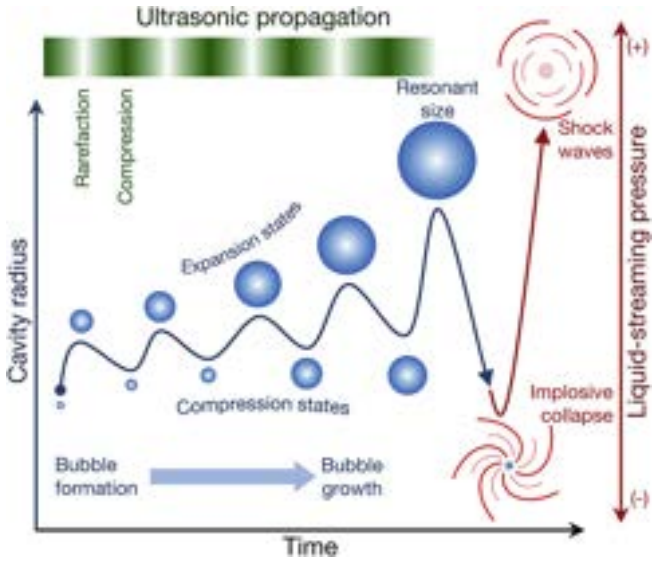

Figure 2.7 Formation of acoustic cavities due to external ultrasonic propagation and reflected shock waves after the collapse of explosives. Reprinted from Ref. [72]

A probe or a cleaning bath are the devices used to generate the ultrasound. Ultrasonic probes are specifically used to catalyze chemical reactions. However, cleaning baths can be useful for the physical effects of ultrasound, e.g. to activate highly reactive metals, generate emulsions, accelerate dissolutions of solids, facilitate crystallization and exfoliate laminated materials. [73]. The ultrasonic probe, powered by the electrical grid, converts this electrical energy into mechanical energy using a piezoelectric transducer. The acoustic waves created by this mechanical energy propagate in the liquid, creating acoustic cavitations [73].

2.9.3 Application of acoustic cavitation for catalyst synthesis

Acoustic cavitation often gives rise to numerous chemical, physical and/or mechanical effects. Sonochemical reactions include homogeneous sonochemistry of liquids and heterogeneous sonochemistry of liquid-liquid or liquid-solid systems. [73].

Homogeneous sonochemistry promotes chemical reactions by forming intermediate free radicals during acoustic cavitation. Moreover, the formed microbubbles act as a microreactor, allowing the volatile molecules to participate in chemical reactions because of the high temperature and pressure. The cavity remains spherical during the bubble collapse because its environment is uniform. As for the less volatile molecules that have not penetrated the microbubbles, they can still react due to the change in pressure associated with the propagation of the shock wave coming from the collapse of the microbubbles. Moreover, the radical species generated can also allow their reaction [73].

Chemical reactions in heterogeneous sonochemistry (liquid-liquid or liquid-solid systems) are mainly influenced by the mechanical effects of cavitation. The mechanics of cavity collapse alter significantly when cavitation occurs in a liquid close to a solid surface. Microjet impact and shockwave damage are the two methods that cause cavitation effects close to surfaces. Every time a cavitation bubble forms close to a surface, the asymmetry of the liquid's molecular motion during cavity collapse causes the cavity to distort. The potential energy of the bubble is converted into the kinetic energy of a jet of liquid that passes through the bubble's interior and impacts the surface at speeds of up to hundreds of meters per second. The energy delivered by these impacts causes the deformation of the surface, increasing its surface area [73].

2.9.4 Operation parameters

Sound frequencies are measured in Hertz (Hz), 1 Hz equal to 1 cycle per second. In sonochemistry, the ultrasound used has been studied for a wide range of frequencies, from 20 kHz to above 2 MHz. However, the use of higher frequencies requires more power because the energy is dissipated by molecular motion, and for this reason, the frequencies generally used are between 20 and 50 kHz. However, frequencies between 100 kHz and 1 MHz are of interest because they have the advantage of generating radicals (Figure 2.8) [74].

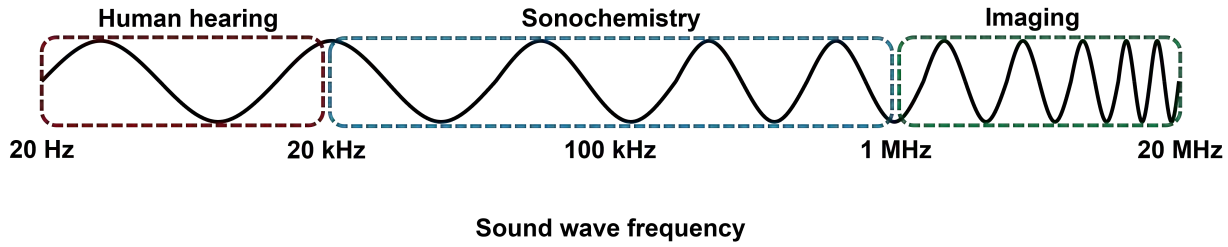

Figure 2.8 The audio frequency spectrum with their use. Adapted from [74]

The applied ultrasound's frequency and pressure amplitude can significantly affect acoustic cavitation, sonochemical reaction rate and free radical formation.

The pressure amplitude is closely related to the energy transferred to the liquid medium, which increases the acoustic cavitation number, the internal collapse temperature and the sonochemical yield. A high-pressure amplitude reduces the amount of dissolved gas below the natural limit in the liquid (degassing). It decreases the surface area of the bubbles in the medium by promoting their fusion (coalescence), limiting the effect of acoustic cavitation. Conversely, a low-pressure amplitude favours the bubble's dissolution due to too-low surface tension, limiting the acoustic cavitation effects [75].

The frequency governs the chemical reactions occurring in the medium by influencing the bubble's number, size and distribution. The reactor geometry, ambient pressure, temperature, viscosity of the medium and the gas composition of the liquid impact the effect of frequency on bubbles. A high frequency favours the formation of small bubbles via the dissociation of the liquid and gas phases (nucleation). A high frequency decreases the gas entering the bubbles by decreasing the rarefaction and compression phases. A low frequency causes an increase in the size of the bubbles due to the coalescence phenomenon limiting the effects of acoustic cavitation [75].

Since the choice of the operating frequency and the pressure amplitude of the ultrasound are intrinsically linked to the physical characteristics of the fluid (viscosity, composition, etc.) and the operating conditions (reactor, temperature, etc.), an inadequate application of ultrasound would limit the acoustic cavitation.

2.10 Characterization

2.10.1 Transmission Electron Microscopy and Scanning Transmission Electron Microscopy

Transmission Electron Microscopy (TEM) and Scanning Transmission Electron Microscopy (STEM) are two types of microscopy techniques that use electrons to form images of specimens. Through the interaction of electrons with the sample's internal structure, the TEM produces an internal image of a nanometric sample by emitting a parallel electron beam at high voltage that cross through the specimen [76]. This technique gives information on nano-dimensional structures regarding their structural characteristics, their fundamental composition and their chemical bonds [76]. However, TEM images have the disadvantage of suffering from diffraction contrast and the Fresnel effect, which can, in the case of crystalline components, generate artifacts in the reconstructions [77]. STEM imaging forms images by scanning the electron beam over the sample using deflection coils located inside the objective lens, thus avoiding the appearance of diffraction-related artifacts [77, 78]. The electrons scattered in an inelastic way (transmission electrons) due to an interaction with an element of higher atomic number appear as a white point on the image, representing the sample atoms [79].

2.10.2 Temperature Programmed Reduction

Temperature Programmed Reduction (TPR) is a characterization technique to analyze the reduction kinetics of an oxidized catalyst precursor. This technique consists of heating the catalyst by linearly increasing the temperature in a constant flow of H_2 to record the H_2 consumption [80]. Then, based on the H_2 consumed, it is possible to identify the number of reducible species and their degree of reduction by deriving the integrated H_2 consumption [80]. The TPR allows evaluation of the impact of a promoter's addition on the catalyst's reduction temperature.

2.10.3 Energy Dispersive X-ray spectroscopy

Energy Dispersive X-ray (EDX) spectroscopy is an analytical electron microscopy method based on the excitation of a sample by an electron beam and the analysis of X-rays emitted at energies characteristic of the elements [81]. When the electron beam comes in contact with an atom, two fundamental physical events occur: *elastic* and *inelastic* scattering [82]. *Elastic* scattering is a change of direction of an incident electron without detectable energy loss, caused mainly by Coulomb attraction or a collision with the atom's nucleus [82, 83]. As for *inelastic* scattering, it is an energy loss without apparent change of direction caused by an interaction between the bound electrons and the atom's nucleus [82]. The *inelastic* scattering causes the ionization of atoms. When they return to their ground state, they emit characteristic X-rays captured by a photon-energy sensitive detector [82].

2.10.4 Electron Energy-Loss Spectrometer

Electron Energy-Loss Spectrometer (EELS) is an analytical technique based on inelastic scattering of a fast monoenergetic electron in a thin specimen [83,84]. The incident electrons undergo *elastic* and *inelastic* scattering [82, 83]. The incident electrons are directed to a high-resolution electron spectrometer which separates them according to their kinetic energy to produce a spectrum of lost electron energy showing the number of electrons as a function of kinetic energy [83].

2.10.5 X-Ray Diffraction

X-Ray Diffraction (XRD) is a non-destructive technique that provides important information such as phase identification, sample purity, crystallite size, and atomic arrangement in each unit cell [85, 86]. This technique can be applied to various materials, including minerals, polymers, plastics, metals, semiconductors, ceramics, and solar cells [85]. When the X-ray

beam is projected onto a crystalline material, diffraction patterns are formed that reflect its structural and physicochemical characteristics [86]. The sample diffracts the beam at an angle that obeys Bragg's law :

$$\eta\lambda = 2d_{hlk}sin\theta \tag{2.10}$$

where η is an integer (1,2,3,...), λ is the wavelength of the incident radiation, d_{hlk} is the interplaner spacing and θ is the angle of the incident X-ray [86]. For the particles size, it can be estimated by the Scherrer equation :

$$D = \frac{K\lambda}{Bcos\theta} \tag{2.11}$$

where D indicates the size of the particle, K is Scherrer constant (0.9), λ is the XRD wavelength, B is the full width at half maximum measured in radian and θ is diffraction angle [85].

2.11 Originality of the research

This work is original for several reasons (i) We introduce small concentrations of Cu on Co/Al_2O_3 to ensure the metallic state of Co synthesized paraffin. (ii) We deposited highly dispersed Co NPs via ultrasound deposition. (iii) Compared to other papers, our catalyst minimizes the formation of alcohols. It has high selectivity for C_{5+} paraffin molecules due to the impregnation method and the Co/Cu ratio used for the synthesis. [87–89]. Synthesis of the catalyst by ultrasonic impregnation doped with 0.0015 g g^{-1} of Cu achieved a higher selectivity than that reported in the literature [90]. Promoting our catalyst with Cu generated a synergistic effect between Co and Cu to increase the selectivity to C_{5+} with the stability of at least $\sim$5 days. Doping Cu with a low amount of 0.0015 g g^{-1} increased the C_{5+} selectivity from 5% for undoped Co/Al_2O_3 to 29% for Cu. This is beneficial to replace expensive noble metals as promoters.

Several papers have developed computer models based on the ASF distribution to evaluate the hypothetical distribution of C_{5+} hydrocarbons produced in an FTS. We provided our computer model with experimental results from our catalysts to evaluate the variation of their kinetic reaction parameters. This allowed us to evaluate the impact of Cu on the production of products in the liquid phase of the FTS.

To the best of our knowledge, there is no example in the literature where the positive promoting effects of Cu on a Co-supported catalyst and where the selectivity for each catalyst is evaluated as a function of wt % via a computer model.

CHAPTER 3 METHODOLOGY

3.1 Materials

Alumina oxide (Al_2O_3, Sigma Aldrich, 205 m^2 g^{-1}), anhydrous cobalt(II) nitrate ($Co(NO_3)_2 \cdot 6H_2O$, Sigma Aldrich), anhydrous tetramethylammonium hydroxide (TMAOH, Sigma Aldrich), copper(II) nitrate ($Cu(NO_3)_2 \cdot 2.5H_2O$, 98% Alfa Aesar) and de-ionized water were used for the synthesis of catalysts.

3.2 Catalyst Synthesis

3.2.1 Ultrasonic impregnation

For synthesizing the Co15-Cu0.25 catalyst, 0.89 g of $Co(NO_3)_2 \cdot 6H_2O$ was mixed with 70 mL of water containing 0.08 M TMAOH for ∼10 min. A two-step deposition method was followed, where Co was first deposited on Al_2O_3, followed by Cu on Co/Al_2O_3. Sequential impregnation of Co and Cu prevents alloying and promotes NPs formation, by first making Co nanoparticles and then doped with Cu. The solution had a final pH of 12. 1 g of Al_2O_3 was added into the Co solution. A Sonics & Materials, Inc 500 W (19.4 kHz) nominal power ultrasonic processor and a solid probe (1.3 cm tip diameter, 25.4 cm length) sonicated the solution containing Co, H_2O, TMAOH, and Al_2O_3 for a 4 h cycle of 2 s on and 2 s off under vigorous mixing. 0.0094 g of $Cu(NO_3)_2 \cdot 2.5H_2O$ was added into the solution, and the 0.01 M of $TMAOH/H_2O$ solution adjusted the pH to 12. The solution was sonicated for 2 h, cycling 2 s on and 2 s off under vigorous mixing to deposit Cu on Co/Al_2O_3. Figure 3.1 represents the set-up used for ultrasonic impregnation, where the chemical elements are deposited in the three-opening vessel, which is then attached to the ultrasound probe. Table 3.1 shows the formula of each synthesized catalyst and the names that will be used to refer to them. The steps to calibrate the ultrasound probe are described in Appendix A.

Table 3.1 Catalysts nominating

Catalysts name	Catalyst formula
Co15	Co 15% on γ-Al_2O_3
Co15-Cu0.05	Co 15% and Cu 0.05% on γ-Al_2O_3
Co15-Cu0.15	Co 15% and Cu 0.15% on γ-Al_2O_3
Co15-Cu0.25	Co 15% and Cu 0.25% on γ-Al_2O_3
Co15-Cu0.50	Co 15% and Cu 0.50% on γ-Al_2O_3
Co15-Cu7.50	Co 15% and Cu 7.50% on γ-Al_2O_3
Cu15	Cu 15% on γ-Al_2O_3
Co-Ru	Co and Ru on γ-Al_2O_3

Figure 3.1 Ultrasound set-up

3.2.2 Drying and calcination

The solution was filtered to remove the water and dried in an oven at 100°C for 12 h. The resulting catalytic powder was calcined at 350°C for 4 h to remove products leftover from the synthesis. The calcined catalyst was grounded into a fine powder via a mill before being loaded into the reactor.

3.3 Characteristic of the catalysts

A Transition Electron Microscope (FEI Titan3 80-300 TEM), operating at 300 keV, imaged the catalyst's detailed morphology and CoCu Nanoparticles (NPs) size. The TEM operates with a monochromatic field emission gun and a CEOS probe aberration corrector. The fundamental composition of the catalysts was analyzed by spectrometers (Gatan Imaging Filter) via Electron Energy Loss-Spectroscopy (EELS) and Energy Dispersive X-ray (EDX) (EDAX spectrometer). Scanning Electron Microscopy Energy Dispersive X-ray Spectroscopy (SEM-EDS) was used to detect the catalyst's elemental concentration and represent the metal dispersion on the support material. X-Ray Diffraction (Bruker D8 Advance XRD configured in Brentano Bragg geometry (theta-theta)) provided the catalyst's chemical composition and oxidation state. The XRD instrument was configured with a Co X-ray tube and a position-sensitive detector (VÅNTEC-1) operating at 40 kV and 40 mA. XRD patterns were collected at 2θ ranging from 10° to 90°, and a 0.02 step size, with a count of 2 s per step. Temperature Programmed Reduction (TPR) (Altamira AMI-300HP, Georgia, US) determined the reduction temperature for all catalysts with a 10% H_2/Ar mixture and 10°C min^{-1}.

3.4 Fischer-Tropsch experimental bench scale tests

The tests were carried out on the lab scale on a CATLAB Hiden module (model HAS-037-001). The furnace and the Mass Flow Controllers (MFCs) were controlled from the CATLAB software. The reagent bottles are connected to high-capacity 0 - 275 bar pressure regulators. The feed is then connected to MFCs which control the flow of reagents into the reactor. The reagents are then fed to the reactor, a stainless steel pipe with an internal diameter of 8 mm, to react with the catalyst inside. The reactor is located inside an electric furnace, where the temperature is controlled by a type-K thermocouple placed 5 mm above the catalyst directly in the reactor. A pressure regulator located at the outlet of the reactor allows controlling the pressure of the FT reactor. Two pressure gauges, located upstream and downstream of the reactor, read the pressure inside the FT reactor. The gas leaving the reactor is cooled by natural convection. The product's gas remains gaseous at room temperature while the C_{5+} hydrocarbons are condensed, flowing into the vessel tank, and collected as a liquid (Figure 3.2).

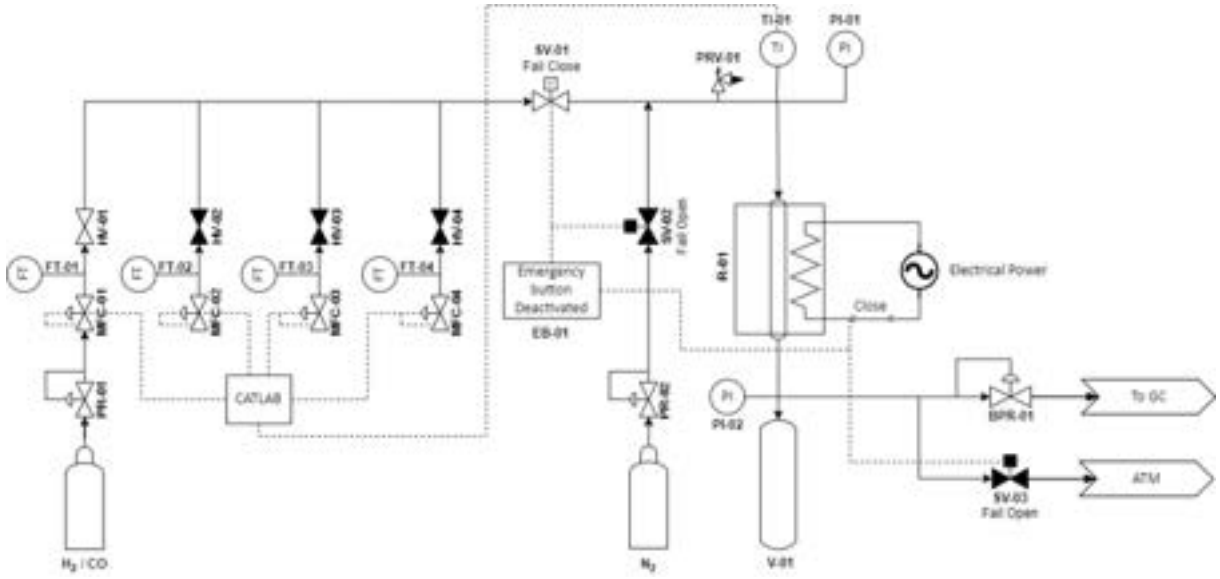

Figure 3.2 Schematic representation of the Fischer-Tropsch test set-up. The CATLAB software controls the temperature and flow rate feeding the FT reactor.

A Gas Chromatograph (GC) Thermal Conductivity Detector (TCD) and Flame Ionization Detector (FID) (Bruker Scion Instruments 456 GC gas) calibrated for CO and CH_4, respectively, analyzed the product's gas at 120-minute intervals during steady state conversion. The liquids produced by the FT reactor are placed in a refrigerator to solidify the upper phase, corresponding to the C_{5+} hydrocarbons. The C_{5+} hydrocarbons are separated, purified and diluted in toluene. The detailed procedure of separation and purification of liquid is presented in Appendix B. The liquid is measured by a GC equipped with an FID (Agilent 7890B) calibrated for C_{5+} straight chain paraffin. We only report results on CO conversion, CH_4 selectivity, and C_{5+} straight chain paraffin selectivity as those variables are pertinent to fuel production. The other hydrocarbons formed are reported as balance.

3.5 Fischer-Tropsch experimental test

Before the FTS, the catalysts were reduced under H_2 (composition 10% H_2, 90% Ar) for 16 - 18 h at 520°C under 100 mL min^{-1} to obtain their active phase by ensuring complete catalyst reduction. 400 mg of catalyst powder is deposited inside the reactor on a fixed-bed of glass wool. After reduction, the reactor is cooled to 180°C under H_2. Lowering the temperature before pressurizing the reactor with syngas is to avoid coke formation by the Boudouard reaction [33]. A back pressure regulator pressurized the reactor to 20 bar at a H_2:CO ratio of 2 (20% H_2, 10% CO, 70% Ar) with a feed of 30 mL min^{-1} and a residence time of 1 s.

The reagent flow rates and the residence time are defined at the standard conditions of temperature and pressure conditions defined by IUPAC (T = 273.15 K, P = 100 kPa). The residence time (Equation 3.1) is defined as the ratio of the catalyst volume (V_{cat}) to the total reagent flow ($\dot{V}$) :

$$\tau = \frac{V_{cat}}{\dot{V}} \tag{3.1}$$

The residence time has been set according to the dimensions and operating limits of the FT reactor. Due to the 8 mm diameter of the reactor, it has been identified that the maximum volume of catalyst in the center of the electric furnace without touching the thermocouple is $\sim$ 0.45 mL (volume of 400 mg of catalyst). As for the inflow of syngas, it was determined to reach a residence time fixed at 1 s, which corresponds to 0.5 mL s^{-1} (or 30 mL min^{-1}).

The choice of the operating pressure (20 bar), corresponding to the lowest operating pressure bracket, is based on minimizing the risk of leakage at the various connections of the reactor, safety concerns, and decreasing material strain [21]. The H_2:CO ratio is 2 since it is the best compromise between performance and cost for hydrocarbon synthesis and favours hydrocarbon paraffin chains [91].

Once the FT reactor was pressurized, the temperature was increased to 230°C for the rest of the test. 230°C was selected to correspond to the Co-based catalyst's median operating temperature range and to ensure Cu is active.

3.6 Outflow Measurement

The flow rate is measured by a flow meter (Restek ProFlow 6000) connected to the outlet of the FT reactor. It was thus possible to ensure that the flow rate to the reactor was constant and calibrated by checking it twice a day.

3.7 Data analysis method

3.7.1 Operating conditions of the gas chromatograph

Gases from the FT reactor are analyzed by GC Bruker Scion Instruments 456 GC gas. The concentration of CO and CH_4 are determined respectively via the TCD and FID. The response produced by the detectors is proportional to the concentration of the analyzed compound. The same volume of gas is injected into the column by the GC for each sample analysis. The sample is injected into the GC and vaporized at 200°C. The GC operates in split mode at a ratio of 30. The inert gas (He) pushes the sample into the separation column, where the oven maintains it at 40°C. The TCD and the FID operate at 150°C. Table 3.2 describes the column used for the FID detector.

Table 3.2 Brucker Scion Instruments 456 GC Columns Specifications

Detector	Modele	Size (Length × Internal diameter × Film thickness)
TCD Back	HP-Plot Molesieve	30 m × 530 μm × 30 μm
TCD Side	HP-Plot Q	30 m × 530 μm × 40 μm
FID Front	DB-1	60 m × 320 μm × 1 μm

The GC Agilent 7890B analyzes the liquids produced during the FTS. The concentration of hydrocarbons is measured by the FID, for which the surface area produced is proportional to the concentration and the number of carbon molecules constituting the hydrocarbon. During hydrocarbon analysis, the volume of liquid injected (1 μL) into the column of the GC is constant. Since the injector is maintained at 200°C, the sample is vaporized. The GC operates in split mode at a ratio of 10. The inert gas (He) pushes the sample into the separation column in an oven at 270°C. The FID operates at 300°C. Table 3.3 describes the column used for the FID detector.

Table 3.3 Agilent 7890B GC Column Specifications

Detector	Modele	Size (Length × Internal diameter × Film thickness)
FID	FS	15 m × 250 μm × 8 μm

Each chemical species is identified based on the retention times obtained during the GC calibration. The steps of the calibration for both GCs are described in Appendix C and D.

3.7.2 Calculation of the molar concentration

The area under the curve of the CO without conversion is determined during the CO calibration (Appendix C). Since the molar concentration without conversion and the corresponding area are known, it is then possible to identify the molar concentration of CO (N_{t_1}) for a specific surface area ($Area_{t_1}$) given by the GC-TCD with Equation 3.2 :

$$N_{t_1} = \frac{N_{t_0} * Area_{t_1}}{Area_{t_0}} \tag{3.2}$$

where N_{t_0} is the molar concentration without conversion, $Area_{t_0}$ is the area of the GC-TCD without conversion and $Area_{t_1}$ is the area of the GC-TCD after the start of the conversion.

As for CH_4, the molar concentration is measured using the calibration curve created during the GC of gases calibration (Appendix C). The area calculated by the GC-FID is inserted in the calibration curve equation to identify the molar concentration of CH_4.

After experimental catalyst testing, the resulting liquid sample is separated and purified according to the steps described in Appendix B. The molar concentration of the hydrocarbons in the liquid phase is measured by their calibration curves (Appendix D). The area calculated by the GC-FID for a given hydrocarbon is inserted in the calibration curve equation corresponding to the hydrocarbon to identify its molar concentration.

3.7.3 Reaction rate, selectivity, conversion, and turnover frequency

The reaction rate is expressed in mol g_{cat}^{-1} h^{-1}, where the value is the number of moles of each compound C_n, n being the carbon number, per gram of catalyst per hour.

The selectivity was calculated using Equation 3.3:

$$\hat{S}_{p/r,k} = \frac{a_{kp}}{a_{kr}} \left(\frac{n_p - n_p^{(0)}}{n_r^{(0)} - n_r} \right);\ \mathrm{n}_r^{(0)} > \mathrm{n}_r \tag{3.3}$$

where the selectivity $\hat{S}_{p/r,k}$ for a product p over a reactant r is measured from the number of moles of reactant r that formed the moles of product p over the total amount of moles of reactant r that reacted. a_{kp} over a_{kr} is the stochiometric ratio between the product p formed from the reactant r based on an element (or a radical) k [92].

The CO conversion was calculated based on the inlet and outlet molar compositions as measured by the GC-TCD (N = moles of CO) (Equation 3.4):

$$Conversion\ (\%) = \left(\frac{N_{in} - N_{out}}{N_{in}}\right) \times 100 \tag{3.4}$$

The Turnover Frequency of CO (TOF_{CO}) values was calculated using the dispersion (D) of Co (Equation 3.5). The dispersion is calculated using the average NPs obtained from the STEM images and assuming that the particles are spherical and uniform with a site density of 14.6 atoms/nm^2 [93, 94].

$$D = \frac{\pi d^2 * site\ density\ (atoms/nm^2)}{\frac{\pi d^3 \rho_{Co} N_{av}}{6 M w_{Co}}} \tag{3.5}$$

where d is the diameter of Co particles, Mw_{Co} is the molecular weight of Co, ρ_{Co} is the density of Co, N_{av} is the Avogadro number ($6.02*10^{23}$) [95]. The diameters of the particles can be found in Table 4.1. The TOF_{CO} values for Cox-Cuy NPs were calculated using Equation 3.6:

$$TOF_{CO} = \frac{R_{CO} \cdot Mw_{Co}}{x_{Co} \cdot D} \tag{3.6}$$

where R_{CO} is the molar rate of CO consumption per gram of catalyst, x_{Co} is Co loading on the catalyst, and D is the Co dispersion [95].

3.7.4 Calculation of the α parameter

The masses of the hydrocarbons constituting the liquid are calculated using the calibration curve carried out during the calibration stage (Appendix D).

The value of the α parameter is determined by plotting $\log(g_n/n)$ as a function of n, n being the number of carbon atoms constituting the hydrocarbon molecule and g_n the mass fraction. The mass fraction (g_n) is calculated by dividing the mass of a hydrocarbon n by the total mass of hydrocarbons. The value of the slope obtained corresponds to $\log(\alpha)$.

CHAPTER 4 RESULTS AND DISCUSSION

4.1 XRD analysis

Crystal patterns of the XRD profile for each catalyst are displayed in Figures 4.1a and 4.1b. On the fresh catalysts (Figure 4.1a), diffraction peaks at 31.5°, 37.0°, 59.5° and 67.0° are attributed to the Co_3O_4 (PDF 04-007-8056), peaks at 35.8°, 39.0° and 48.5° are attributed to the CuO (PDF 00-041-0254) and the peaks at 31.0° 45.0° and 67.0° correspond to γ-Al_2O_3 (PDF 00-029-0063). For the used catalysts (Figure 4.1b), the diffraction peaks at 44.3°, 51.5°and 75.9° correspond to the metallic Co (PDF 04-014-0167), peaks at 43.3°, 50.4° and 74.0° are attributed to the Cu (PDF 04-003-7262), while the peaks at of Al_2O_3 remained unchanged between fresh and used. Thus, the catalysts are metallic after the reaction, without the presence of an oxide and carbide phase. Co and Cu are NPs, and because of their amorphous form, the XRD peaks are superimposed and overlapped, which lowers the precision of the Scherrer equation to determine the size of NPs. In order to determine particle size, we used TEM and STEM images.

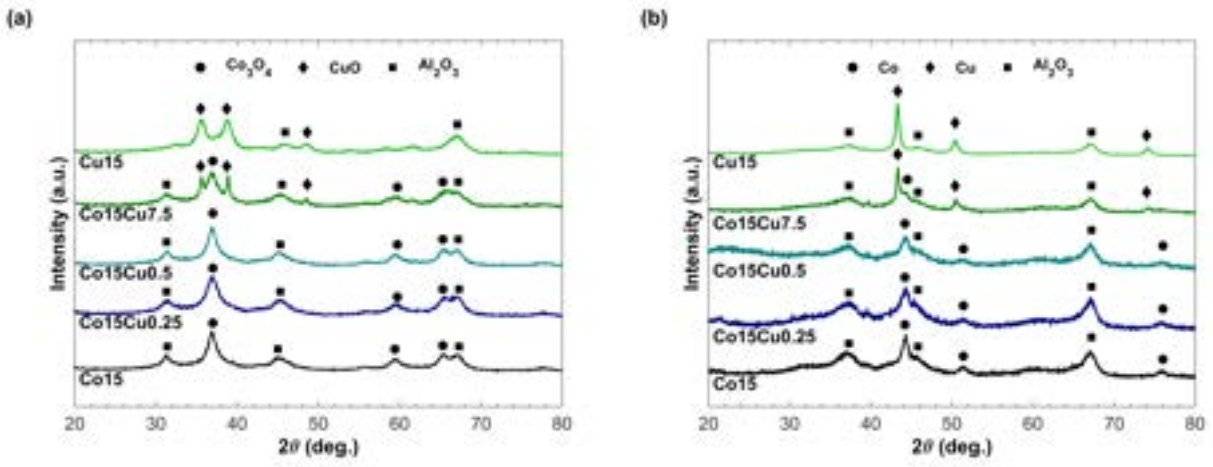

Figure 4.1 XRD patterns of (a) fresh and (b) used Cox-Cuy catalysts after 90 h of test under a 2:1 H_2:CO feed ratio

4.2 Electron Microscopy Analysis

For the Co15, the Co NPs size increases from 6.0 ± 1.4 to 11.4 ± 3.1 nm, i.e. an increase of ∼1.9 times. For Cu15, the size of the Cu NPs increases by ∼3.7 times, from 7.9 ± 2.1 nm to 29.2 ± 10.4 nm. For the Cox-Cuy catalyst, Cu is only detected in the presence of Co (Figure F.10 and F.11). Thus, the size of the Cox-Cuy catalysts NPs represents the mixture of Co and Cu (referred to as CoCu). The size of the NPs (6.0 ± 1.7 nm) for Co15-Cu0.25 catalyst is highly dispersed on Al_2O_3 represented by the white dots encircled in red (Figure 4.2a). The EELS image confirms the presence of Co but not of Cu (Figure F.4), even though Cu is detected by EDX (Figure F.10). The low amount of Cu (0.0025 g g^{-1}) can explain why it is absent [96]. After the reaction, the size of the NPs increased by ∼1.5 times to 9.2 ± 2.8 nm (represented by the red arrows in Figure 4.2b). For Co15-Cu0.50, the size of the CoCu NPs increases from 6.0 ± 1.4 nm to 10.0 ± 2.5 nm, i.e. an increase of ∼1.7 times, while the size of the CoCu NPs from Co15-Cu7.50 increases by ∼3.6 times, from 2.9 ± 1.1 nm to 10.5 ± 3.2 nm. For the bimetallic catalysts (i.e. Co15-Cu0.25, Co15-Cu0.50, Co15-Cu7.5), the CoCu NPs size increased as a function of Cu loading. All the results are presented in Table 4.1. Overall, the CoCu NPs impregnated on the support by ultrasound impregnation were 1.6 to 4 times smaller than what was previously synthesized via ultrasound. [97–100].

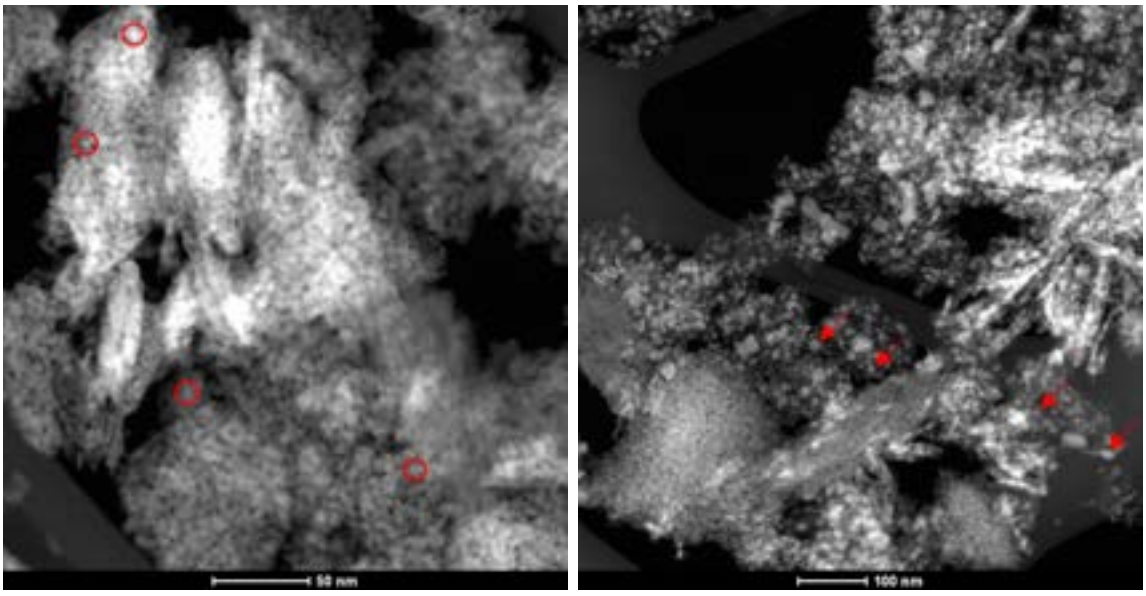

(a) (b)

Figure 4.2 STEM images of Co15-Cu0.25 for (a) fresh (6.0 ± 1.7) and (b) used (9.2 ± 2.8) CoCu NPs (indicated by the red circles and arrows)

Table 4.1 List of NPs size measured in TEM images of Cox-Cuy supported catalysts

Catalyst	NPs size fresh (nm)	NPs size used (nm)
Co15 [1]	6.0 ± 1.4	11.4 ± 3.1
Co15-Cu0.25 [2]	6.0 ± 1.7	9.2 ± 2.8
Co15-Cu0.50 [2]	6.0 ± 1.4	10.0 ± 2.5
Co15-Cu7.50 [2]	4.7 ± 1.0	10.5 ± 3.2
Cu15 [3]	7.9 ± 2.1	29.2 ± 10.4

[1] Co NPs
[2] CoCu NPs
[3] Cu NPs

The ratio of the distribution frequency of fresh to used catalysts is 1.48, 1.74, 2.24, 3.13, 4.93 for Co15-Cu0.25, Co15-Cu0.50, Co15, Co15-Cu7.5, and Cu15 respectively (Figure 4.3). Impregnation of 0.0025 g g^{-1} (Figure 4.3b) and 0.0050 g g^{-1} (Figure 4.3c) of Cu decreased the variation in CoCu NPs size compared to Co15 catalyst (Figure 4.3a). Doubling the mass of Cu from 0.0025 to 0.0050 g g^{-1} negatively affects the CoCu NPs size distribution frequency by increasing it by 18%. As for 0.075 g g^{-1} of Cu (Figure 4.3d), increased the variation in CoCu NPs size compared to Co15 catalyst. Cu15 (Figure 4.3e) showed tremendous variability compared to the other catalysts (4.93). Thus, Cu limits the size variation of CoCu NPs up to a certain threshold because, after that, Cu acts negatively by promoting the size dispersion of CoCu NPs.

Fresh Co15 consists of a mixed oxide state where its lattice of 0.20 nm, 0.22 nm and 0.29 nm correspond to metallic Co (221), CoO (200) and Co_3O_4 (220), respectively (Figure 4.4a) [101–103]. As for the used Co15 (Figure 4.4b), we find after the reaction the presence of spacing lattice of 0.20 nm corresponds respectively to metallic Co (221) [101]. The lattice spacing of fresh Co15-Cu0.25 (Figure 4.4c) is 0.23 nm, 25 nm and 0.29 nm, corresponding to Al_2O_3 (222), Co_3O_4 (311) and Co_3O_4 (220), respectively [103–105]. For the lattice spacing of used Co15-Cu0.25 (Figure 4.4d), these are 0.20 nm and 0.21 nm, corresponding to metallic Co (221) and metallic Cu (111), respectively [101, 106].

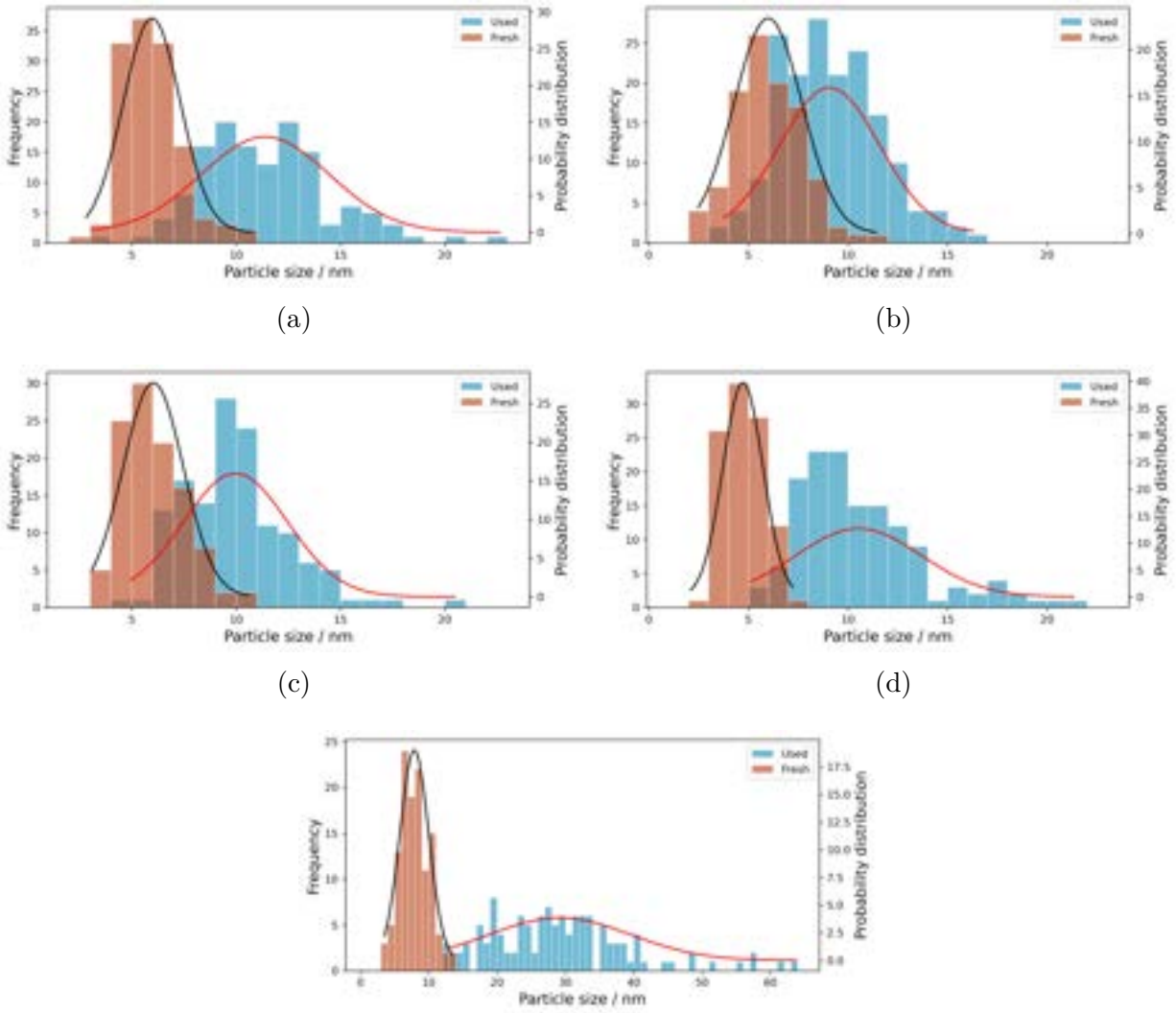

Figure 4.3 Frequency and probability distribution of Co, CoCu and, Cu NPs fresh and used samples for (a) Co15, (b) Co15-Cu0.25, (c) Co15-Cu0.50, (d) Co15-Cu7.50, (e) Cu15 based on TEM images

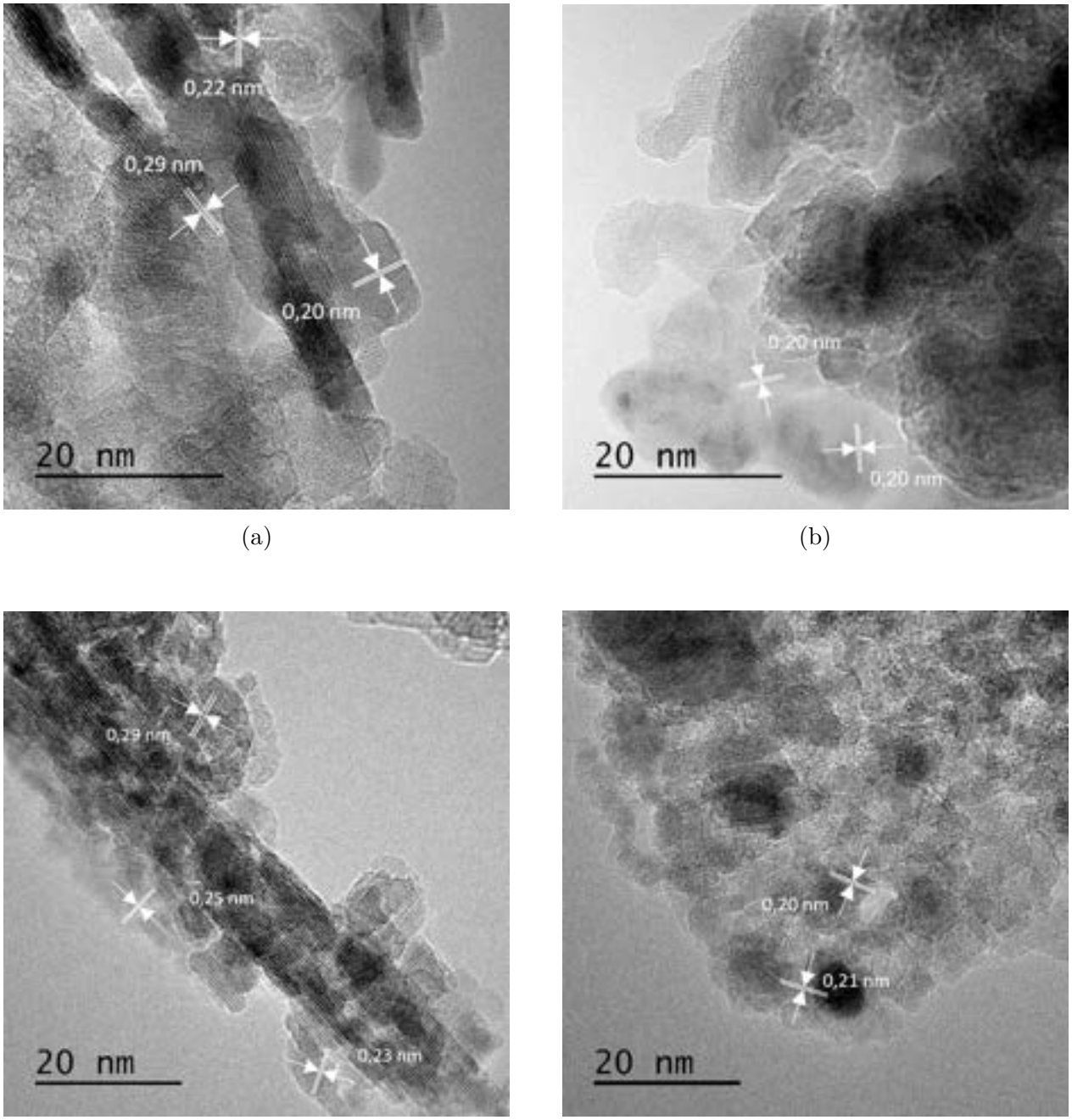

(a) (b)

(c) (d)

Figure 4.4 TEM images with d-spacing : (a) Co15 fresh, (b) Co15 used, (c) Co15-Cu0.25 fresh, (d) Co15-Cu0.25 used

4.3 H_2 Temperature Programmed Reduction

As confirmed by XRD and TEM images, the as-prepared catalysts are in their oxide state. Co15 reduces at two peaks, the first between 260 - 325°C and the second between 520 - 600°C, in line with the work of Jacobs et al. for loads of 15 - 30% Co [107]. As for Cu15, it reduces at 200°C, 60°C before Co15, remaining reduced under the reaction temperature (i.e. 220-230°C). The Co15-Cu7.50 catalyst further facilitates the reduction of Co oxide (first peak by $\Delta = 60$°C) compared to Co15-Cu0.25 (first peak by $\Delta = 30$°C) and Co15-Cu0.50 (first peak by $\Delta = 20$°C). The TPR profiles are shown in Figure 4.5.

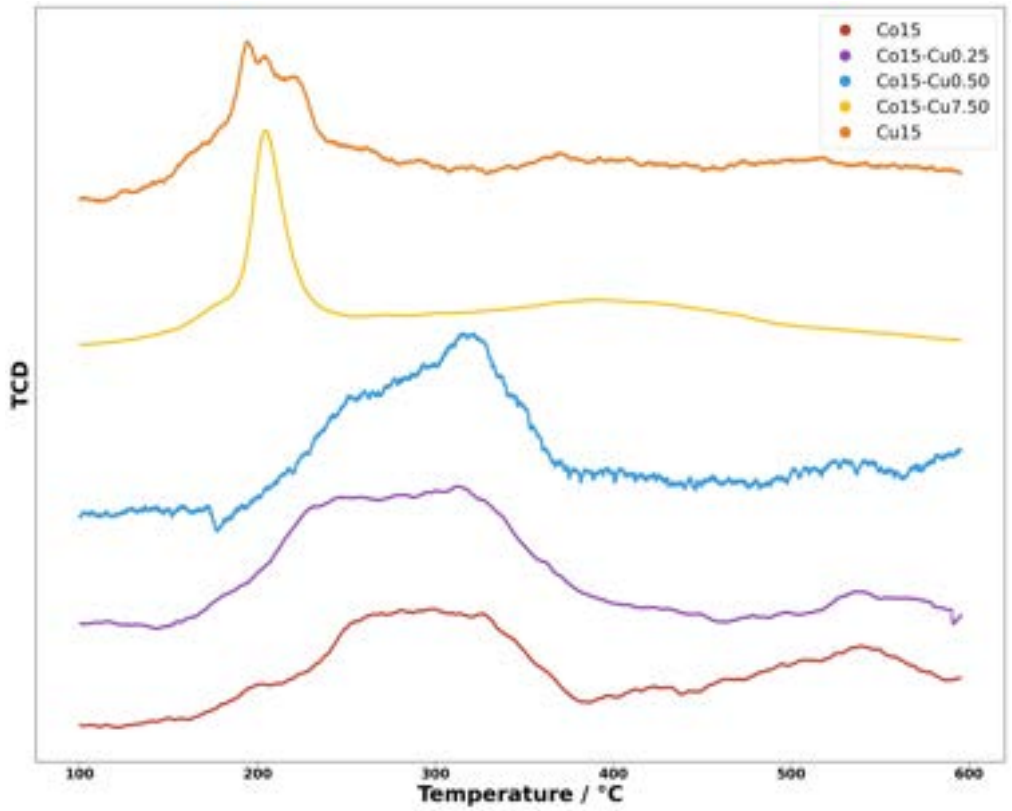

Figure 4.5 TPR profiles of used Cox-Cuy catalysts

The low-temperature peaks of H_2 consumption between 150 and 390°C correspond to the Co oxide crystallites phase reduction, ($Co_3O_4 \rightarrow CoO \rightarrow Co$) [108, 109]. Overall, Co_3O_4 follows a two-step reduction (Equations 4.1 and 4.2). The first step of Co_3O_4 reduction is difficult and is initiated at higher temperatures, causing a superposition of this step with CoO reduction [109]. The H_2 consumption peak at >400°C represents the reduction of Co that is incorporated in γ-Al_2O_3 matrix, due to the size of Co NPs (∼6 nm), which makes their complete reduction at higher temperature [107, 108, 110].

$$Co_3O_4 + H_2 \rightarrow 3CoO + H_2O \tag{4.1}$$

$$3CoO + 3H_2 \rightarrow 3Co + 3H_2O \tag{4.2}$$

The reduction temperature of the Co oxides varies with the wt % of Cu present on the catalyst, highlighting the Cu influence. The Cu-loaded catalysts reduce at lower temperatures than Co15 (260°C) and unaffected the second reduction peak at ∼500°C. Cu provides additional H_2 dissociation sites while increasing the concentration of atomic H on the catalyst surface to reduce Co_3O_4 (spillover) [111]. The Cu-doped on Co/Al_2O_3 catalysts is similar to Cu-doped on Fe/Al_2O_3 catalyst in shifting the reduction to lower temperatures and increasing the density of H [111].

4.4 Catalysts performance

All Cox-Cuy catalysts were evaluated under the same conditions: 230°C, 20 bar, H_2:CO ratio of 2 with a space velocity of 0.045 L gcat^{-1} h^{-1} and residence time of 1 s. The selectivity of the catalysts to CO and hydrocarbons differs as a function of the Cu loading. Co15 converts ∼67% of CO with a ∼34% and ∼5% selectivity to CH_4 and C_{5+} paraffin, respectively, and a mix of hydrocarbons for the balance. When 0.0025 g g^{-1} of Cu is added (i.e. Co15-Cu0.25), 68% of the CO is converted with a selectivity of ∼24% and ∼21% for CH_4 and C_{5+}, respectively. Doubling the amount of Cu to 0.005 g g^{-1} decreased the overall CO conversion to ∼39%, for a selectivity ∼34% and <1% for CH_4 and C_{5+}, respectively. Increasing the amount of Cu to 0.075 g g^{-1} wt % decreased the CO conversion to ∼7% for a ∼39% selectivity to CH_4 and balance of light hydrocarbons. As for Cu15, it converted trace CO at ∼1% and showed ∼1% selectivity for CH_4 (Figure 4.6).

Following the results obtained with Co15-Cu0.25, two catalysts were synthesized (Co15-Cu0.05 and Co15-Cu0.15) to evaluate the effects of lower Cu loading. Compared to Co15, when 0.0005 g g^{-1} of Cu is added (i.e. Co15-Cu0.05), the CO conversion and the CH_4 selectivity decrease to ∼40% and ∼18%, respectively, while the C_{5+} selectivity increases to ∼19%. Tripling the mass of Cu to 0.0015 g g^{-1} increased the CO conversion to ∼66%, for a selectivity of ∼16% and ∼29% for CH_4 and C_{5+}, respectively (Figure 4.6). The selectivity to CH_4 increased as a function of Cu loading above 0.0015 g g^{-1}.

Five of the catalysts produced C_{5+} hydrocarbons: Co15, Co15-Cu0.05, Co15-Cu0.15, Co15-Cu0.25, and Co15-Cu0.50. A Cu loading of 0.0015 g g^{-1} is the optimal loading at which it produces ∼6-times more C_{5+} than Co15. Furthermore, we compared our catalysts alongside a Co-Ru commercial catalyst which converts ∼54% of CO with a ∼19% selectivity to paraffin and a low CH_4 selectivity of ∼16%. Co15-Cu0.15 was more selective to paraffin than the commercial catalyst for a similar CH_4 selectivity.

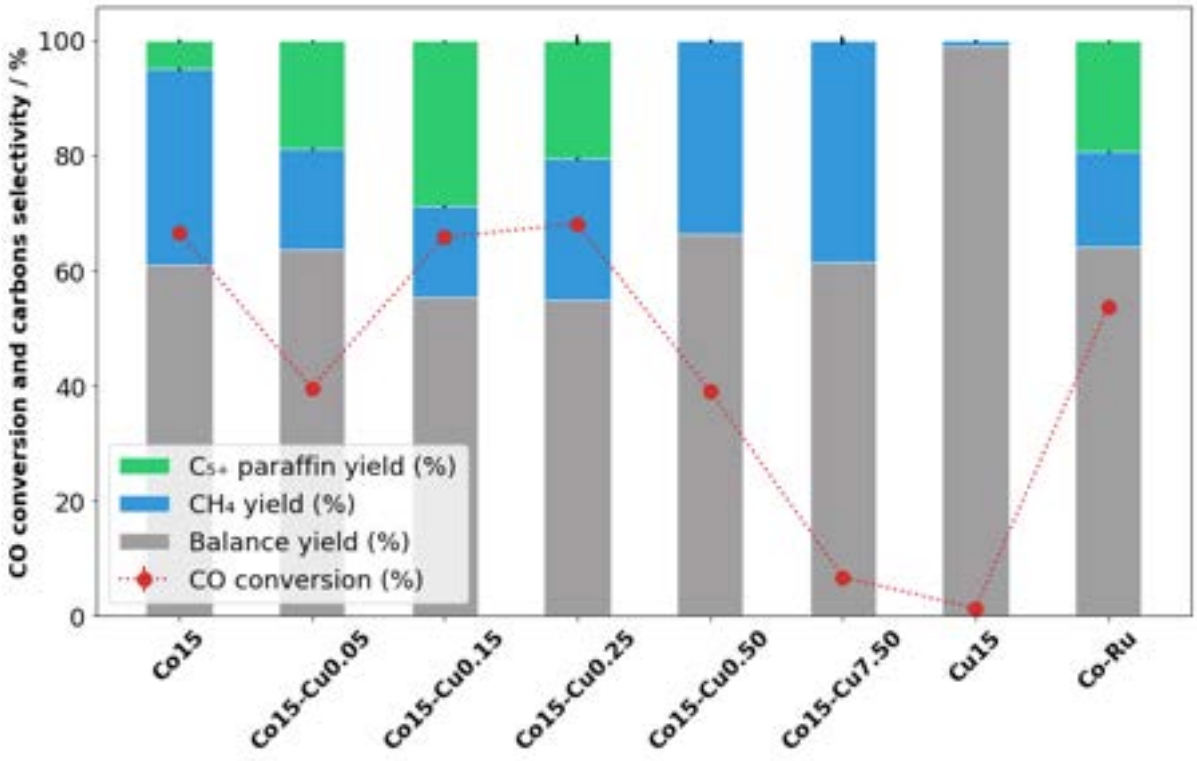

Figure 4.6 CO conversion, and selectivity for CH_4 and C_{5+} by catalyst. The standard error represented is <1%

The hydrocarbon distribution for Co15, Co15-Cu0.05, Co15-Cu0.15, Co15-Cu0.25 and Co-Ru is shown in Figure 4.7. As the C_{5+} selectivity of Co15-Cu0.50 is <1%, it was not included in the results. All catalysts have a broad distribution from C_5 to C_{18}, and peak at C_8, except for Co15-Cu0.15, which peaks at C_5 and C_7. For C_5 to C_{11} paraffin, Co15-Cu0.15 is the most selective. However, from C_{12} paraffin, Co15-Cu0.05 is more selective than Co15-Cu0.15. An impregnation of only 0.0005 g g^{-1} favours chain extension of C_{12} hydrocarbons among the catalysts. Thus, all catalysts produce hydrocarbons in the naphtha fuel range to be applied as jet fuel. Remarkably, the low loading of Cu shifted the selectivity of Co/Al_2O_3. Compared with commercial Co-Ru, Cu-promoted Co/Al_2O_3 yields more naphtha products while being more selective to higher hydrocarbons.

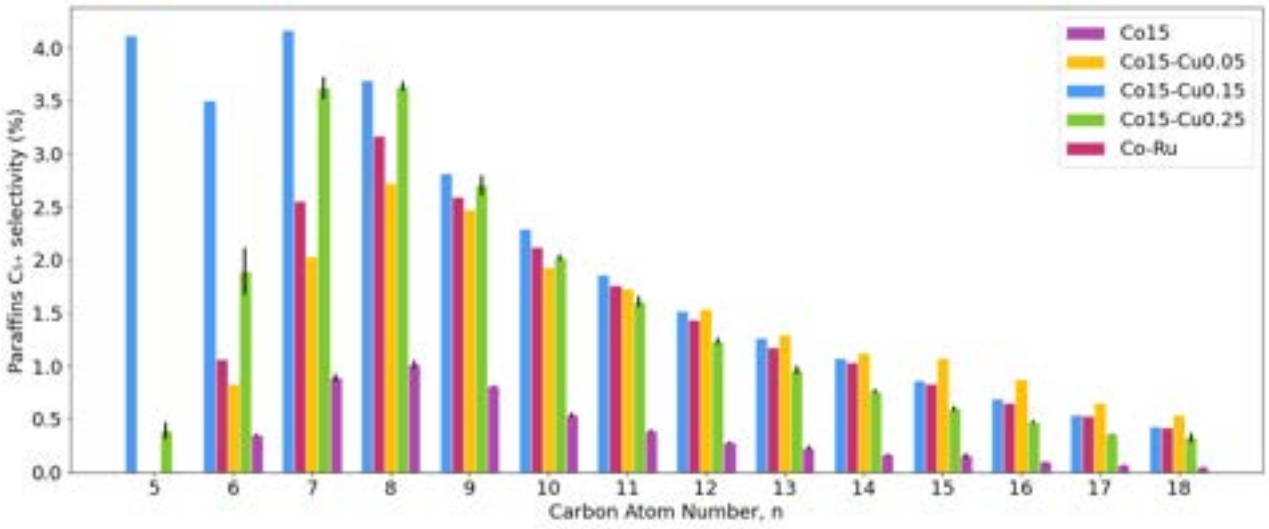

Figure 4.7 Paraffin distribution of the Co15, Co15-Cu0.05, Co15-Cu0.15, Co15-Cu0.25 and Co-Ru catalysts. The standard error represented is <0.3%

The α parameter was also calculated for each catalyst after ~5-6 days of conversion using Figure F.1 and are presented in Table 4.2

Table 4.2 The α value of catalysts

Catalyst	α value
Co15	0.725
Co15-Cu0.05	0.834
Co15-Cu0.15	0.757
Co15-Cu0.25	0.796
Co-Ru	0.797

As seen in Figure 4.7, from C_{12} paraffin, Co15-Cu0.05 has the highest selectivity. Therefore, it is logical that it has the highest α parameter since this parameter indicates the probability of carbon chain extension.

Excessive addition of Cu promoter ($\geq$0.005 g g^{-1}) covered the Co-active surface area and blocked the activity of the catalyst as Cu15 did not work on its own [49]. For Co15-Cu7.50, the selectivity to CH_4 is the majority of the product with 7% of CO converted and no selectivity to C_{5+}. At this loading (0.075 g g^{-1}), Cu covers the Co NPs, blocking its active sites accessible to CO, which decreases CO conversion and favours the formation of light hydrocarbons such as CH_4 due to the creation of an H-rich environment [56, 96]. Decreasing the Cu loading to 0.005 g g^{-1} increases the CO conversion by freeing up active sites on

Co to convert CO but did not affect the CH_4 selectivity when compared to Co15-Cu7.50. Cu can promote the catalytic properties of Co/Al_2O_3 by adsorbing and dissociating H_2 to spillover (i.e. spillover effect) onto Co [61, 112]. For Co15-Cu0.50, the spillover effect of H_2 from Cu to Co can be supplying H molecules to Co faster than it can build hydrocarbon chains, promoting the formation of light hydrocarbons such as CH_4. H_2 spillover can follow two mechanisms: (i) primary (Figure 4.8a) or (ii) secondary (Figure 4.8b). Thus, since Cu is only detected in the presence of Co (Figure F.10 and F.11), Cox-Cuy could follow the primary mechanism favouring the reduction and extension of the hydrocarbon chain due to the interaction between Cu and Co, favouring the migration of H species from Cu to Co compared to the secondary mechanism. The mechanism is speculated because if we take Co15-Cu0.25 as an example, the doped Cu (0.0025 g g^{-1}) is indistinguishable on the EELS images (Figure F.4 and Figure F.5). However, its presence is detected in EDX images only when Co is detected (Figure F.10 and F.11), which can be associated with small Cu NPs (<5 nm) or clusters on Co NPs assuming that the likely mechanism is primary H_2 spillover. Although Cu is not always detected, its effect was evaluated by comparing its activity with Co15, where there is a distinct change in catalytic activity and behaviour.

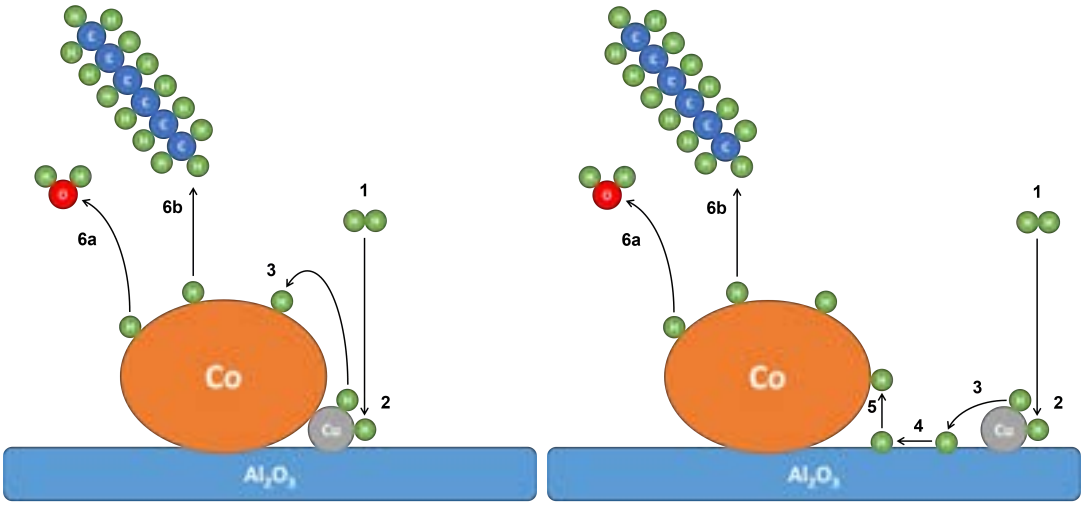

Figure 4.8 Pathways for spillover-assisted on Cox-Cuy catalyst for (a) primary and (b) secondary H_2 spillover. (1) molecular H_2; (2) dissociative chemisorption; (3) spillover; (4) H_2 atom surface migration; (5) spillover; (6a) reduction and water removal and (6b) chain growth and hydrocarbon removal. Adapted from [11]

Co-based catalysts doped with Cu <0.0025 g g^{-1} are not overwhelmed by the supply of H_2 since Cu activates H_2 into H, and Co activates CO to build heavy hydrocarbons (>C_{5+}). Without Cu, Co oxidizes to CoO/Co_3O_4 lowering C_{5+} selectivity, where H_2 is consumed to

reduce Co instead of building hydrocarbons [57]. The promotional effect of Cu ensures Co remains metallic, avoiding CO and H_2 competing for sites. The CH_4 selectivity of Co15 is similar to Co15-Cu0.50 and Co15-Cu7.50, signifying that once the threshold of Cu is passed (i.e. >0.0025 g g^{-1}), Cu decreases the catalytic activity of Co15. This is depicted by the <1% conversion of Cu15. Thus, the effect of doping Cu on Co is similar to Cu doped on Fe, which increased the selectivity to heavier hydrocarbons from ∼65 to ∼80%, and from ∼50 to ∼52% [49, 113]. The results obtained with the Co15-Cu0.05 and Co15-Cu0.15 catalysts are similar to those of Cu promoted on a Fe-support catalyst. As Co-Cu is scarce in the literature, Fe-Cu catalysts for FT were used to compare the promoting effect of Cu. Compared to the Cu-doped Fe-based catalyst, no paper to date has shown that Cu on a Co-based catalyst increased the selectivity for C_{5+} hydrocarbons paraffin.

4.5 Effect of High Dispersion

The CO conversion for all catalysts decreased slightly after 80 h under reaction conditions (Figure 4.9). Co15-Cu0.15 has the lowest deactivation rate at 0.0103 CO% h^{-1} compared to Co15 (0.071 CO% g^{-1}) and the other catalysts (Table 4.3).

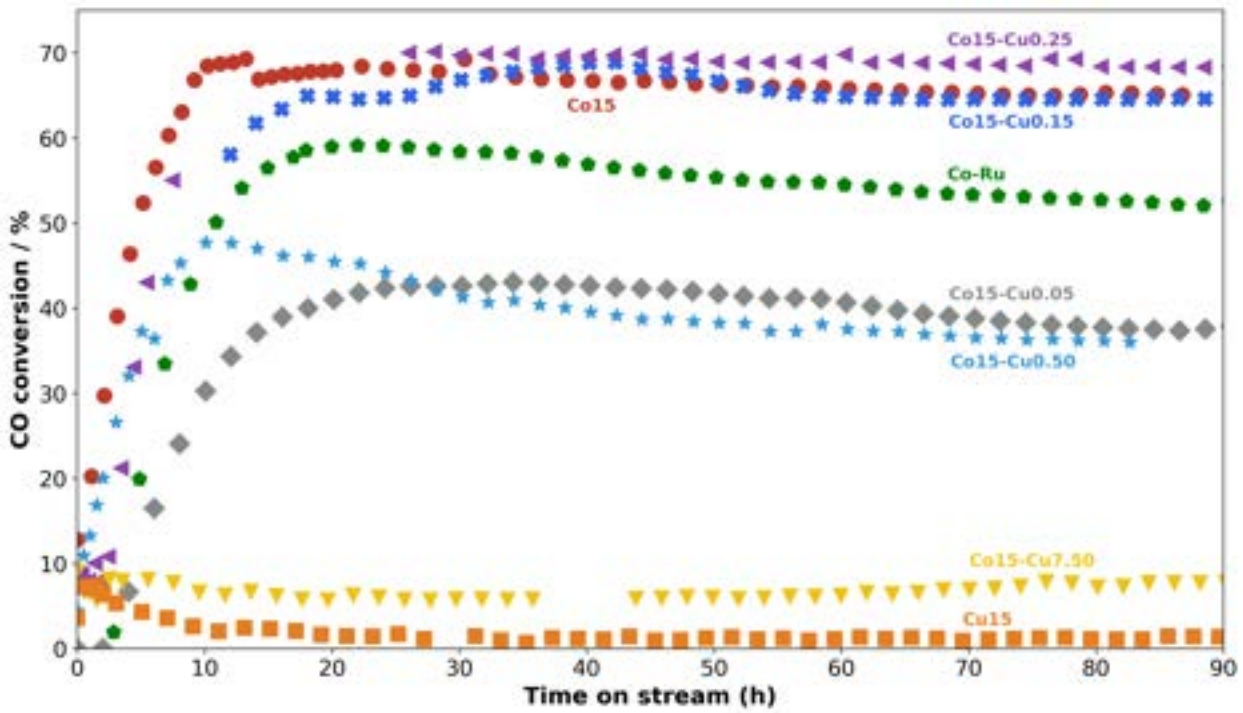

Figure 4.9 Stability of the catalysts as a function of the time on stream

From the results, adding 0.005 to 0.025 g g^{-1} of Cu decreases catalyst deactivation over time compared to other catalysts, but only Co15-Cu0.25 seems to increase CO conversion over time. Cu inhibits catalyst oxidation to promote slightly its conversion and stability over time compared to Co15. Cu thus favours hydrocarbon chain extension while having a slight, positive impact on CO conversion and stability. At 0.0005 g g^{-1} Cu (Co15-Cu0.05), CO conversion is inhibited and shows similar results to Co15-Cu0.50 catalyst. Given the amount of Cu on the Co-based catalyst, it would have been reasonable to anticipate a similar CO conversion to Co15. As a result, Co15-Cu0.05's CO conversion may be abnormal. Exceeding 0.0025 g g^{-1} Cu appears to inhibit CO conversion and promotes the deactivation of the Co15-Cu0.50 catalyst. Adding 0.005 g g^{-1} Cu results in rapid deactivation due to Cu agglomerating and sintering, obstructing the Co-active sites. As for the Co15-Cu7.50 and Cu15 catalysts, the excess Cu impregnation on the support only enhances the sintering effect. However, it is difficult to interpret these catalyst's deactivation due to the low CO conversion. As for Co-Ru, it deactivates due to pore blocking of hydrocarbons as the catalyst is a pellet (4 mm diameter). Co15, Co15-Cu0.15, and Co15-Cu0.25 are stable due to their dispersion and adherence to Al_2O_3, affiliated with the synthesis method. Sonochemical impregnation of Co on Al_2O_3 generated uniformly dispersed Co NPs decorated with Cu, minimizing the formation of large particles during the FTS (Figure 4.2a). Based on the STEM images of Co15-Cu0.25, Co15-Cu0.05 and Co15-Cu0.15 can follow the same morphology.

Table 4.3 Variation of the stability of catalysts over time

Catalyst	Variation of the conversion rate per hour (CO% h^{-1})
Co15	− 0.0709
Co15-Cu0.05	0.0028
Co15-Cu0.15	− 0.0103
Co15-Cu0.25	− 0.0576
Co15-Cu0.50	− 0.2534
Co15-Cu7.50	0.2739
Cu15	− 0.0696
Co-Ru	− 0.1379

Uniform dispersion of nanocrystals (NCs) of Co can decrease the effect of sintering, which involves the diffusion, collision and coalescence and/or bridging of metal NPs, a process known as crystallite migration and coalescence (CMC) conceptually illustrated in Figure 4.10a [114]. Figure 4.10b represents how a nonuniform dispersion of NPs facilitates the formation of NPs clusters during catalyst synthesis. When the catalyst is under FT operating conditions, it can be predicted that the NPs clusters form large crystallites on the external surface of the catalyst particles [114].

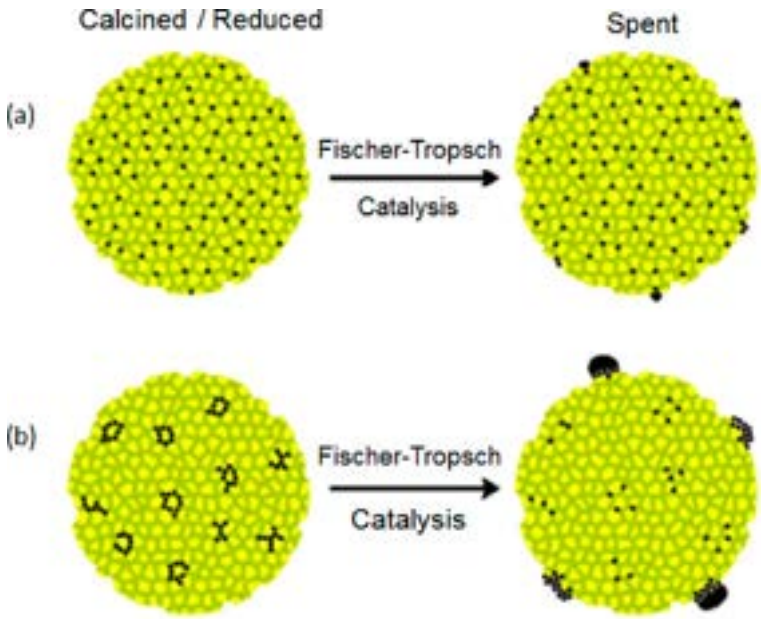

Figure 4.10 Conceptual drawing illustrating effects of (a) uniform and (b) nonuniform spatial distributions of Co NCs on their resistances against sintering via CMC during FT synthesis. Reproduced with permission from Ref [115]

The ultrasonic impregnation of Cox-Cuy on the support favours the stability of the catalysts over a long period due to the formation of NPs and high dispersion of the active phase on the support allowing a greater degree of reduction of this phase [97, 98].

4.6 Metal-Support Interaction (MSI)

The properties of Cox-Cuy catalysts depend on their morphological geometry and surface composition as this alters the synergy between Cu and Co. This synergetic effect is functionally equivalent to the metal-support interaction, where Cu spillovers H_2 onto Co [11]. The values of the Turnover Frequency of CO (TOF_{CO}) were calculated using the Equation 3.5 and 3.6. From Equation 3.5, the dispersion of Co15, Co15-Cu0.25, Co15-Cu0.50 and Co15-Cu7.50 is 8%, 10%, 10%, 9% and 4% respectively. Figure 4.11 is the TOF_{CO} of all

the tested catalysts calculated with Equation 3.6. It represents the amount of mole of CO converted per mole of Co (Co15, Co15-Cu0.25, Co15-Cu0.50, Co15-Cu7.50), or Cu (Cu15), per second for each hour. The Co15 catalyst has the highest TOF_{CO} due to the absence of Cu on this catalyst, several active sites are available to perform the CO conversion. Jacobs et al. stated that the drop in TOF_{CO} is due to the blocking of Co with Cu [96]. As for the other catalysts, the TOF_{CO} decreases proportionally as the loading of Cu increases. This phenomenon is explained by Cu blocking of Co sites, which does not always result in lower catalytic activity. While the TOF_{CO} for Co15 is greater than Co15-Cu0.25, its CO conversion is lower and affiliated with the particle size of Co.

Although TOF_{CO} is reduced by the impregnation of Cu NPs, it remains essential as it promotes hydrocarbon chain prolongation.

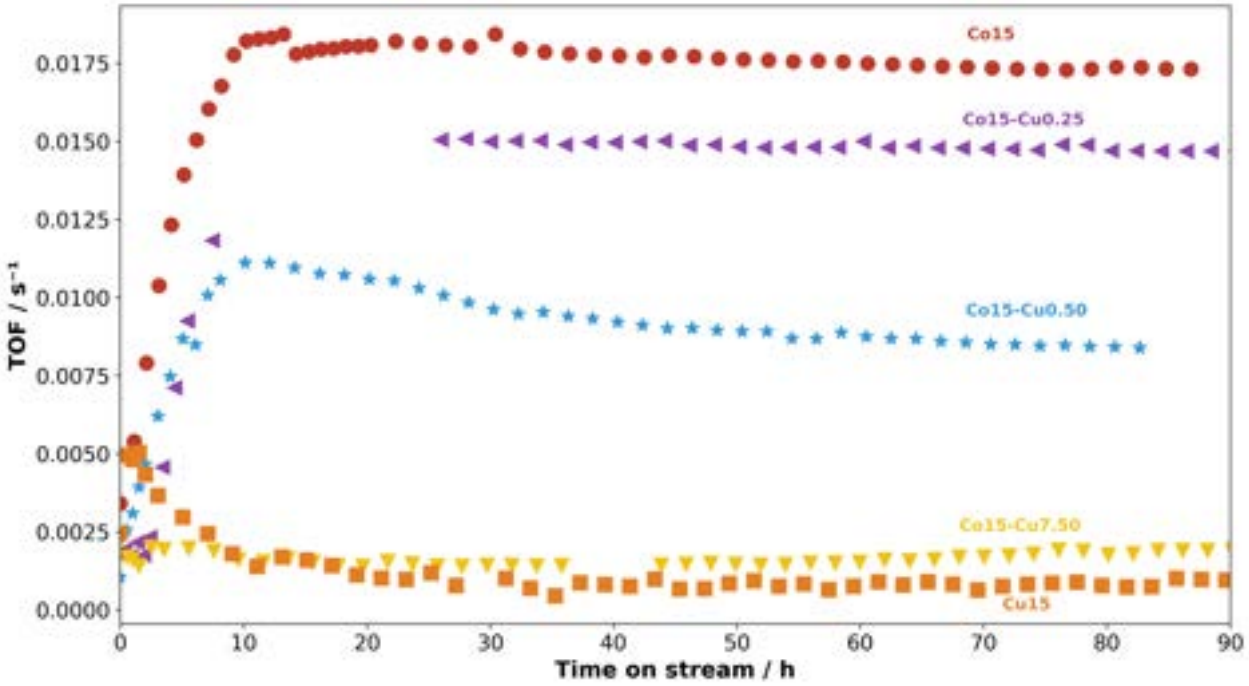

Figure 4.11 Turnover frequency of all tested catalysts over time. H_2:CO ratio of 2:1 and a flow rate of 30 mL min^{-1}

4.7 Apparent kinetic study of FTS

The models developed by Fernandez et al., Lee et al. and Todic et al. were evaluated for the reaction kinetics of the FT to represent the distribution of products.

The objective of Fernandez et al. was to propose a model to represent the distribution of products as a function of reaction conditions based on the polymerization kinetics of chains during the alkyl and alkenyl mechanisms for FTS. The model of Fernandez et al. was reproduced but the simulation diverged from our experimental results due to the different operating conditions for the Cox-Cuy catalysts. The H_2:CO ratio used in our tests is $\sim$2 times higher than the one used by Fernandez et al. where they used a Fe-based catalyst [116]. As for Lee et al. they incorporated into their model, the effects of catalyst size, catalyst active sites and reactor configuration on product distribution. By modifying the operating conditions such as temperature and pressure of the two-phase FT reactor, they optimized the yield of hydrocarbon products. It was impossible to validate the model of Lee et al. with our experimental results as it diverged from the operating conditions and reaction kinetic parameters as they used a Fe-based catalyst [117]. Todic et al. confirm the theory that taking the desorption of olefins into account as a function of chain length in the elongation mechanisms develops a kinetic model capable of reproducing the product distributions discovered experimentally. The model they developed uses the Langmuir-Hinshelwood-Hougen-Watson approach based on the CO insertion chain growth mechanism to identify the distribution of products such as paraffin and olefin [118]. Their model was applied to a Ru-impregnated Co-based catalyst for a stirred tank FT reactor. Despite the use of a different reactor and promoter, the use of this model is applicable as it employs Co as the active metal at a temperature (230°C), pressure (15 bar) and H_2:CO ratio (2.1) similar to the experimental conditions used to test Cox-Cuy catalysts, making it a good starting model to evaluate the effects of Cu. The kinetic study of the FTS is based on the model developed by Todic and al. assumes that the reaction mechanism is the same [118, 119]. The model uses differential and algebraic equations based on mass and population equilibria. The objective was to predict paraffin production in function of the catalytic composition. The kinetic steps of the FTS followed in the model include (1) adsorption of reactants (CO and H_2); (2) activation of CO (or chain initiation); (3) chain propagation; and (4) chain termination (product formation). CO can be activated by the CO insertion chain growth and carbide mechanisms (Figures 2.1 and 2.2.) The difference between these two CO activation mechanisms is in the initial compound that starts the elongation, CH_2 for the carbide mechanism and CH_3-S for the CO insertion chain growth mechanism [118]. The model developed by Todic et al. is based on the CO insertion chain growth mechanism.

As there are multiple elementary reaction mechanisms during the FTS, their reaction rates are complex because each step involves equilibrium constants. Steps 1 and 2 are the uptake of CO and H_2 on the support to steady state. Step 3 is the activation of the absorbed CO by hydrogenation to CHO-S and the insertion of CO-S to the growing chain (C_nH_{2n+1}-S). This step depends only on the temperature considering that the chain growth does not influence the kinetic reaction constants. Then the chain increases due to the fast hydrogenation of the absorbed CO to CH_2, forming $C_nH_{2n+1}CH_2$-S (Steps 4 and 5). The formation and rapid dissociation of H_2O on the catalyst's surface can occur during a pseudo-equilibrium state (Step 6). In step 7 the alkyl chains are hydrogenated into paraffins. As for the formation of 1-olefin, it occurs during the dehydrogenation (β-hydrogen elimination) of C_nH_{2n+1}-S followed by its desorption (Step 8). The desorption step depends on the temperature and the number of C-atoms (CH_2-group) in the alkene molecule [118]. Steps 1, 5 and 6 are considered by Todic et al. to be the rate-determining steps as the other steps occur quickly enough to be in pseudo equilibrium [119]. All steps and equilibrium constants are described in Table 4.4.

Table 4.4 Elementary steps of the CO insertion chain growth mechanism used in the kinetic model

No.	Elementary step	Rate and equilibrium constants
(1)	CO + S $\rightleftharpoons$ CO-S	K_1
(2)	H_2 + 2S $\rightleftharpoons$ 2H-S	K_2
(3^{RDS})	CO-S + H-S $\rightarrow$ CHO-S + S CO-S + CH_3-S $\rightarrow$ CH_3CO-S + S CO-S + C_nH_{2n+1}-S $\rightarrow$ C_nH_{2n+1}CO-S + S n = 2,3,...	K_3
(4)	CHO-S + H-S $\rightleftharpoons$ CH_2O-S + S CH_3CO-S + H-S $\rightleftharpoons$ CH_3CHO-S + S C_nH_{2n+1}CO-S + H-S $\rightleftharpoons$ C_nH_{2n+1}CHO-S + S n = 2,3,...	K_4
(5)	CH_2O-S + 2H-S $\rightleftharpoons$ CH_3-S + OH-S + S CH_3CHO-S + 2H-S $\rightleftharpoons$ CH_3CH_2-S + OH-S + S C_nH_{2n+1}CHO-S + 2H-S $\rightleftharpoons$ $C_nH_{2n+1}CH_2$-S + OH-S + S n = 2,3,...	K_5
(6)	OH-S + H-S $\rightleftharpoons$ H_2O + 2S	K_6
(7^{RDS})	CH_3-S + H-S $\rightarrow$ CH_4 + 2S C_nH_{2n+1}-S + H-S $\rightarrow$ C_nH_{2n+2} + 2S n = 2,3,...	K_{7M} K_7
(8^{RDS})	C_2H_5-S $\rightarrow$ C_2H_4 + H-S C_nH_{2n+1}-S $\rightarrow$ C_nH_{2n} + H-S n = 3,4,...	K_{8E} K_8

We assume that the reaction kinetics are unaffected by the presence of Cu atoms, instead we consider Cu as the promoter to ensure the metallic state of Co. As a result, the findings we'll outline in the next paragraph should be regarded as apparent kinetic parameters for the reactor system under consideration in this study. One of the assumptions made for the model is that due to the linear increase in the activation energy of 1-olefin desorption, the rate constant for 1-olefin desorption depends exponentially on the carbon number [118, 120]. Todic et al. demonstrated with Equation 4.3, the linear dependence of the activation energy of desorption resulting from the linear dependence of the heat of chemisorption of 1-olefin with carbon number:

$$E_{d,o}^{n} = E_{d,o}^{0} + \Delta E \times n \tag{4.3}$$

where $E_{d,o}^{n}$ is the activation energy of the desorption step of the 1-olefin molecule with n atoms of C, $E_{d,o}^{0}$ represents the desorption energy of the 1-olefin molecule that is independent of the number of C atoms, ΔE is the contribution of Van der Waals (VdW) interactions of the chain with the surface for every C-atom (or CH_2-group) [119]. Equation 4.3 can be coupled to the Arrhenius equation (Equation 4.4) to establish the rate of desorption of 1-olefin according to the temperature and the length of the chain ($k_{d,n}$):

$$\begin{aligned} k_{d,n} &= A_d e^{-E_{d,o}^{n}/RT} \\ k_{d,n} &= A_d e^{-(E_{d,o}^{0}+\Delta E\times n)/RT} \\ k_{d,n} &= A_d e^{-E_{d,o}^{0}/RT} e^{-\Delta E\times n/RT} \end{aligned} \tag{4.4}$$

Constant c represents the weak VdW operation. It groups the constant terms (Equation 4.5) to simplify Equation 4.6 :

$$c = -\frac{\Delta E}{RT} \tag{4.5}$$

$$e^{-\Delta E\times n/RT} = e^{c\times n} \tag{4.6}$$

The final equation of the olefin desorption rate constant (Equation 4.7) is:

$$k_{d,n} = k_{d,0} e^{c\times n} \tag{4.7}$$

where $k_{d,n}$ is the desorption rate of 1-olefin with a carbon-number $n \geq 3$. The equilibrium constants for the different steps are expressed in Equation 4.8:

$$K_i(T) = A_i e^{(-\frac{\Delta H_i}{RT})} \tag{4.8}$$

The equations to calculate the chain growth probability are dependent on the number of carbon and are expressed in Equations 4.9, 4.10 and 4.11:

$$\alpha_1 = \frac{k_3 K_1 P_{CO}}{k_3 K_1 P_{CO} + k_{7M}\sqrt{K_2 P_{H_2}}} \tag{4.9}$$

$$\alpha_2 = \frac{k_3 K_1 P_{CO}[S]}{k_3 K_1 P_{CO}[S] + k_{7M}\sqrt{K_2 P_{H_2}}[S] + k_{8E} e^{c\cdot 2}} \tag{4.10}$$

$$\alpha_n = \frac{k_3 K_1 P_{CO}[S]}{k_3 K_1 P_{CO}[S] + k_{7M}\sqrt{K_2 P_{H_2}}[S] + k_8 e^{c\cdot n}} \quad n \geq 3 \tag{4.11}$$

For [S], the vacant active site on the catalyst is calculated by Equation 4.12:

$$[S] = 1/\left\{1 + K_1 P_{CO} + \sqrt{K_2 P_{H_2}} + \left(\frac{1}{K_2^2 K_4 K_5 K_6}\frac{P_{H_2O}}{P_{H_2}^2} + \sqrt{K_2 P_{H_2}}\right) \times \left(\alpha_1 + \alpha_1\alpha_2 + \alpha_1\alpha_2 \sum_{i=3}^{n}\prod_{j=3}^{i}\alpha_j\right)\right\} \tag{4.12}$$

Equation 4.12 is an implicit nonlinear function of a single variable [S] whose value is between 0 and 1. Since the Equations 4.9, 4.10, 4.11 and 4.12 are recursive, their resolution requires an iterative calculation. Rates of formation of n-paraffins and 1-olefin with carbon-number n are calculated with Equations 4.13, 4.14, 4.15 and 4.16:

$$R_{CH_4} = k_{7M} K_2^{0,5} P_{H_2}^{0,5} \alpha_1 [S]^2 \tag{4.13}$$

$$R_{C_n H_{2n+2}} = k_7 K_2^{0,5} \alpha_1 \alpha_2 \sum_{i=2}^{n} \alpha_j [S]^2 \quad n \geq 2 \tag{4.14}$$

$$R_{C_2 H_4} = k_{8E} e^{c\cdot 2} \alpha_1 \alpha_2 [S] \tag{4.15}$$

$$R_{C_n H_{2n}} = k_8 e^{c\cdot n} \alpha_1 \alpha_2 \sum_{i=3}^{n} \alpha_j [S] \quad n \geq 3 \tag{4.16}$$

The model developed from the experimental data and parameters from Todic et al. (Table F.1) is shown in Figure 4.12 [118]. This step confirms the performance and accuracy of the model to fit the experimental values.

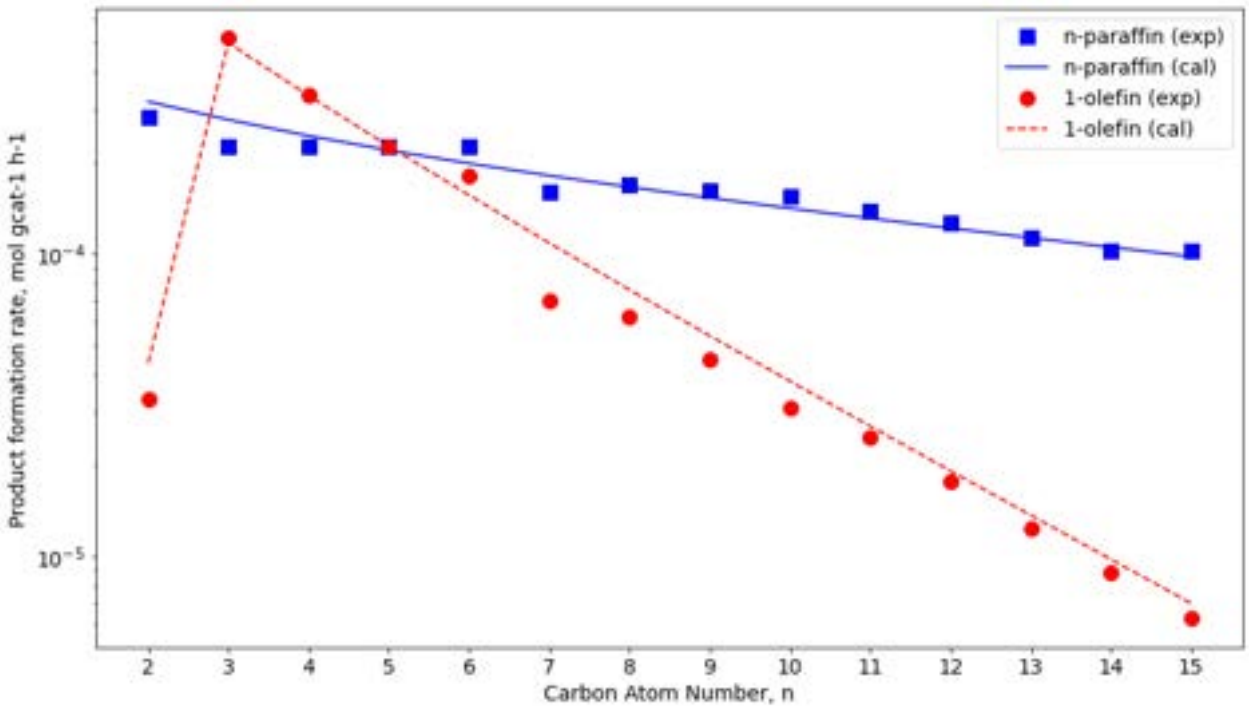

Figure 4.12 Experimental and calculated product distribution from experimental and model parameter values of Todic et al. for n-paraffin and 1-olefin formation rates

We optimized our model following the Nelder-Mead minimization method. This method consists in randomly modifying the variables for a given reaction kinetics parameter to reduce the average absolute percentage error between the experimental data and the model results, thus allowing to optimize the values for each parameter. The efficiency of this method was confirmed by applying it to the developed model (Figure 4.12), allowing to identify the optimized values of each parameter. The optimized version of the model is presented in Figure F.12. The model was then applied to the experimentally tested Co15, Co15-Cu0.05, Co15-Cu0.15 and Co15-Cu0.25 catalysts. A change in the apparent kinetic constants was observed (Tables F.2, F.3. F.4 and F.5).

Increasing the concentration of Cu to 0.05 g g^{-1} reduced the conversion of CO towards jet fuel range hydrocarbons. We are not reporting the results in the simulation as the concentration of products is negligible.

Figure 4.13 represents the model optimized according to the experimental data for each catalyst tested. The model allows to predict the rate of paraffin formation (solid line) for each hydrocarbon.

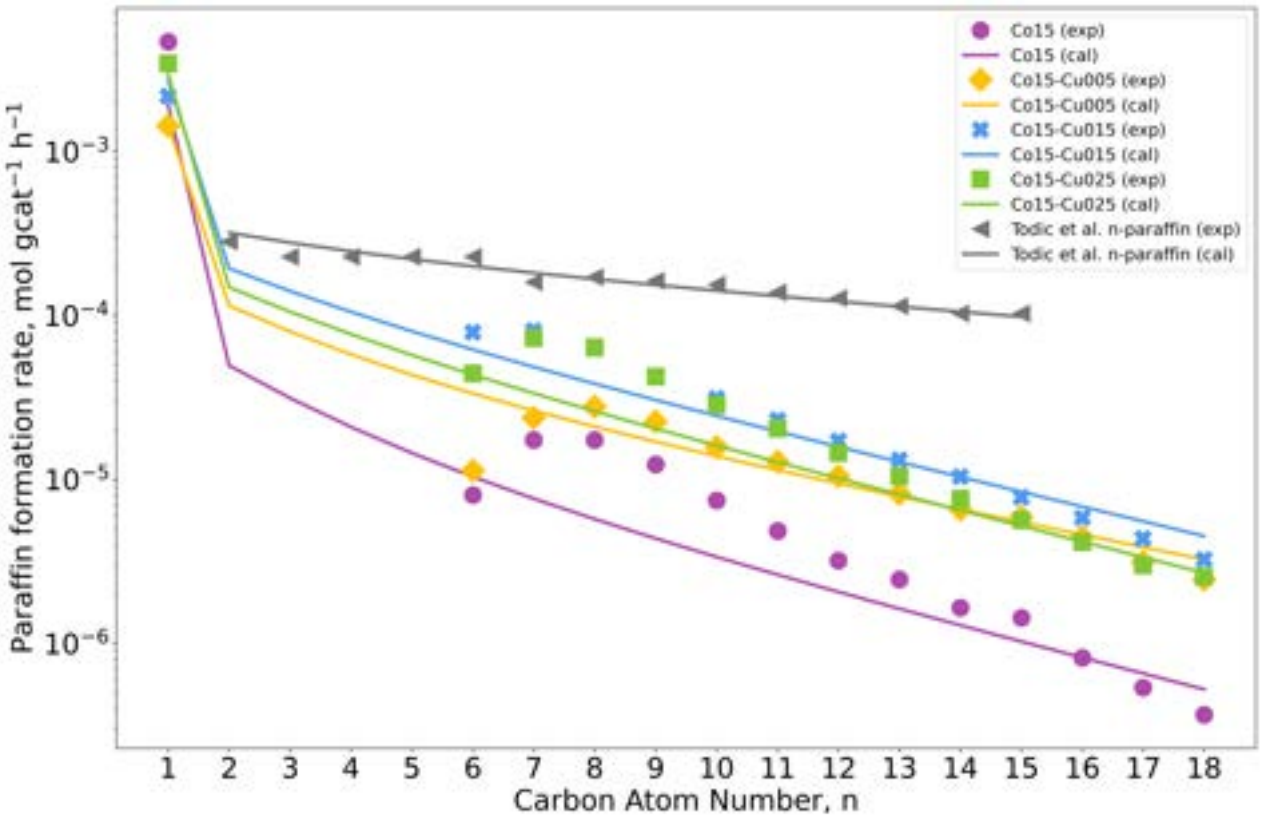

Figure 4.13 Experimental and calculated product distribution for all catalysts tested for n-paraffin formation rates. Data and model results from Todic et al. paper are included for comparison

The distribution of non-ASF products can be explained by the fact that the addition of VdW increases the chemisorption energy of 1-olefin interactions and that the ratio of paraffin formation is not linear compared to what is presented in the work of Todic et al. which explains the curvature of the model and the impossibility to include all experimental values [118]. The production of C_{5+} paraffin is, in fact, similar to the work of Haghtalab et al. and Bertoncini et al. [121, 122]

After optimization, each catalyst's reaction rate and equilibrium constants were extracted to evaluate their value (Figure 4.14). Each value has been normalized to Co15 catalyst. The adsorption equilibrium step for CO (K_1) is lower than the normal established because Cu obstructs the active sites on Co, explaining the decrease of the CO fixation rate on the catalyst surface. The reduction of K_1 is consistent with the amount of Cu on the catalyst. More Cu blocks more active sites, further decreasing the reaction constant. The K_2 constant, associated with the fixation of free H on the catalyst, is the highest for Co15-Cu0.25. Cu

causes H_2 spillover, explaining why the amount of H_2 that binds to the catalyst increases with the Cu mass ratio. Co15-Cu0.05 seems to have a minimal negative effect on H_2 overflow. However, it is likely to be considered that the variation of this parameter is 0, as does the Co15 catalyst considering the small amount of Cu (0.0005 g g^{-1}), without considering that Co15-Cu0.05 has a 60% lower CO conversion than Co15. Considering the amount of Cu on the Co-based catalyst, it would have been possible to expect a similar conversion to Co15. Therefore, the CO conversion for Co15-Cu0.05 may be aberrant, explaining the divergence of some reaction kinetics parameters. The value of the constant K_3 is higher for the Co15-Cu0.15 catalyst compared to the other catalysts. According to the results obtained (Figure 4.7), Cu in an adequate amount (0.0015 g g^{-1}) presents a higher selectivity and conversion than the other catalysts because it favours the reduction of the catalyst and H_2 spillover. Further tests showed that the Co15-Cu0.15 catalyst produced more moles of paraffin per minute than Co15-Cu0.05 and Co15-Cu0.25 (Figure 4.13), which explains the higher value of the reaction rate parameter. For K_7, associated with free paraffin formation, the Co15-Cu0.15 catalyst has the highest value since the number of moles per minute of paraffin produced by this catalyst is higher than the others (Figure 4.13). Overall, the higher the paraffin formation rate of the catalysts, the more K_7 increases to fit the curve. However, despite a formation rate for C_{5+} paraffin of 0.000580 mol g_{cat}^{-1} s^{-1} for Co15-Cu0.25, the parameter K_7 is lower than Co15-Cu0.05 whose formation rate for C_{5+} paraffin is 0.000459 mol g_{cat}^{-1} s^{-1}. It is currently difficult to explain precisely the reason for this parameter deviation compared to the two other catalysts. The parameter K_{7M}, associated with the formation of free methane, decreased with the addition of Cu (Table 4.4). Optimizing the models according to the rate of formation of the products behaved as advised by a decrease of the constant. For constant K_8, following optimization of the model for each catalyst, it would appear that Cu decreases C_{3+} olefin formation. However, we cannot validate such behaviour of this constant because the production of olefins was not measured experimentally since the paraffin was the product of interest. It appears that Co15-Cu0.05 is the only catalyst that influences the parameters K_5, K_{8E} and c. Given that the Co15-Cu0.05 catalyst is impregnated with 0.0005 g g^{-1} Cu, it is surprising that Cu reduces the hydrogenation of Co (K_5) by ∼30% while promoting the formation of 1-olefin (K_{8E}) by ∼60%. Knowing that Cu causes H_2 spillover to Co, one would expect Cu impregnation to positively affect the K_5 parameter, if any at all, given the small amount.

Conversely, no catalyst has shown such high selectivity for 1-olefin formation as the Co15-Cu0.05 catalyst. However, olefins were not analyzed for the Cox-Cuy catalysts. As for the effect of the VdW associated with the constant, it would be possible that the variation of this parameter is 0 considering the small quantity of Cu. However, it is impossible to validate it. Add that when the concentration of Cu is limited to 0.0005 g g^{-1}, K_4 and K_6 constants are unaffected, suggesting that the high dispersion of Cu does not influence the apparent kinetics of the reaction.

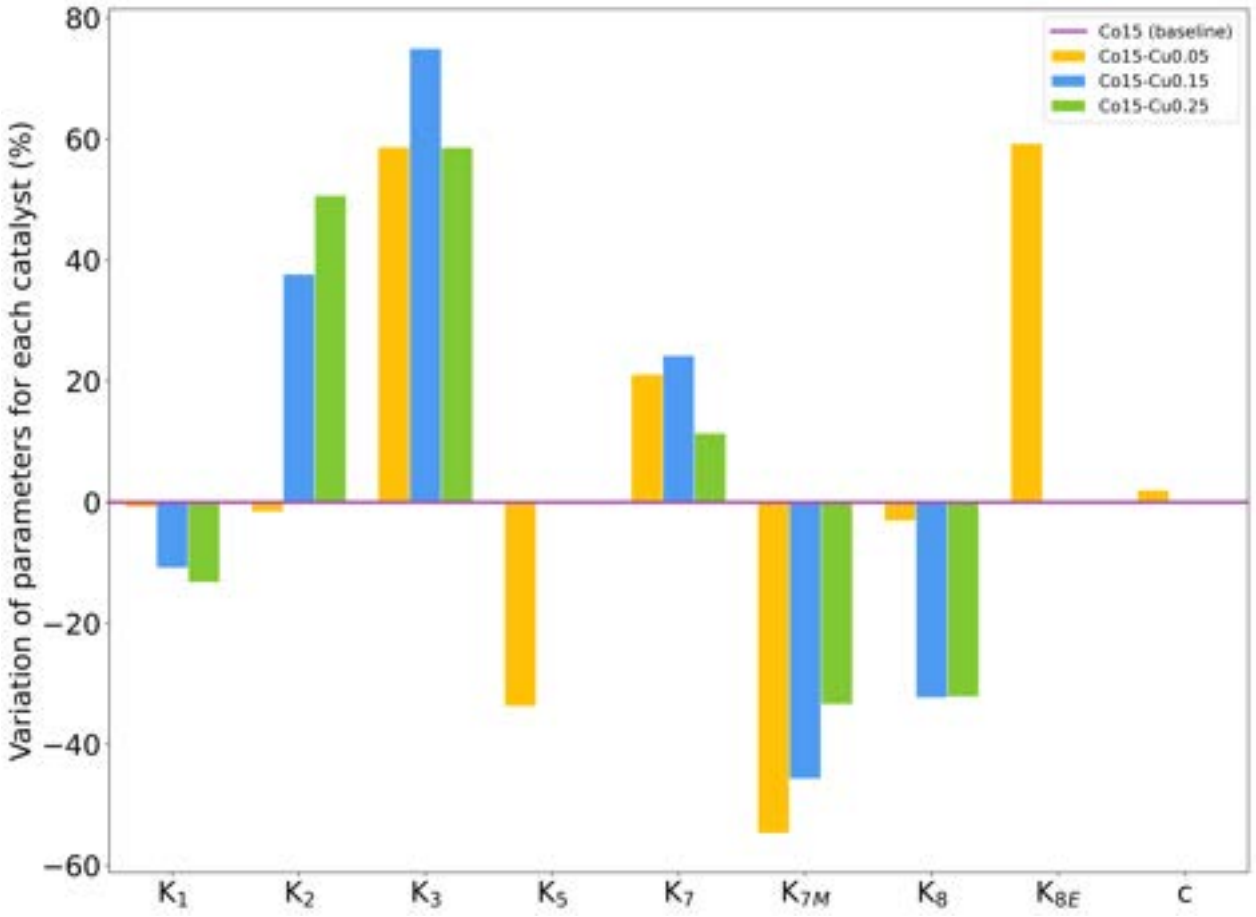

Figure 4.14 Variation of reaction kinetic parameters compared to Co15 for each of the catalysts

The information acquired by these results would allow us in future work to evaluate the optimal concentration of Cu necessary to maximize jet fuel production. Although this study predicts the products from different catalyst compositions, additional in situ measurements will be required to understand the interaction of hydrocarbons in the presence of Cu and Co atoms.

CHAPTER 5 CONCLUSION

5.1 Summary of Works

This research project identified the effects of sonochemically synthesizing Co-based catalyst doped with Cu for the FTS to substitute the use of noble metals (Ru, Re, Pt) as promoters. The characterization of the catalysts shows that the ultrasonic impregnation produces uniformly dispersed NPs of about ∼6 nm in diameter. During the FTS, a Cu threshold >0.0025 g g^{-1} blocks the sites of Co NPs. Cu lowers the reduction temperature of Co/Al_2O_3 as a function of metal loading. Cu increases CO conversion and decreases catalyst deactivation over time. Cu doped on a Co-based catalyst increased the selectivity of Co15-Cu0.15 catalyst for C_{5+} hydrocarbons by ∼6 times compared to a Cu-free catalyst. The increase in selectivity is due to the H_2 spillover, increasing the accessibility of free H, favouring the extension of the C_{5+} chains while ensuring the reducibility of Co. The developed model allows for optimizing the reaction kinetics parameters to fit the experimental values. It allowed to evaluate the impact of the Cu concentration on each step of the CO conversion mechanism and to predict the behaviour of the catalysts according to the Cu concentration.

5.2 Limitations

The proposed solution is limited due to the lack of data for the Co15-Cu0.05 and Co15-Cu0.15 catalysts. Since the performance of these catalysts was belatedly discovered, it was impossible to perform all the tests, such as XRD analysis, dispersion and NPs size, d-spacing and TPR. It is impossible to confirm that the results obtained with the other catalysts are similar to Co15-Cu0.05 and Co15-Cu0.15 catalysts. The residence time of 1 s is also a limiting factor since it limits the conversion of CO by reducing its contact time with the catalyst. This impacts the results, and it is impossible to identify the optimal performance of the catalysts presented. The lack of calibration of C_2 to C_4 hydrocarbons, alcohols and olefins is a limitation of the proposed solution since it is impossible to accurately complete the mass balance of the products formed by the catalysts. In addition, C_4 hydrocarbons at the experimental conditions (230°C, 20 bar) are liquid. The Bruker Scion Instruments 456 GC cannot analyze this specie's concentration. However, when the reactor is depressurized, the C_4 vaporizes at room temperature and atmospheric pressure, preventing its analysis by the Agilent 7890B GC. The following section details the improvements that will be made to the tests performed.

5.3 Future Research

The length and diameter of the Fischer-Tropsch reactor should be increased. Increasing the reactor size would allow more catalysts to be inserted, which would increase the residence time. Increasing the residence time would increase the contact time with the CO, promoting higher conversion.

It would be essential to modify the Bruker Scion Instruments 456 GC analysis method and improve the FT reactor by adding a connection to collect the C_4 produced by the tested catalysts during depressurization for analysis.

It would be interesting to test the amount of C_2 - C_4 hydrocarbons, alcohols and olefins to represent better the products the catalysts formed during the synthesis.

Future tests should be performed on Co15-Cu0.05 and Co15-Cu0.15 catalysts to evaluate the dispersion of Cu and its effect on the reduction temperature of these catalysts.

The results of CO conversion from Co15-Cu0.05 catalyst seem erroneous. The low amount of Cu impregnated (0.0005 g g^{-1}) suggested that CO conversion would have been similar to that of Co15, whereas it is 60% lower. In addition, the results obtained with the model demonstrate a different behaviour of Co15-Cu0.05 compared to other catalysts. This catalyst seems to limit hydrocarbon chain elongation and favour 1-olefin production. Therefore, it would be interesting to test this catalyst again to ensure the result's accuracy.

REFERENCES

[1] H. Ritchie, M. Roser, and P. Rosado, "Energy," *Our World in Data*, 2022, https://ourworldindata.org/energy.

[2] A. Olabi and M. A. Abdelkareem, "Renewable energy and climate change," *Renewable and Sustainable Energy Reviews*, vol. 158, p. 112111, 2022.

[3] Government of Canada. (2022) Greenhouse gas emissions. [Online]. Available: https://www.canada.ca/en/environment-climate-change/services/environmental-indicators/greenhouse-gas-emissions.html

[4] K. Dahal *et al.*, "Techno-economic review of alternative fuels and propulsion systems for the aviation sector," *Renewable and Sustainable Energy Reviews*, vol. 151, p. 111564, 2021.

[5] J. H. Park *et al.*, "Review of recent technologies for transforming carbon dioxide to carbon materials," *Chemical Engineering Journal*, vol. 427, p. 130980, 2022.

[6] M. D. Garba *et al.*, "Co2 towards fuels: A review of catalytic conversion of carbon dioxide to hydrocarbons," *Journal of Environmental Chemical Engineering*, vol. 9, no. 2, p. 104756, 2021.

[7] T. A. Atsbha *et al.*, "A review on the catalytic conversion of co2 using h2 for synthesis of co, methanol, and hydrocarbons," *Journal of CO2 utilization*, vol. 44, p. 101413, 2021.

[8] L.-P. Merkouri *et al.*, "Versatile ni-ru catalysts for gas phase co2 conversion: Bringing closer dry reforming, reverse water gas shift and methanation to enable end-products flexibility," *Fuel*, vol. 315, p. 123097, 2022.

[9] Q. Zhang *et al.*, "Co2 conversion via reverse water gas shift reaction using fully selective mo–p multicomponent catalysts," *Industrial & Engineering Chemistry Research*, vol. 61, no. 34, pp. 12 857–12 865, 2022.

[10] M. Zhu, Q. Ge, and X. Zhu, "Catalytic reduction of co 2 to co via reverse water gas shift reaction: Recent advances in the design of active and selective supported metal catalysts," *Transactions of Tianjin University*, vol. 26, pp. 172–187, 2020.

[11] A. C. Ghogia *et al.*, "Cobalt catalysts on carbon-based materials for fischer-tropsch synthesis: a review," *Applied Catalysis A: General*, vol. 609, p. 117906, 2021.

[12] H. Mahmoudi *et al.*, "A review of fischer tropsch synthesis process, mechanism, surface chemistry and catalyst formulation," *Biofuels Engineering*, vol. 2, no. 1, pp. 11–31, 2017.

[13] L. Gavrilović *et al.*, "Fischer-tropsch synthesis over an alumina-supported cobalt catalyst in a fixed bed reactor–effect of process parameters," *Catalysis Today*, vol. 369, pp. 150–157, 2021.

[14] C. I. Méndez and J. Ancheyta, "Kinetic models for fischer-tropsch synthesis for the production of clean fuels," *Catalysis Today*, vol. 353, pp. 3–16, 2020.

[15] Daily Metal Prices. (2022) Metal spot price charts. [Online]. Available: https://www.dailymetalprice.com/metalpricecharts.php?c=u&u=lb&d=240

[16] Metal Properties. (2019) Rhénium – propriétés – prix – applications – production. [Online]. Available: https://material-properties.org/fr/rhenium-proprietes-prix-applications-production/

[17] Teter, Jacob and Kim, Hyeji. (2022) Aviation. [Online]. Available: https://www.iea.org/reports/aviation

[18] Government of Quebec. (2022) Green hydrogen. [Online]. Available: https://www.quebec.ca/en/agriculture-environment-and-natural-resources/energy/energy-production-supply-distribution/green-hydrogen

[19] A. Dubey and A. Arora, "Advancements in carbon capture technologies: A review," *Journal of Cleaner Production*, p. 133932, 2022.

[20] J. Sun *et al.*, "Beyond cars: Fischer-tropsch synthesis for non-automotive applications," *ChemCatChem*, vol. 11, no. 5, pp. 1412–1424, 2019.

[21] V. Dieterich *et al.*, "Power-to-liquid via synthesis of methanol, dme or fischer–tropsch-fuels: a review," *Energy & Environmental Science*, vol. 13, no. 10, pp. 3207–3252, 2020.

[22] W. Yuan *et al.*, "Modeling and optimization of supercritical phase fischer-tropsch synthesis," in *Computer Aided Chemical Engineering*. Elsevier, 2011, vol. 29, pp. 1929–1933.

[23] Gouvernement du Canada. (2023) La carboneutralité d'ici 2050. [Online]. Available: https://www.canada.ca/fr/services/environnement/meteo/changementsclimatiques/plan-climatique/carboneutralite-2050.html

[24] Z. Gholami, Z. Tišler, and V. Rubáš, "Recent advances in fischer-tropsch synthesis using cobalt-based catalysts: A review on supports, promoters, and reactors," *Catalysis Reviews*, vol. 63, no. 3, pp. 512–595, 2021.

[25] R. Van Santen *et al.*, "Mechanism and microkinetics of the fischer–tropsch reaction," *Physical Chemistry Chemical Physics*, vol. 15, no. 40, pp. 17 038–17 063, 2013.

[26] G. P. Van Der Laan and A. Beenackers, "Kinetics and selectivity of the fischer–tropsch synthesis: a literature review," *Catalysis Reviews*, vol. 41, no. 3-4, pp. 255–318, 1999.

[27] X. Fang *et al.*, "Particle-size-dependent methane selectivity evolution in cobalt-based fischer–tropsch synthesis," *ACS Catalysis*, vol. 10, no. 4, pp. 2799–2816, 2020.

[28] J. Van Belleghem *et al.*, "Microkinetic model validation for fischer-tropsch synthesis at methanation conditions based on steady state isotopic transient kinetic analysis," *Journal of Industrial and Engineering Chemistry*, vol. 105, pp. 191–209, 2022.

[29] C. L. Tucker and E. van Steen, "Activity and selectivity of a cobalt-based fischer-tropsch catalyst operating at high conversion for once-through biomass-to-liquid operation," *Catalysis Today*, vol. 342, pp. 115–123, 2020.

[30] C. L. Tucker *et al.*, "Manganese promotion of a cobalt fischer-tropsch catalyst to improve operation at high conversion," *Journal of Catalysis*, vol. 411, pp. 97–108, 2022.

[31] W. Ma, W. D. Shafer, and M. Martinelli, "Fischer–tropsch reactions and product distribution suits for downstream," in *Chemicals and Fuels from Biomass via Fischer–Tropsch Synthesis*, 2022, pp. 188–213.

[32] A. V. Karre and D. B. Dadyburjor, "Review of iron-based catalysts with and without zeolite supports used in fischer-tropsch processes," *Chemical Engineering Communications*, vol. 209, no. 7, pp. 967–987, 2022.

[33] P. P. Paalanen, S. H. Van Vreeswijk, and B. M. Weckhuysen, "Combined in situ x-ray powder diffractometry/raman spectroscopy of iron carbide and carbon species evolution in fe (- na–s)/α-al2o3 catalysts during fischer–tropsch synthesis," *ACS Catalysis*, vol. 10, no. 17, pp. 9837–9855, 2020.

[34] Q. Zhang, W. Deng, and Y. Wang, "Recent advances in understanding the key catalyst factors for fischer-tropsch synthesis," *Journal of Energy Chemistry*, vol. 22, no. 1, pp. 27–38, 2013.

[35] J. S. Kaizer, A. K. Heller, and W. L. Oberkampf, "Scientific computer simulation review," *Reliability Engineering & System Safety*, vol. 138, pp. 210–218, 2015.

[36] F. Sauerhöfer-Rodrigo *et al.*, "Modelling of fixed bed and slurry bubble column reactors for fischer–tropsch synthesis," *Reviews in Chemical Engineering*, no. 0, 2023.

[37] Z. Teimouri *et al.*, "Application of computational fluid dynamics for modeling of fischer-tropsch synthesis as a sustainable energy resource in different reactor configurations: A review," *Renewable and Sustainable Energy Reviews*, vol. 160, p. 112287, 2022.

[38] H. Williams *et al.*, "Fischer–tropsch synthesis: Computational sensitivity modeling for series of cobalt catalysts," *Catalysts*, vol. 9, no. 10, p. 857, 2019.

[39] D. Martinez del Monte *et al.*, "Potential pathways for syngas transformation towards kerosene range hydrocarbons in a dual fischer-tropsch-zeolite bed," *International Journal of Energy Research*, vol. 46, no. 4, pp. 5280–5287, 2022.

[40] A. Barenbaum and D. Klimov, "Theoretical model anderson-schulz-flory within the framework of studying the mechanism of polycondensation synthesis," *Inorganic Chemistry Communications*, vol. 112, p. 107664, 2020.

[41] H. M. Torres Galvis and K. P. de Jong, "Catalysts for production of lower olefins from synthesis gas: a review," *ACS catalysis*, vol. 3, no. 9, pp. 2130–2149, 2013.

[42] J. Cheng *et al.*, "A dft study of the chain growth probability in fischer–tropsch synthesis," *Journal of Catalysis*, vol. 257, no. 1, pp. 221–228, 2008.

[43] Q. Cheng *et al.*, "Manipulating metal-support interactions of metal catalysts for fischer-tropsch synthesis," *Chinese Journal of Chemical Engineering*, vol. 35, pp. 220–230, 2021.

[44] K. D. Kruit *et al.*, "Selectivity of the fischer–tropsch process: deviations from single alpha product distribution explained by gradients in process conditions," *Catalysis Science & Technology*, vol. 3, no. 9, pp. 2210–2213, 2013.

[45] J. G. Speight, "Chapter 8 - hydrocarbons from synthesis gas," in *Handbook of Industrial Hydrocarbon Processes (Second Edition)*, second edition ed., J. G. Speight,

Ed. Boston: Gulf Professional Publishing, 2020, pp. 343–386. [Online]. Available: https://www.sciencedirect.com/science/article/pii/B9780128099230000084

[46] M. Martinelli *et al.*, "An overview of fischer-tropsch synthesis: Xtl processes, catalysts and reactors," *Applied Catalysis A: General*, vol. 608, p. 117740, 2020.

[47] H. Jahangiri *et al.*, "Chapter 14 - production of biofuels via fischer-tropsch synthesis: Biomass-to-liquids," in *Handbook of Biofuels Production (Third Edition)*, third edition ed., ser. Woodhead Publishing Series in Energy, R. Luque *et al.*, Eds. Woodhead Publishing, 2023, pp. 449–509. [Online]. Available: https://www.sciencedirect.com/science/article/pii/B9780323911931000135

[48] C. H. Bartholomew, "Mechanisms of catalyst deactivation," *Applied Catalysis A: General*, vol. 212, no. 1, pp. 17–60, 2001, catalyst Deactivation. [Online]. Available: https://www.sciencedirect.com/science/article/pii/S0926860X00008437

[49] V. R. R. Pendyala *et al.*, "Fischer–tropsch synthesis: effect of activation gas after varying cu promoter loading over k-promoted fe-based catalyst," *Catalysis letters*, vol. 144, pp. 1624–1635, 2014.

[50] M. Claeys *et al.*, "Impact of process conditions on the sintering behavior of an alumina-supported cobalt fischer–tropsch catalyst studied with an in situ magnetometer," *ACS Catalysis*, vol. 5, no. 2, pp. 841–852, 2015.

[51] D. Moodley *et al.*, "Sintering of cobalt during fts: Insights from industrial and model systems," *Catalysis Today*, vol. 342, pp. 59–70, 2020.

[52] J. Zhou *et al.*, "Regeneration of catalysts deactivated by coke deposition: A review," *Chinese Journal of Catalysis*, vol. 41, no. 7, pp. 1048–1061, 2020.

[53] S. Li *et al.*, "Tuning strong metal-support interactions to boost activity and stability of aluminium nitride supported nickel catalysts for dry reforming of methane," *Fuel*, vol. 343, p. 127918, 2023.

[54] N. Ostrovskii, "Coking of catalysts: Mechanisms, models, and influence," *Kinetics and Catalysis*, vol. 63, no. 1, pp. 52–66, 2022.

[55] A. C. Ghogia *et al.*, "Hydrogen spillover in the fischer-tropsch synthesis on carbon-supported cobalt catalysts," *ChemCatChem*, vol. 12, no. 4, pp. 1117–1128, 2020.

[56] D. Nabaho *et al.*, "Hydrogen spillover in the fischer–tropsch synthesis: An analysis of platinum as a promoter for cobalt–alumina catalysts," *Catalysis Today*, vol. 261, pp. 17–27, 2016.

[57] C. Iris and B. M. Weckhuysen, "The active phase in cobalt-based fischer-tropsch synthesis," *Chem Catalysis*, vol. 1, no. 2, pp. 339–363, 2021.

[58] EnvironmentalChemistry.com. (2023) Element ruthenium - ru. [Online]. Available: https://environmentalchemistry.com/yogi/periodic/Ru.html

[59] D. B. Bukur *et al.*, "Binder/support effects on the activity and selectivity of iron catalysts in the fischer-tropsch synthesis," *Industrial & engineering chemistry research*, vol. 29, no. 8, pp. 1588–1599, 1990.

[60] J. Regalbuto, *Catalyst Preparation: Science and Engineering*. CRC Press, 2016. [Online]. Available: https://books.google.ca/books?id=j8ZQ5uAJyrcC

[61] J. Horáček, "Fischer–tropsch synthesis, the effect of promoters, catalyst support, and reaction conditions selection," *Monatshefte für Chemie-Chemical Monthly*, vol. 151, pp. 649–675, 2020.

[62] W. Chou *et al.*, "Effects of al, si, ti, zr promoters on catalytic performance of iron-based fischer–tropsch synthesis catalysts," *Catalysis Letters*, vol. 150, pp. 1993–2002, 2020.

[63] H. Wang *et al.*, "Effect of ca promoter on the structure and catalytic behavior of fek/al2o3 catalyst in fischer-tropsch synthesis," *ChemCatChem*, vol. 11, no. 14, pp. 3220–3226, 2019.

[64] F. Morales, B. M. Weckhuysen *et al.*, "Promotion effects in co-based fischer–tropsch catalysis," *Catalysis*, vol. 19, pp. 1–40, 2006.

[65] V. Vosoughi *et al.*, "Performances of promoted cobalt catalysts supported on mesoporous alumina for fischer-tropsch synthesis," *Applied Catalysis A: General*, vol. 547, pp. 155–163, 2017.

[66] D. U. Mangaloğlu *et al.*, "Effect of the promoter presence in catalysts on the compositions of fischer–tropsch synthesis products," *Journal of Industrial and Engineering Chemistry*, vol. 66, pp. 298–310, 2018.

[67] A. Wang *et al.*, "Effect of na, cu and ru on metal-organic framework-derived porous carbon supported iron catalyst for fischer-tropsch synthesis," *Molecular Catalysis*, vol. 509, p. 111601, 2021.

[68] W. Gong *et al.*, "Effect of copper on highly effective fe-mn based catalysts during production of light olefins via fischer-tropsch process with low co2 emission," *Applied Catalysis B: Environmental*, vol. 278, p. 119302, 2020.

[69] J. H. Bang and K. S. Suslick, "Applications of ultrasound to the synthesis of nanostructured materials," *Advanced materials*, vol. 22, no. 10, pp. 1039–1059, 2010.

[70] M. Ashokkumar, "The characterization of acoustic cavitation bubbles–an overview," *Ultrasonics sonochemistry*, vol. 18, no. 4, pp. 864–872, 2011.

[71] K. Yasui and K. Yasui, *Acoustic cavitation*. Springer, 2018.

[72] T. Q. Bui, H. T. M. Ngo, and H. T. Tran, "Surface-protective assistance of ultrasound in synthesis of superparamagnetic magnetite nanoparticles and in preparation of monocore magnetite-silica nanocomposites," *Journal of Science: Advanced Materials and Devices*, vol. 3, no. 3, pp. 323–330, 2018.

[73] J. C. Colmenares, "Sonication-induced pathways in the synthesis of light-active catalysts for photocatalytic oxidation of organic contaminants," *ChemSusChem*, vol. 7, no. 6, pp. 1512–1527, 2014.

[74] T. G. McKenzie *et al.*, "Ultrasound and sonochemistry for radical polymerization: sound synthesis," *Chemistry–A European Journal*, vol. 25, no. 21, pp. 5372–5388, 2019.

[75] R. J. Wood, J. Lee, and M. J. Bussemaker, "A parametric review of sonochemistry: Control and augmentation of sonochemical activity in aqueous solutions," *Ultrasonics sonochemistry*, vol. 38, pp. 351–370, 2017.

[76] H. Rostamabadi, S. R. Falsafi, and S. M. Jafari, "Transmission electron microscopy (tem) of nanoencapsulated food ingredients," in *Characterization of nanoencapsulated food ingredients*. Elsevier, 2020, pp. 53–82.

[77] A. Hungría, J. Calvino, and J. Hernández-Garrido, "Haadf-stem electron tomography in catalysis research," *Topics in Catalysis*, vol. 62, no. 12-16, pp. 808–821, 2019.

[78] M. Kannan, "Scanning electron microscopy: Principle, components and applications," *A Textbook on Fundamentals and Applications of Nanotechnology; Springer: Berlin/Heidelberg, Germany*, pp. 81–92, 2018.

[79] P. Qi *et al.*, "Techniques for the characterization of single atom catalysts," *RSC advances*, vol. 12, no. 2, pp. 1216–1227, 2022.

[80] S. Besselmann *et al.*, "Temperature-programmed reduction and oxidation experiments with v 2 o 5/tio 2 catalysts," *Physical chemistry chemical physics*, vol. 3, no. 21, pp. 4633–4638, 2001.

[81] D. Shindo *et al.*, "Energy dispersive x-ray spectroscopy," *Analytical electron microscopy for materials science*, pp. 81–102, 2002.

[82] M. Scimeca *et al.*, "Energy dispersive x-ray (edx) microanalysis: A powerful tool in biomedical research and diagnosis," *European journal of histochemistry: EJH*, vol. 62, no. 1, 2018.

[83] R. F. Egerton, *Electron energy-loss spectroscopy in the electron microscope*. Springer Science & Business Media, 2011.

[84] F. Hofer *et al.*, "Fundamentals of electron energy-loss spectroscopy," in *IOP conference series: Materials science and engineering*, vol. 109, no. 1. IOP Publishing, 2016, p. 012007.

[85] A. Ali, Y. W. Chiang, and R. M. Santos, "X-ray diffraction techniques for mineral characterization: A review for engineers of the fundamentals, applications, and research directions," *Minerals*, vol. 12, no. 2, p. 205, 2022.

[86] H. Khan *et al.*, "Experimental methods in chemical engineering: X-ray diffraction spectroscopy—xrd," *The Canadian journal of chemical engineering*, vol. 98, no. 6, pp. 1255–1266, 2020.

[87] Y. Xiang and N. Kruse, "Cobalt–copper based catalysts for higher terminal alcohols synthesis via fischer–tropsch reaction," *Journal of energy chemistry*, vol. 25, no. 6, pp. 895–906, 2016.

[88] T. Ishida *et al.*, "Synthesis of higher alcohols by fischer–tropsch synthesis over alkali metal-modified cobalt catalysts," *Applied Catalysis A: General*, vol. 458, pp. 145–154, 2013.

[89] H. Du *et al.*, "Activity and selectivity enhancement of silica supported cobalt catalyst for alcohols production from syngas via fischer-tropsch synthesis," *International Journal of Hydrogen Energy*, vol. 47, no. 7, pp. 4559–4567, 2022.

[90] G. H. Hong *et al.*, "Effect of catalytic reactor bed dilution on product distribution for fischer-tropsch synthesis over ru/co/al2o3 catalyst," *Catalysis Today*, vol. 303, pp. 136–142, 2018.

[91] Q. Lin *et al.*, "Assessing the formation of cobalt carbide and its catalytic performance under realistic reaction conditions and tuning product selectivity in a cobalt-based fts reaction," *Catalysis Science & Technology*, vol. 9, no. 12, pp. 3238–3258, 2019.

[92] R. W. Missen and W. R. Smith, "Yield, selectivity, and all that," *Chemical Engineering Education*, vol. 34, no. 4, pp. 320–324, 2000.

[93] R. D. Jones and C. H. Bartholomew, "Improved flow technique for measurement of hydrogen chemisorption on metal catalysts," *Applied Catalysis*, vol. 39, pp. 77–88, 1988.

[94] J. Evans *et al.*, "On the determination of copper surface area by reaction with nitrous oxide," *Applied Catalysis*, vol. 7, no. 1, pp. 75–83, 1983.

[95] J. Yang *et al.*, "Particle size effect for cobalt fischer–tropsch catalysts based on in situ co chemisorption," *Surface Science*, vol. 648, pp. 67–73, 2016.

[96] G. Jacobs *et al.*, "Group 11 (cu, ag, au) promotion of 15% co/al2o3 fischer–tropsch synthesis catalysts," *Applied Catalysis A: General*, vol. 361, no. 1-2, pp. 137–151, 2009.

[97] P. Louyot *et al.*, "Ultrasound-assisted impregnation for high temperature fischer-tropsch catalysts," *Ultrasonics Sonochemistry*, vol. 48, pp. 523–531, 2018.

[98] Z. Xiaofeng *et al.*, "Influence of ultrasound impregnation on the performance of co/zr/sio2 catalyst during fischer-tropsch synthesis," *Chinese Journal of Catalysis*, vol. 32, no. 6-8, pp. 1156–1165, 2011.

[99] C. Pirola *et al.*, "Ultrasound and microwave assisted synthesis of high loading fe-supported fischer–tropsch catalysts," *Ultrasonics sonochemistry*, vol. 17, no. 3, pp. 610–616, 2010.

[100] T. Kuang *et al.*, "Controlled synthesis of cobalt nanocrystals on the carbon spheres for enhancing fischer–tropsch synthesis performance," *Journal of energy chemistry*, vol. 33, pp. 67–73, 2019.

[101] G. M. Bremmer *et al.*, "In situ tem observation of the boudouard reaction: multi-layered graphene formation from co on cobalt nanoparticles at atmospheric pressure," *Faraday Discussions*, vol. 197, pp. 337–351, 2017.

[102] K. Wang *et al.*, "Synthesis and electrochemical performance of nickel–cobalt oxide/carbon nanocomposites for use in efficient oxygen evolution reaction," *Journal of Materials Science: Materials in Electronics*, vol. 30, pp. 4144–4151, 2019.

[103] Y. Liu *et al.*, "Concave co 3 o 4 octahedral mesocrystal: polymer-mediated synthesis and sensing properties," *CrystEngComm*, vol. 14, no. 19, pp. 6264–6270, 2012.

[104] X. Zhang *et al.*, "Process study on the formation of nanocrystalline α-alumina with novel morphology at 1000° c," *Journal of Materials Chemistry*, vol. 19, no. 13, pp. 1915–1922, 2009.

[105] F. Zhang *et al.*, "Facile growth of mesoporous co3o4 nanowire arrays on ni foam for high performance electrochemical capacitors," *Journal of Power Sources*, vol. 203, pp. 250–256, 2012.

[106] S.-M. Park *et al.*, "Hybrid cu x o–tio2 heterostructured composites for photocatalytic co2 reduction into methane using solar irradiation: Sunlight into fuel," *ACS omega*, vol. 1, no. 5, pp. 868–875, 2016.

[107] G. Jacobs, W. Ma, and B. H. Davis, "Influence of reduction promoters on stability of cobalt/γ-alumina fischer-tropsch synthesis catalysts," *Catalysts*, vol. 4, no. 1, pp. 49–76, 2014.

[108] G. Jacobs *et al.*, "Fischer–tropsch synthesis: Temperature programmed exafs/xanes investigation of the influence of support type, cobalt loading, and noble metal promoter addition to the reduction behavior of cobalt oxide particles," *Applied Catalysis A: General*, vol. 333, no. 2, pp. 177–191, 2007.

[109] S. Guo *et al.*, "A comprehensive insight into the role of barium in catalytic performance of co/al2o3 catalyst for fischer-tropsch synthesis," *Fuel*, vol. 256, p. 115911, 2019.

[110] R. Xu *et al.*, "Effects of ag promotion for co/al2o3 catalyst in fischer-tropsch synthesis," *Catalysis Today*, vol. 342, pp. 111–114, 2020.

[111] D. Peña *et al.*, "The effect of copper loading on iron carbide formation and surface species in iron-based fischer–tropsch synthesis catalysts," *ChemCatChem*, vol. 10, no. 6, pp. 1300–1312, 2018.

[112] C. Göbel *et al.*, "Structural evolution of bimetallic co-cu catalysts in co hydrogenation to higher alcohols at high pressure," *Journal of Catalysis*, vol. 383, pp. 33–41, 2020.

[113] Z. H. Chonco *et al.*, "Copper ferrites: A model for investigating the role of copper in the dynamic iron-based fischer–tropsch catalyst," *Journal of catalysis*, vol. 308, pp. 363–373, 2013.

[114] M. Rahmati *et al.*, "Chemical and thermal sintering of supported metals with emphasis on cobalt catalysts during fischer–tropsch synthesis," *Chemical reviews*, vol. 120, no. 10, pp. 4455–4533, 2020.

[115] P. Munnik, P. E. De Jongh, and K. P. De Jong, "Control and impact of the nanoscale distribution of supported cobalt particles used in fischer–tropsch catalysis," *Journal of the American Chemical Society*, vol. 136, no. 20, pp. 7333–7340, 2014.

[116] F. A. Fernandes, "Polymerization kinetics of fischer-tropsch reaction on iron based catalysts and product grade optimization," *Chemical Engineering & Technology: Industrial Chemistry-Plant Equipment-Process Engineering-Biotechnology*, vol. 28, no. 8, pp. 930–938, 2005.

[117] H.-J. Lee *et al.*, "Conceptual design of a fischer–tropsch reactor in a gas-to-liquid process," *Industrial & Engineering Chemistry Research*, vol. 54, no. 26, pp. 6749–6760, 2015.

[118] B. Todic *et al.*, "Co-insertion mechanism based kinetic model of the fischer–tropsch synthesis reaction over re-promoted co catalyst," *Catalysis Today*, vol. 228, pp. 32–39, 2014.

[119] B. Todic *et al.*, "Kinetic model of fischer–tropsch synthesis in a slurry reactor on co–re/al2o3 catalyst," *Industrial & Engineering Chemistry Research*, vol. 52, no. 2, pp. 669–679, 2013.

[120] F. G. Botes, "Proposal of a new product characterization model for the iron-based low-temperature fischer- tropsch synthesis," *Energy & fuels*, vol. 21, no. 3, pp. 1379–1389, 2007.

[121] A. Haghtalab, J. Shariati, and A. Mosayebi, "Experimental and kinetic modeling of fischer–tropsch synthesis over nano structure catalyst of co–ru/carbon nanotube," *Reaction Kinetics, Mechanisms and Catalysis*, vol. 126, pp. 1003–1026, 2019.

[122] F. Bertoncini *et al.*, "Unravelling molecular composition of products from cobalt catalysed fischer-tropsch reaction by comprehensive gas chromatography: methodology and application," *Oil & Gas Science and Technology-Revue de l'IFP*, vol. 64, no. 1, pp. 79–90, 2009.

APPENDIX A CALIBRATION OF THE ULTRASOUND PROBE

The ultrasound probe emits vibrational energy in the form of ultrasound. When an ultrasound probe is immersed in a liquid, its temperature increases because the vibrational energy is transformed into thermal energy. When calibrating the probe, it is assumed that all of the vibrational energy emitted is converted into thermal energy. By measuring the change in temperature of the liquid, we can calculate the thermal energy transmitted to the liquid and thus deduce the power of the probe. During calibration, the amplitude remains constant. Based on this principle, the power of the probe is determined by the following equation:

$$P_{sonde} = m \times c_p \times \frac{\Delta T}{\Delta t} \tag{A.1}$$

where m is the mass of the liquid, c_p is the mass heat capacity of the liquid, $\Delta T/\Delta t$ is the temperature variation over a time interval Δt.

APPENDIX B SEPARATION AND PURIFICATION OF THE LIQUID

The liquid is transferred to a closed glass container and placed in a refrigerator at a temperature of 4°C. When the sample is cooled, the upper phase containing the C_{5+} hydrocarbon gels, allowing the separation of the two phases. By means of a 1000 μL micropipette, the lower phase containing water and alcohol is collected and transferred into a container. The upper phase is then weighed. The C_{5+} hydrocarbons are diluted in toluene until their wt % represents 20 to 25% of the total weight. The C_{5+} hydrocarbon/toluene mixture is filtered through a 0.45 μm nylon membrane filter of 25 mm diameter connected to a 25 mL syringe. The filter ensures that there are no contaminants in the sample that could block the GC column.

APPENDIX C CALIBRATION OF THE GAS CHROMATOGRAPH

The calibration performed on the compounds CO and CH_4 is analyzed by GC-TCD and GC-FID respectively (Bruker Scion Instruments 456 GC-FID gas).

For the CO calibration, a cylinder with a known molar concentration containing H_2/CO in a 2:1 ratio was available. The flow rate feeding the GC-TCD during the calibration corresponds to the same flow rate used during the FTS, which allows the calculation of the surface area when the conversion of CO is 0. It is then possible to identify the surface area given by the GC-TCD for a given molar concentration.

For the calibration of CH_4, a cylinder with a defined molar concentration was used to establish a calibration curve. For a given molar concentration injected into the GC-FID, it was possible to identify the corresponding surface area. The CH_4 was then diluted to different concentrations in order to be able to make a calibration curve from a single cylinder.

APPENDIX D CALIBRATION OF THE LIQUID CHROMATOGRAPH

The calibration performed on the hydrocarbons is analyzed by GC-FID (Agilent 7890B).

Two calibration mixtures containing hydrocarbons at a known molar concentration were used for the calibration of hydrocarbons present in the liquid phase. The first calibration mixture contains C7, C8, C9, C10 hydrocarbons (47101 n-Paraffin Mix C7, C8, C9, C10 Sigma Aldrich) and the second sample contains C10, C12, C14, C16 hydrocarbons (47102 n-Paraffin Mix C10, C12, C14, C16 Sigma Aldrich). Each calibration mixture was diluted with toluene to obtain calibration samples at different weight fractions (mg mg^{-1}). For a given weight fraction injected into the GC, it was possible to identify the retention time of each hydrocarbon species and the corresponding surface area, in order to plot the calibration curves.

For the hydrocarbons not present in the calibration mixtures (such as C5, C6, C11, C13, etc.), iterations, based on the results of the calibration, were performed on these hydrocarbons to identify their approximate weight fraction based on the area under the curve and their retention time given by the GC.

APPENDIX E CHAUVENET'S CRITERION

Chauvenet's criterion allows for determining if data coming from a measurement is aberrant compared to the other measured data. Using this criterion, the deviation is calculated as follows:

$$Deviation = \left| \frac{x_i - \bar{x}}{s} \right| \tag{E.1}$$

where x_i is one of the values subject to Chauvenet's criterion, $\bar{x}$ is the mean of the measured data, and s is the standard deviation of the measured data. The calculated deviation for the tested data is compared to the critical value of Chauvenet's criterion. The critical values are listed in Table E.1.

The choice of the critical value to which the deviation is compared depends on the number of total measured data that are subject to the criterion. For example, if the number of tested data is 50 (n=50), the critical value used for the comparison is 2.576. If the calculated deviation exceeds the critical value, the data is considered an outlier and should be eliminated. When data is eliminated, the mean ($\bar{x}$) and standard deviation (s) must be recalculated. Select the new critical value and compare the deviations for each measured data again to the critical value until all the deviations are less than the critical value of Chauvenet's criterion.

n	critical value
2	1.150
3	1.383
4	1.534
5	1.645
6	1.732
7	1.803
8	1.863
9	1.915
10	1.960
11	2.000
12	2.037
13	2.070
14	2.100
15	2.128
16	2.154
17	2.178
18	2.200
19	2.222
20	2.241
21	2.260
22	2.278
23	2.295
24	2.311
25	2.326
26	2.341
27	2.355
28	2.369
29	2.382
30	2.394
31	2.406
32	2.418
33	2.429
34	2.440
35	2.450
36	2.460
37	2.470
38	2.479
39	2.489
40	2.498
50	2.576
100	2.807
500	3.291
1000	3.481

Table E.1 Critical values of Chauvenet's criterion

APPENDIX F SUPPLEMENTARY IMAGES

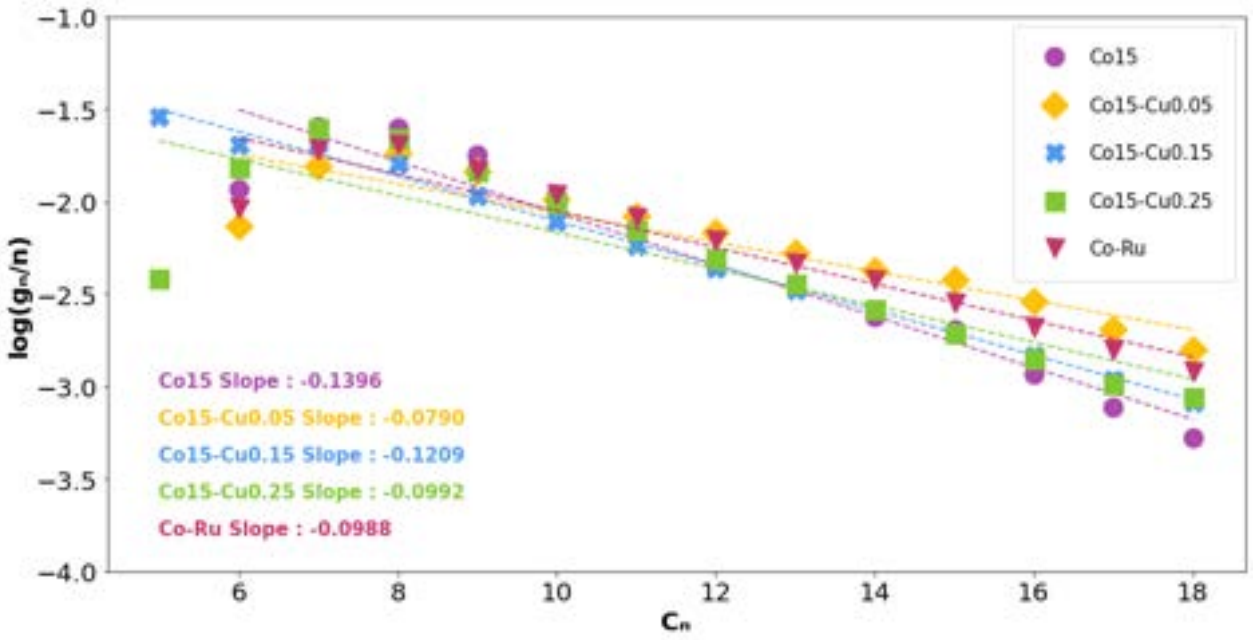

Figure F.1 ASF diagram obtained after ∼5 to 6 days for each of the tested catalysts

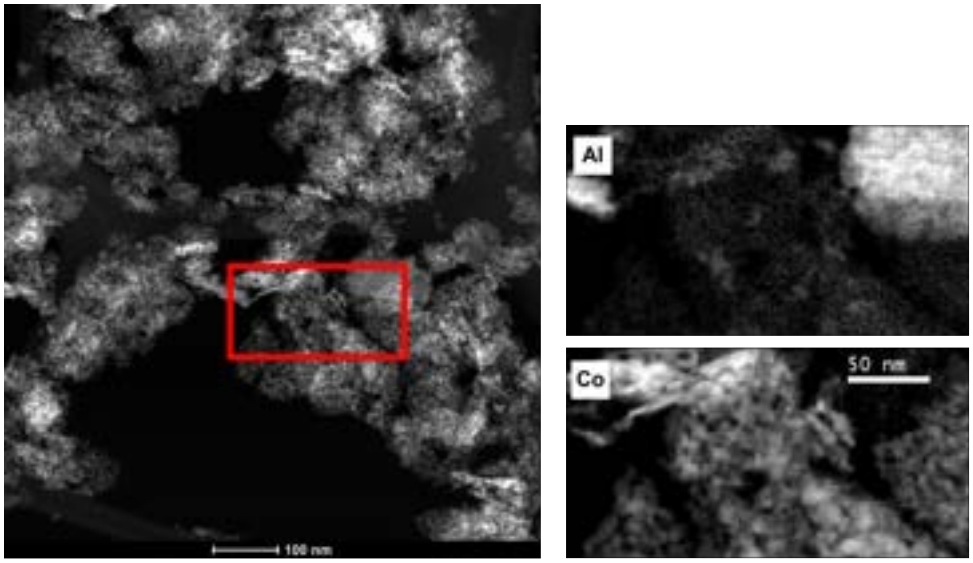

Figure F.2 EELS map of Co15 fresh where Co NPs are distinguished as 6.0 nm in diameter. The red square represents Co and Cu dispersed on Al_2O_3

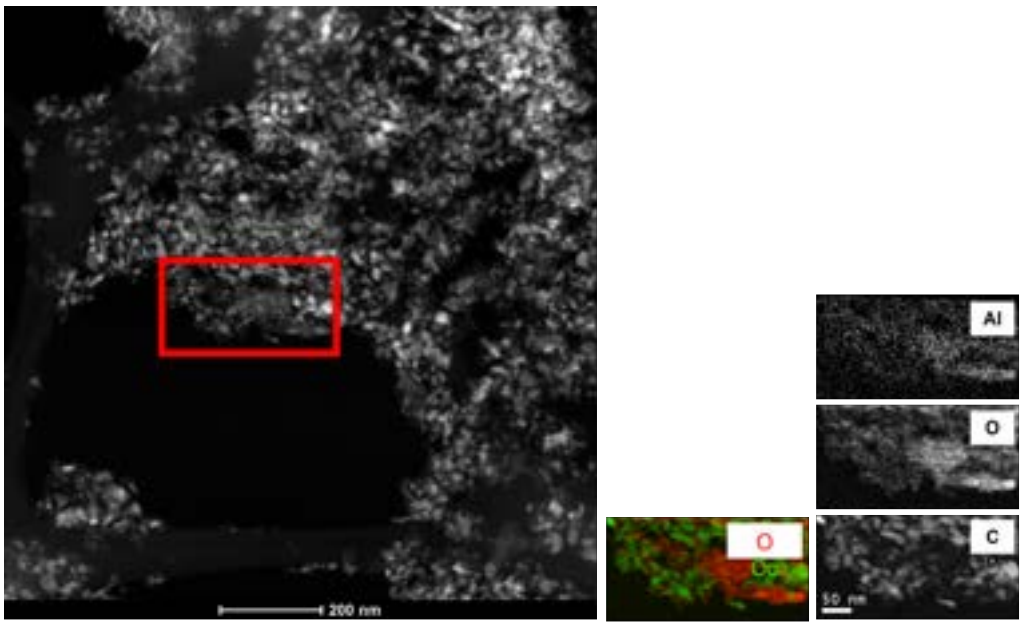

Figure F.3 EELS map of Co15 used where Co NPs are distinguished as 11.4 nm in diameter. The red square represents Co and Cu dispersed on Al_2O_3

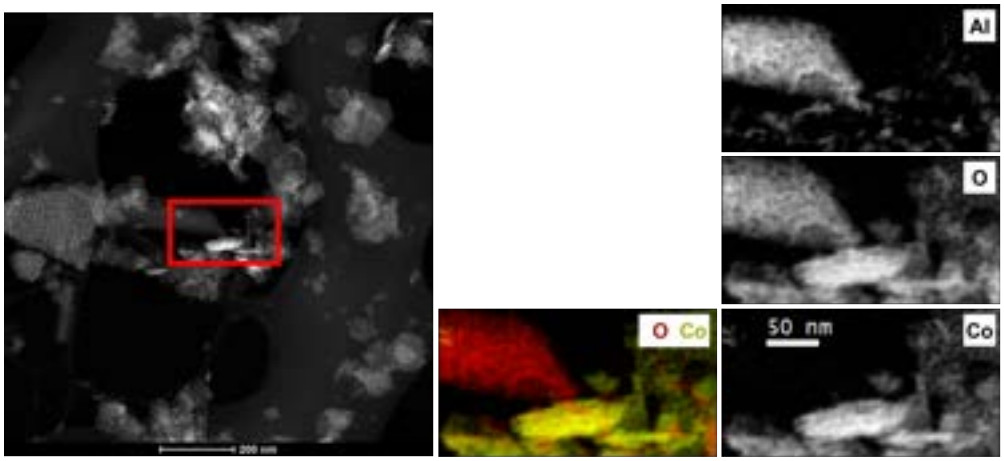

Figure F.4 EELS map of Co15-Cu0.25 fresh where Co NPs are distinguished as 6.0 nm in diameter. The red square represents Co and Cu dispersed on Al_2O_3

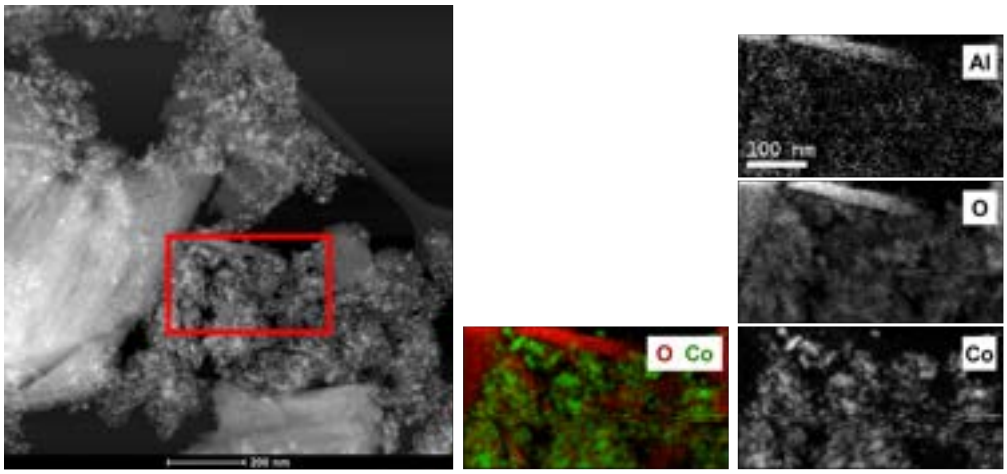

Figure F.5 EELS map of Co15-Cu0.25 used where Co NPs are distinguished as 9.2 nm in diameter. The red square represents Co and Cu dispersed on Al_2O_3

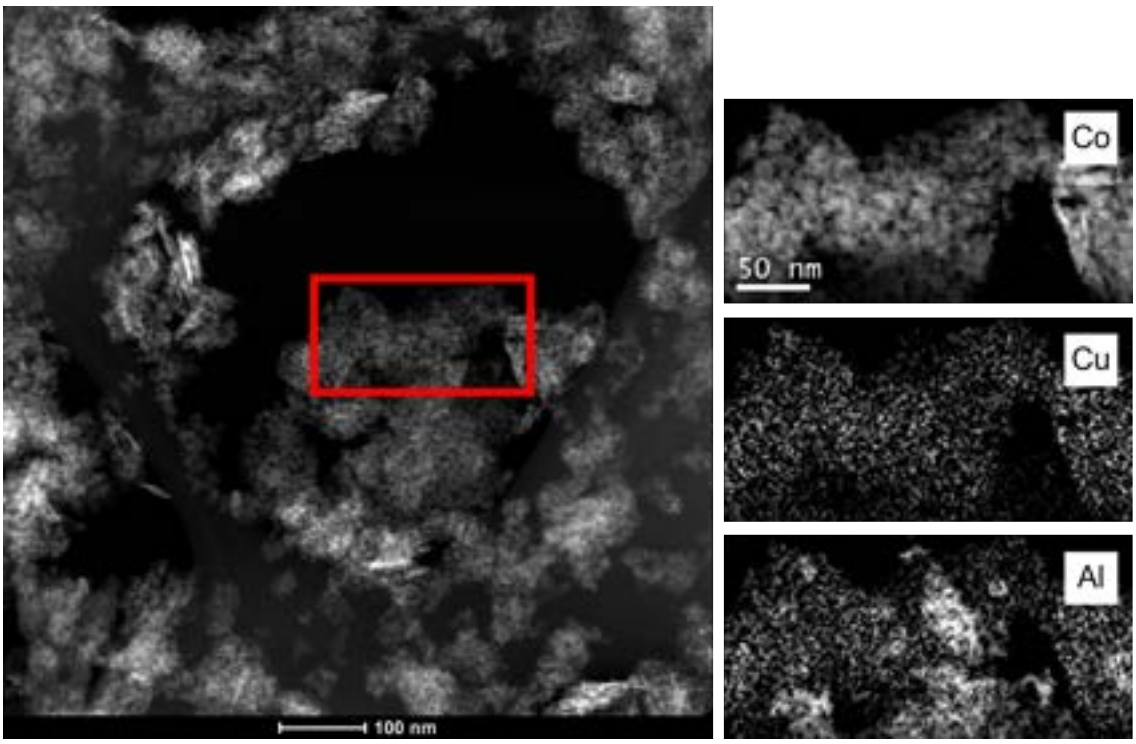

Figure F.6 EELS map of Co15-Cu0.50 fresh where Co NPs are distinguished as 6.0 nm in diameter. The red square represents Co and Cu dispersed on Al_2O_3

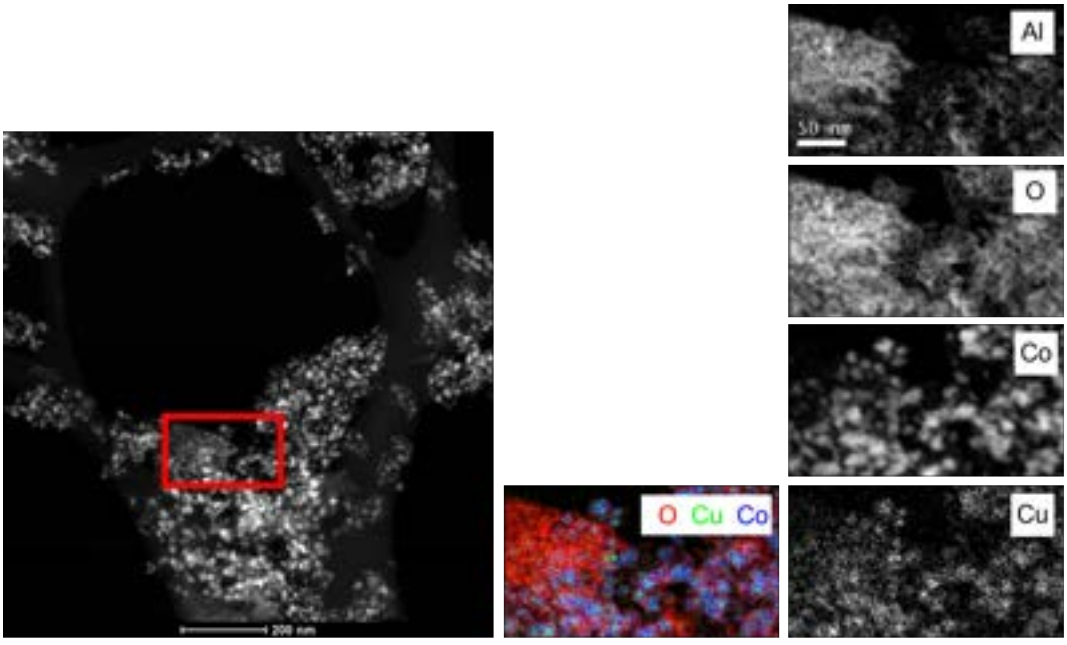

Figure F.7 EELS map of Co15-Cu0.50 used where Co NPs are distinguished as 10.0 nm in diameter. The red square represents Co and Cu dispersed on Al_2O_3

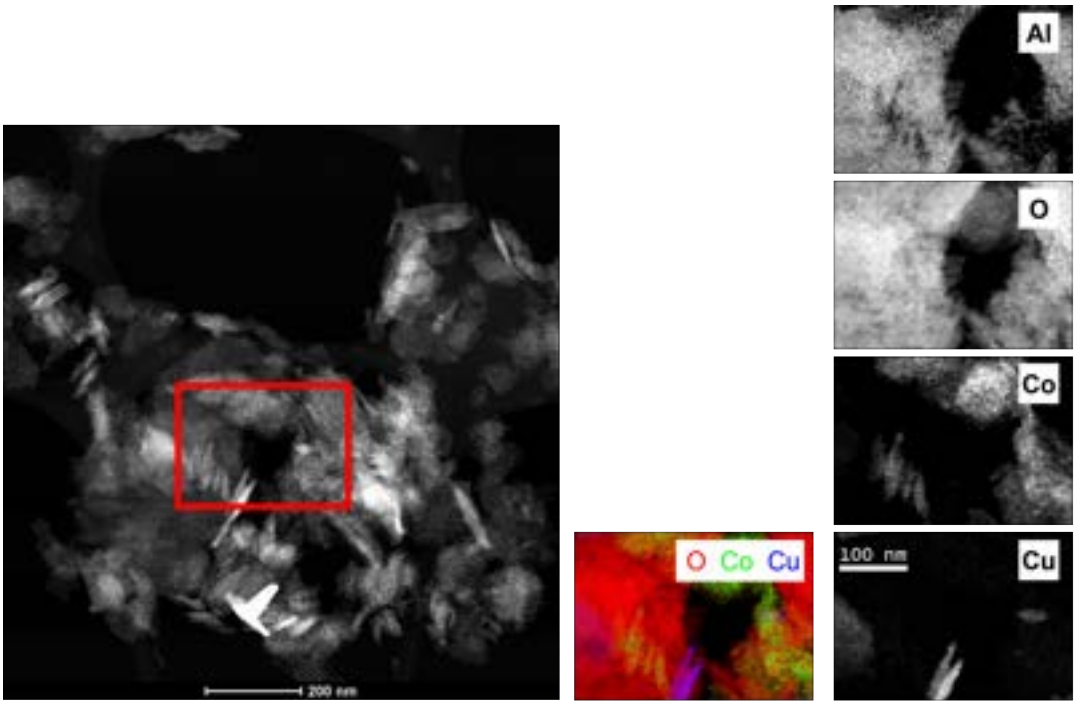

Figure F.8 EELS map of Co15-Cu7.50 fresh where Co NPs are distinguished as 2.9 nm in diameter. The red square represents Co and Cu dispersed on Al_2O_3

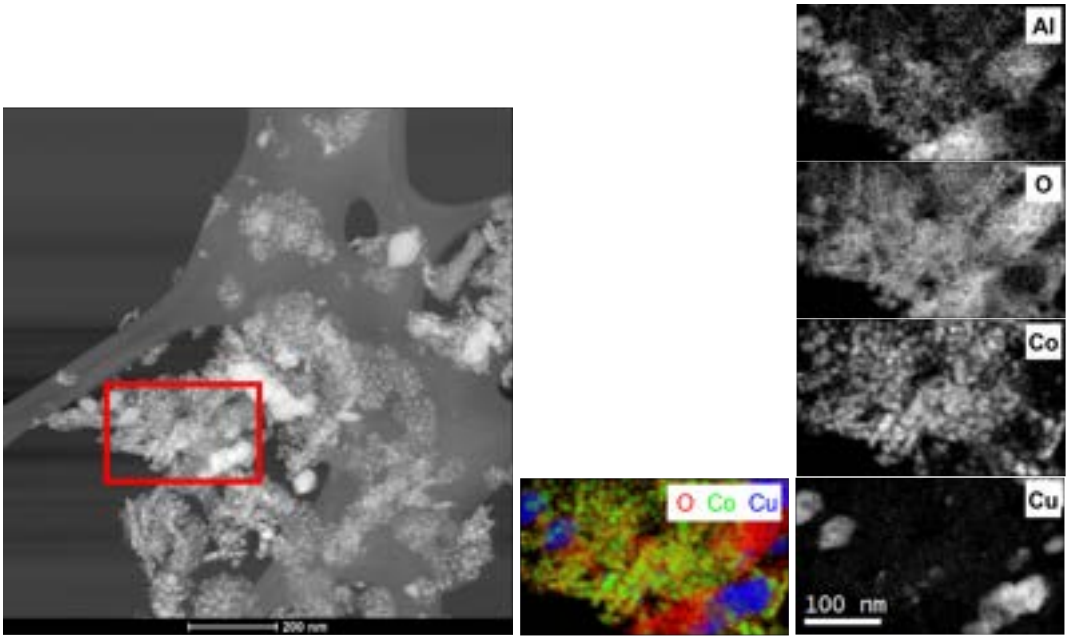

Figure F.9 EELS map of Co15-Cu7.50 used where Co NPs are distinguished as 10.5 nm in diameter. The red square represents Co and Cu dispersed on Al_2O_3

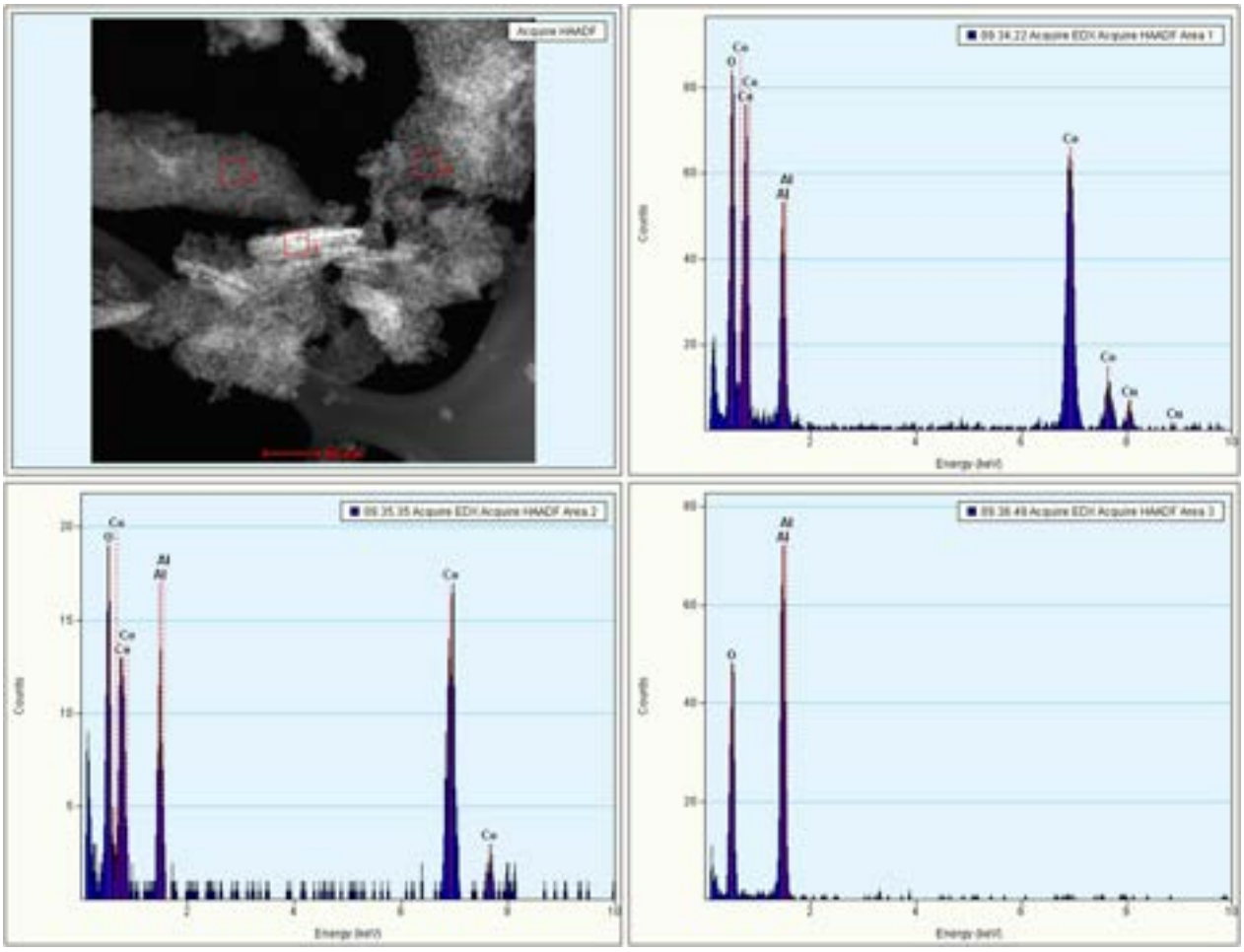

Figure F.10 EDX mapping of fresh Co15-Cu0.25 where Co and Cu are detected and labelled by the red squares 2 at the center of the Al_2O_3 surface

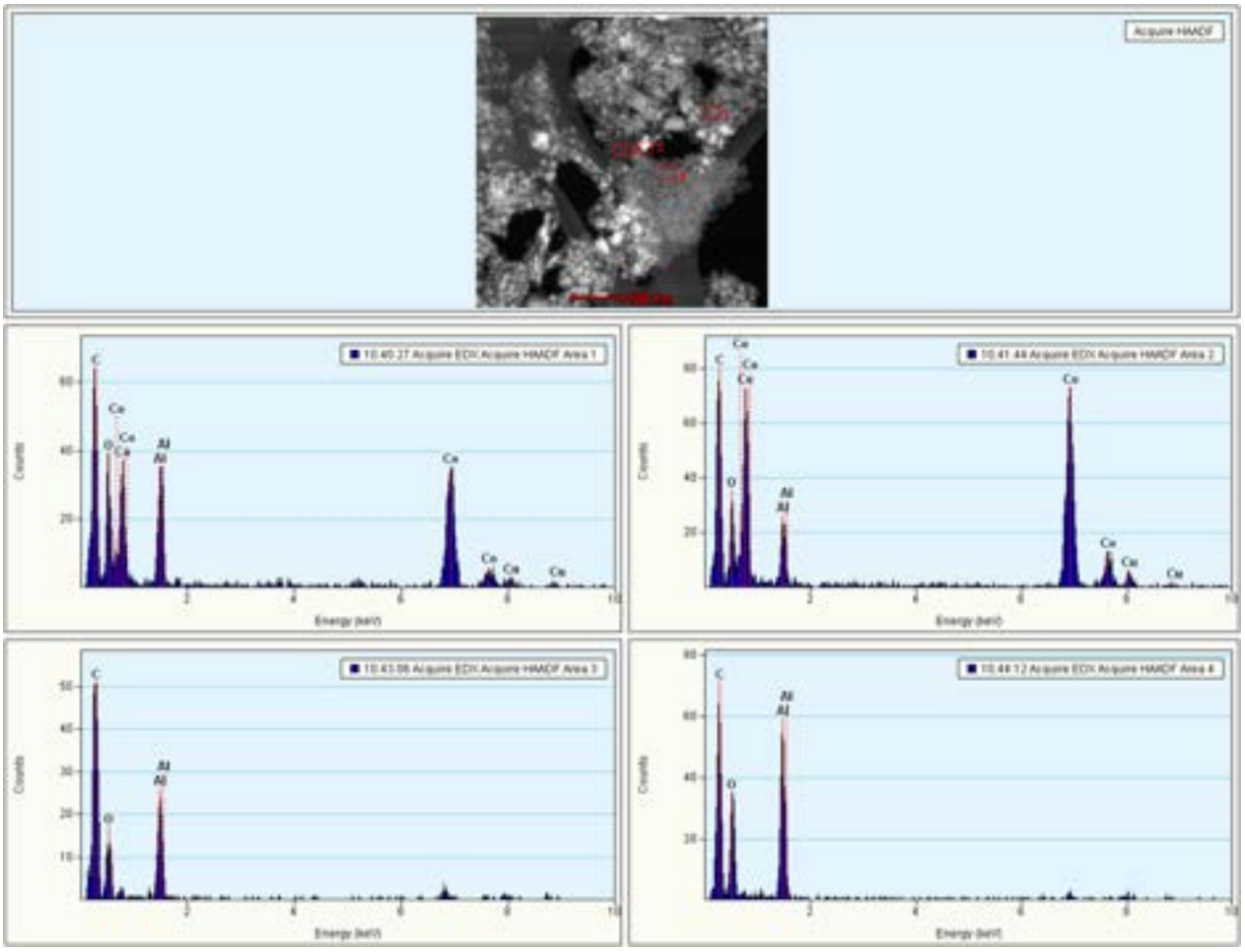

Figure F.11 EDX mapping of used Co15-Cu0.25 where Co and Cu are detected and labelled by the red squares 1 and 2 at the center of the Al_2O_3 surface

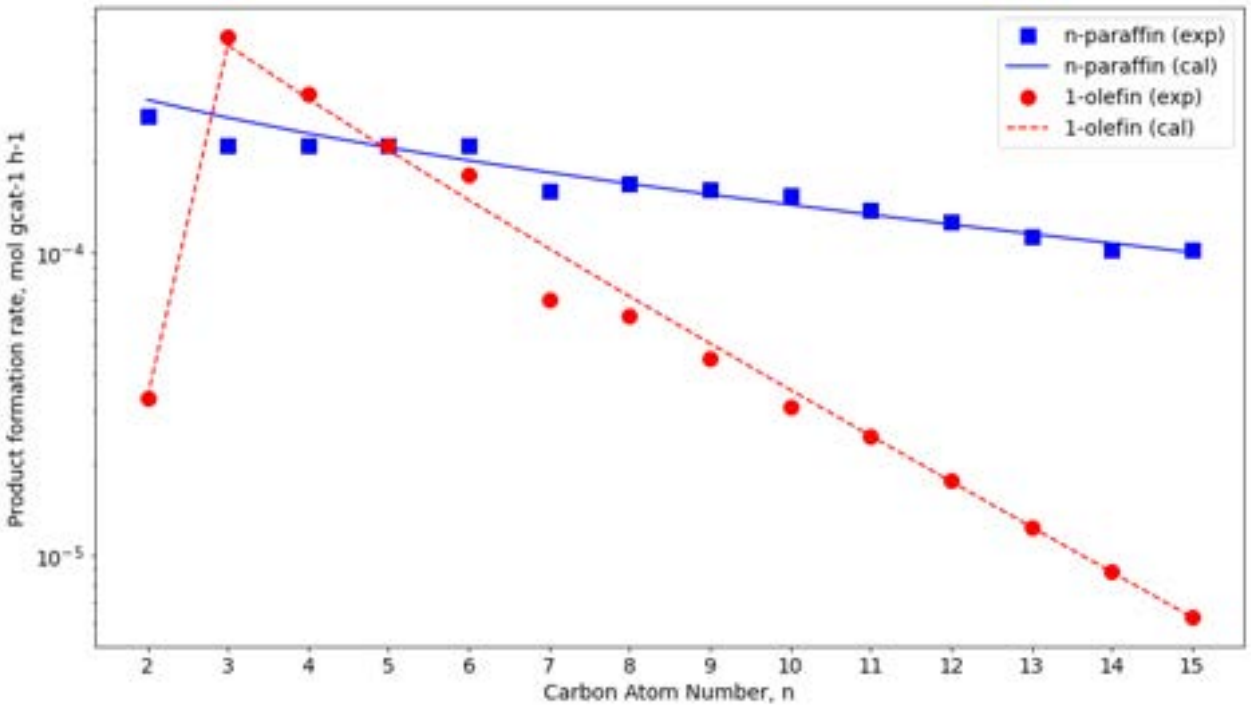

Figure F.12 Experimental and optimized calculated product distribution from experimental and model parameter values of Todic et al. for n-paraffin and 1-olefin formation rates

Table F.1 Values of Todic et al. model parameters

Parameter	Value	Unit	Parameter	Value	Unit
A_1	6.59×10^{-5}	MPa^{-1}	ΔH_1	-48.9	kJ/mol
A_2	1.64×10^{-4}	MPa^{-1}	ΔH_2	-9.4	kJ/mol
A_3	4.14×10^{8}	$mol/(g_{cat} \times h)$	E_3	92.8	kJ/mol
A_4	3.59×10^{5}	-	ΔH_4	16.2	kJ/mol
A_5	9.81×10^{-2}	-	ΔH_5	11.9	kJ/mol
A_6	1.59×10^{6}	MPa	ΔH_6	14.5	kJ/mol
A_7	4.53×10^{7}	$mol/(g_{cat} \times h)$	E_7	75.5	kJ/mol
A_8	4.11×10^{8}	$mol/(g_{cat} \times h)$	E_8	100.4	kJ/mol
A_{7M}	7.35×10^{7}	$mol/(g_{cat} \times h)$	E_{7M}	65.4	kJ/mol
A_{8E}	4.60×10^{7}	$mol/(g_{cat} \times h)$	E_{8E}	103.2	kJ/mol
ΔE	1.1	$kJ/mol/CH_2$			

Table F.2 Values of Co15 model parameters

Parameter	Value	Unit	Parameter	Value	Unit
A_1	6.59×10^{-5}	MPa^{-1}	ΔH_1	-48.9	kJ/mol
A_2	1.64×10^{-4}	MPa^{-1}	ΔH_2	-9.4	kJ/mol
A_3	4.17×10^{8}	$mol/(g_{cat} \times h)$	E_3	99.8	kJ/mol
A_4	3.59×10^{5}	-	ΔH_4	16.2	kJ/mol
A_5	9.81×10^{-2}	-	ΔH_5	11.9	kJ/mol
A_6	1.59×10^{6}	MPa	ΔH_6	14.5	kJ/mol
A_7	4.53×10^{7}	$mol/(g_{cat} \times h)$	E_7	75.5	kJ/mol
A_8	4.11×10^{8}	$mol/(g_{cat} \times h)$	E_8	100.4	kJ/mol
A_{7M}	7.35×10^{7}	$mol/(g_{cat} \times h)$	E_{7M}	65.4	kJ/mol
A_{8E}	4.60×10^{7}	$mol/(g_{cat} \times h)$	E_{8E}	103.2	kJ/mol
ΔE	1.1	$kJ/mol/CH_2$			

Table F.3 Values of Co15-Cu0.05 model parameters

Parameter	Value	Unit	Parameter	Value	Unit
A_1	6.38×10^{-5}	MPa^{-1}	ΔH_1	-49.0	kJ/mol
A_2	1.71×10^{-4}	MPa^{-1}	ΔH_2	-9.2	kJ/mol
A_3	4.13×10^{8}	$mol/(g_{cat} \times h)$	E_3	97.8	kJ/mol
A_4	3.59×10^{5}	-	ΔH_4	16.2	kJ/mol
A_5	9.44×10^{-2}	-	ΔH_5	13.5	kJ/mol
A_6	1.59×10^{6}	MPa	ΔH_6	14.5	kJ/mol
A_7	4.71×10^{7}	$mol/(g_{cat} \times h)$	E_7	74.9	kJ/mol
A_8	4.13×10^{8}	$mol/(g_{cat} \times h)$	E_8	100.5	kJ/mol
A_{7M}	7.01×10^{7}	$mol/(g_{cat} \times h)$	E_{7M}	68.5	kJ/mol
A_{8E}	5.02×10^{7}	$mol/(g_{cat} \times h)$	E_{8E}	101.6	kJ/mol
ΔE	1.12	$kJ/mol/CH_2$			

Table F.4 Values of Co15-Cu0.15 model parameters

Parameter	Value	Unit	Parameter	Value	Unit
A_1	6.62×10^{-5}	MPa^{-1}	ΔH_1	-48.4	kJ/mol
A_2	1.74×10^{-4}	MPa^{-1}	ΔH_2	-10.5	kJ/mol
A_3	4.11×10^{8}	$mol/(g_{cat} \times h)$	E_3	97.4	kJ/mol
A_4	3.59×10^{5}	-	ΔH_4	16.2	kJ/mol
A_5	9.81×10^{-2}	-	ΔH_5	11.9	kJ/mol
A_6	1.59×10^{6}	MPa	ΔH_6	14.5	kJ/mol
A_7	4.76×10^{7}	$mol/(g_{cat} \times h)$	E_7	74.8	kJ/mol
A_8	4.07×10^{8}	$mol/(g_{cat} \times h)$	E_8	101.9	kJ/mol
A_{7M}	7.02×10^{7}	$mol/(g_{cat} \times h)$	E_{7M}	67.8	kJ/mol
A_{8E}	4.60×10^{7}	$mol/(g_{cat} \times h)$	E_{8E}	103.2	kJ/mol
ΔE	1.1	$kJ/mol/CH_2$			

Table F.5 Values of Co15-Cu0.25 model parameters

Parameter	Value	Unit	Parameter	Value	Unit
A_1	6.76×10^{-5}	MPa^{-1}	ΔH_1	-48.2	kJ/mol
A_2	1.45×10^{-4}	MPa^{-1}	ΔH_2	-11.6	kJ/mol
A_3	4.15×10^{8}	$mol/(g_{cat} \times h)$	E_3	97.8	kJ/mol
A_4	3.59×10^{5}	-	ΔH_4	16.2	kJ/mol
A_5	9.81×10^{-2}	-	ΔH_5	11.9	kJ/mol
A_6	1.59×10^{6}	MPa	ΔH_6	14.5	kJ/mol
A_7	5.01×10^{7}	$mol/(g_{cat} \times h)$	E_7	75.5	kJ/mol
A_8	4.05×10^{8}	$mol/(g_{cat} \times h)$	E_8	101.9	kJ/mol
A_{7M}	7.30×10^{7}	$mol/(g_{cat} \times h)$	E_{7M}	67.1	kJ/mol
A_{8E}	4.60×10^{7}	$mol/(g_{cat} \times h)$	E_{8E}	103.2	kJ/mol
ΔE	1.1	$kJ/mol/CH_2$			